

# UNIVERSITÀ DI PISA

DIPARTIMENTO DI FISICA "ENRICO FERMI"

Corso di Laurea Magistrale in Fisica


TESI DI LAUREA

# Performance Improvement of the Inertial Sensors of Advanced Virgo Seismic Isolators with Digital Techniques


Candidato:
**Giovanni Cerretani**

Relatori:
**Dott. Diego Passuello**
**Ing. Alberto Gennai**



**Anno Accademico 2012/2013**

# Contents

# Abstract

Gravitational waves, predicted on the basis of the General Relativity, are ripples in the curvature of space-time that propagate as a wave. The passage of a gravitational wave induces tiny oscillations in the relative separation between two test masses, that can be measured. Nevertheless these oscillations are extremely small, so that only a very sensitive detector is able to measure them. The Advanced Virgo project is a major upgrade of the 3 km-long interferometric gravitational wave detector Virgo, with the goal of increasing its sensitivity by about one order of magnitude in the whole detection band. We expect to have a maximum strain amplitude sensitivity of $4 \times 10^{-24} \frac{1}{\sqrt{\text{Hz}}}$ at $\sim 300$ Hz. In other words this means that it will be able to detect a relative displacement between mirrors of about $10^{-20}$ m, by averaging for one second. This sensitivity should allow to detect several tens of events per year.

Among the various ongoing updates, an important improvement is represented by the new electronics used to control the Superattenuators, complex mechanical structures that isolate optical elements from seismic noise by a factor $10^{15}$ at 1 Hz. Using the information of several inertial sensors, a digital control system keeps the structures as stable as possible. A new board for the Superattenuator control has been designed, that incorporates analog-to-digital and digital-to-analog converters, a Field Programmable Gate Array (FPGA) and a Digital Signal Processor (DSP) into a single unit. This board is enough to handle every single part of the Superattenuator inertial control. It performs the computation of feedback forces, and is used to synthesize sine wave to drive the coils of the inertial sensors, as well as to read their output. Furthermore it interfaces with all the other structures of Virgo.

In this thesis I have studied the horizontal accelerometers, feedback-controlled sensors used in the Superattenuator inertial control to measure the seismic noise in the frequency band from DC to 100 Hz. Using the computing power of the new electronics (the new DSP has 8 cores and can compute 8.4 GFLOPS per core for double precision floating point indeed), I have designed a new control system for the accelerometers, exploiting the properties of a critically damped harmonic oscillator. This system

allows to improve by about one order of magnitude the sensitivity of these sensors, with respect to the system used in Virgo, by reducing the root mean square of the force needed for the control by a factor 2. In this way, the accelerometer sensitivity can reach about $10^{-9}\,\frac{\mathrm{m/s^2}}{\sqrt{\mathrm{Hz}}}$ at 1 Hz.

In the last part of the thesis I have studied the Linear Variable Differential Transformer (LVDT), a kind of displacement sensor widely used in Superattenuator control. I have designed a system to read the output of LVDT using a FPGA. It consists of a Direct Digital Synthesizer (DDS) that is used both to drive the primary coil of the LVDT with a sine wave at 50 kHz, and then to demodulate the signal induced on the secondary coils, whose amplitude is modulated by a signal proportional to displacement. An algorithm, based on a Phase-Locked Loop (PLL), allows the detection of the phase shift of the signal induced on the secondary coils, and tunes the system in order to maximize the signal-to-noise ratio of the measurement of displacement.

# Introduction

*Virgo* is a 3 km-long laser Michelson interferometer located in Italy, whose aim is the direct observation of gravitational wave, in frequency range extended from 10 Hz to 10 kHz. It acquired data from 2007 up to 2011. As shown in Fig. 0.1, the sensitivity of the experiment has changed during the years, up to reach in 2011 the design specs with the update named Virgo+: the maximum strain amplitude sensitivity was $h = 4 \times 10^{-23} \frac{1}{\sqrt{\text{Hz}}}$ at 300 Hz. According to the project, in this final configuration it was supposed to detect a few events per year, but no evidence of gravitational wave has been found in data analyses so far.

The absence of events is likely due to an overestimation of rates in the initial design, primarily because of a bad knowledge of some stellar parameters. The realistic rate of events detectable by Virgo in its initial design, updated to the most recent hypothesis in stellar field, is

$$R_{re} \sim 0.03\,\text{yr}^{-1} \tag{0.1}$$

mostly due to neutron stars coalescence. [1]

It is clear that in these conditions is very difficult to detect something. Because of it, a significant upgrade is in progress at Virgo; this will lead to a new generation of gravitational wave antennas: Advanced Virgo (AdV). Also LIGO, the other main experiment in the gravitational wave field, is undergoing a similar upgrade.

The aim of Advanced Virgo is to achieve a sensitivity that is an improvement on the original Virgo by one order of magnitude in sensitivity, which corresponds to an increase of the detection rate by three orders of magnitude. According to a realistic estimation of the binary system coalescence rates in the universe (the same used in equation 0.1), this upgrade would allow to see [1]

$$R_{re} \sim 70\,\text{yr}^{-1} \tag{0.2}$$

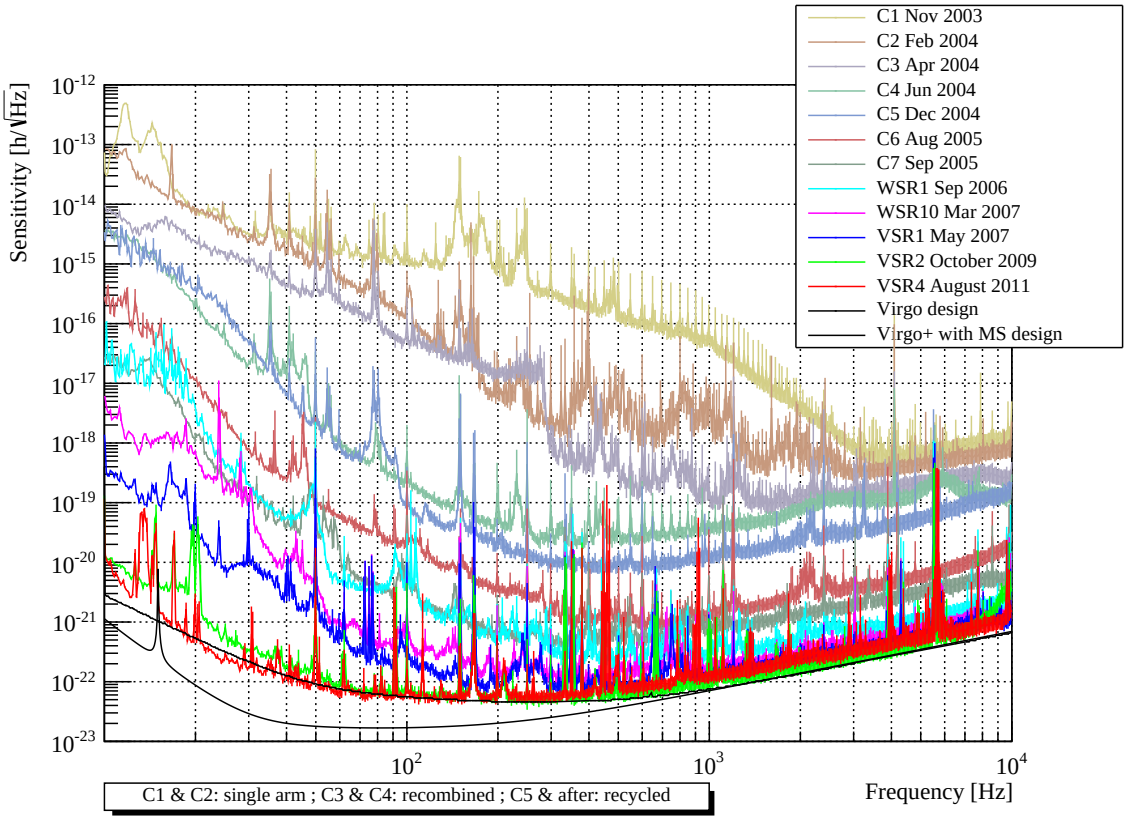


**Figure 0.1.:** Strain amplitude spectral densities of Virgo during time, compared with the design sensitivity. Virgo+ represents the last update to the interferometer, performed in 2010.

The design sensitivity curve of Advanced Virgo is shown in figure Fig. 0.2: the maximum strain amplitude sensitivity of $h = 3.5 \times 10^{-24} \frac{1}{\sqrt{\text{Hz}}}$ is expected at $\sim 300\,\text{Hz}$. In other words this means that it will be able to detect a relative displacement between mirrors of about $10^{-20}\,\text{m}$, by averaging for one second.

Therefore, most of the detector subsystems have to deliver a largely improved performance to be compatible with the design sensitivity. Of course, the achievement of this goal requires to take to the limit of perfection every single component of the interferometer. The power of new laser will be increased by one order of magnitude, the interferometer optical configuration will undergo the installation of new components, mirrors will be replaced with new ones twice as heavy as before to limit the effect of radiation pressure, the vacuum level will be improved by a factor of about 100, just to name a few.

For this thesis I joined the group responsible of the Superattenuator inertial control, a complex feedback system conceived to extraordinarily reduce effects of the seismic noise at the level of the mirrors, by a factor $10^{15}$ at 1 Hz. Indeed, the vibrations of the ground limit the sensitivity of an Earth-based gravitational wave detector at

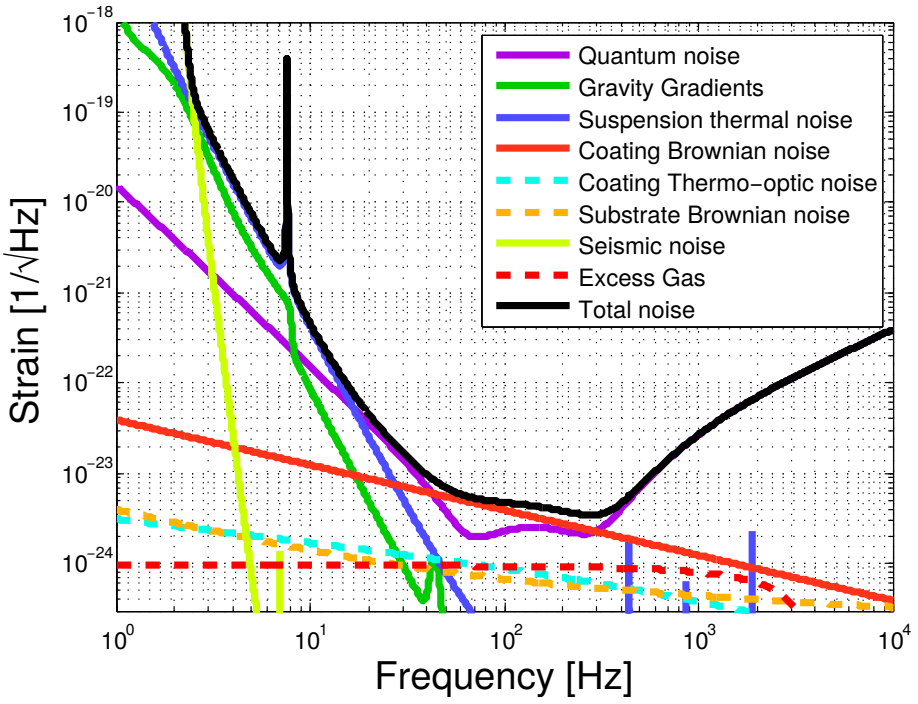


**Figure 0.2.:** Advanced Virgo design sensitivity with noise budget [2]

low frequencies, as it's shown in Fig. 0.2, and must be properly treated. The main effort of the group for Advanced Virgo is to design a new electronic system, that incorporates analog-to-digital and digital-to-analog converters and a Digital Signal Processor (DSP) into a single unit. This board is enough to handle every single part of the Superattenuator inertial control. It performs the computation of feedback forces to keep the whole system as stable as possible, and is used to synthesize sine wave to drive the coils of the inertial sensors, as well as to read their output. Furthermore it interfaces with all the other structures of Virgo. This is possible due to the huge computing power of modern DSPs, that can natively handle double precision floating point, performing sums and multiplications very fast. They run a software called Inertial Damping, almost entirely written in assembly language to optimize as much as possible the application of digital filters and to make the duration of calculations predictable. This is mandatory, because unpredictable delays are not tolerated in such a delicate real time application. A first prototype of the new board arrived in Virgo site at the end of 2013 and, of course, a lot of work has to be done, both in hardware and software, to be ready for the beginning of Advanced Virgo operations expected by the end of 2015.

The production of the new board also entails the reduction of the number of boards used up to now. In addition to those that will be merged together, in each crate we will remove a commercial waveform generator, a board used to read displacement sensors and another one used for the analog control of the accelerometer: the new DSP is fast enough to take over also the management of these operations.

The Part I of this thesis contains an introduction on the search for gravitational waves, from the theoretical background to the possible sources.

In the Part II, I study the horizontal accelerometers, feedback-controlled sensors used in the Superattenuator inertial control to measure the seismic noise in the frequency band from DC to 100 Hz. I analyze their operating principles and the typical signal that they might measure. Then, exploiting the performances of the new board, I design a new control system for the accelerometers, exploiting the properties of a critically damped harmonic oscillator

The implementation of this system is presented in the Part III of the thesis, together with its noise budget: we see how this new control system increase the sensitivity of the experiment of almost one order of magnitude. It contains also the description of an algorithm, implemented in the new electronics, that allows to maximize the signal-to-noise ratio of the measurement of displacement using a Linear Variable Differential Transformer (LVDT), a displacement sensor widely used in Virgo.

# Part I.

# Gravitational Waves

# 1 A Little of Theory

## 1.1. An Introduction to General Relativity

The gravitational force dominates the universe on the large scale, binding matter into stars, stars into galaxies, and galaxies into cluster of galaxies. The classic theory of gravitation is based on Newton's law of gravity which states that who masses $m_1$ and $m_2$ separated by a distance $r$ feel a mutual gravitational attraction

$$F = -G\frac{m_1 m_2}{r^2} \tag{1.1}$$

where $G$ is a constant of proportionality called "universal gravitational constant"; its value is $G = 6.67384(80) \times 10^{-11}\,\mathrm{m^3\,kg^{-1}\,s^{-2}}$. [3] This equation describes the motion of the planets around the Sun with great accuracy. However, there are several features that cannot be explained by the Newton's law. The most significant one is a tiny component in the precession of the perihelion of the orbit of Mercury. The main problem is that equation 1.1 is time independent, which would mean that the gravitational force could act instantaneously at all distances. Such behavior is in flat contradiction to the "Special Theory of Relativity" (SR), which requires that no signal should travel faster than the speed of light $c$. [4]

The problem is shared with electromagnetism and Coulomb's law: in this case it was solved with Maxwell's equations, witch are consistent with SR.

In 1916 Albert Einstein published his geometric theory of gravitation, called "General Theory of Relativity" or "General Relativity" (GR), that is a description of gravitation consistent with special relativity.

### 1.1.1. The Principle of Equivalence

General relativity is based on the Principle of Equivalence. This establishes the equality of gravitational and inertial mass, demonstrated at first by Galileo and

Newton. Einstein interpreted this result to postulate the "weak equivalence principle": *the motion of a neutral test body released at a given point in space-time is independent of its composition.* [4]

Furthermore, Einstein reflected that, as a consequence, no external static homogeneous gravitational field could be detected in a freely falling elevator, because the observers, their test bodies, and the elevator itself would respond to the field with the same acceleration. Although inertial forces do not exactly cancel gravitational forces for freely falling systems in an inhomogeneous or time-dependent gravitational field, we can still expect an approximate cancellation if we restrict our attention to such a small region of space and time that the field changes very little over the region. Therefore, the "strong equivalence principle" was postulated by Einstein and it states that *at every space-time point in an arbitrary gravitational field is possible to choose a "locally inertial coordinate system" such that, within a sufficiently small region of the point in question, the laws of nature take the same form as in unaccelerated Cartesian coordinate systems in the absence of gravitation.* [5]

### 1.1.2. General Relativity and Einstein's Field Equations

According to General relativity, the universe consists of an active space-time continuum that is distorted by matter and energy passing through it.

A first effect predicted by general relativity was detected by Arthur Stanley Eddington in 1919. The theory suggest that starlight which passes the limb of the Sun on its way to the Earth should be deflected by $1.750''$. Eddington organized an expedition to the Island of Príncipe (São Tomé and Príncipe) which photographed the star field around the Sun during a solar eclipse occurred on May 29. When comparison was made with night photographs of the same star field, the predicted general relativistic deflection was confirmed. [4]

Since that day the predictions of general relativity have been confirmed in all observations and experiments up to now. Among the other results, in the limit of low velocities and small gravitational effects, GR reduces to Newton's law with small corrections: in the case of Mercury, these corrections account precisely for the small residual advance of perihelion.

GR allows to describe the curvature of space-time, as directly related to the energy and momentum of whatever matter and radiation are present. The relation is specified by the Einstein field equations, a set of 10 partial differential equations:

$$R_{\mu\nu} - \frac{1}{2} g_{\mu\nu} R - \lambda g_{\mu\nu} = 8\pi G T_{\mu\nu} \tag{1.2}$$

$g_{\mu\nu}$ is the metric tensor, that contains information about the intensity of the gravitational field. $R_{\mu\nu}$ represent the curvature of the space-time and contains second derivatives of $g_{\mu\nu}$, while $R = g^{\mu\nu} R_{\mu\nu}$ is called scalar curvature. $\lambda$ was introduced

by Einstein and is called the *cosmological constant*: for some reasons it has to be very small and, four our purposes, we can assume $\lambda = 0$. Finally, $T_{\mu\nu}$ is the energy–momentum tensor and contains the distribution of energy and momentum in the space-time.

## 1.2. Gravitational radiation

There ares many similarities between gravitation and electromagnetism. It should therefore come as no surprise that Einstein's equations, like Maxwell equations, have radiative solutions.

We know that electromagnetic propagation is described by d'Alembert equations ($c = 1$)

$$\Box A_\mu = J_\mu/\epsilon_0 \tag{1.3}$$

deriving from Maxwell's equation, where $A_\mu = (\phi, \mathbf{A})$ describes the electromagnetic potentials and $J_\mu = (\rho, \mathbf{j})$ describes the source of the field. [6] A particular solution to this equation is represented by the retarded potentials:

$$A_\mu(\mathbf{x}, t) = \frac{1}{4\pi\epsilon_0}\int d^3\mathbf{x}' \frac{J_\mu(\mathbf{x}', t - |\mathbf{x}' - \mathbf{x}|)}{|\mathbf{x}' - \mathbf{x}|} \tag{1.4}$$

They show that the state of the field in a certain point of the space-time depends on that of the source at a previous time $t - |\mathbf{x}' - \mathbf{x}|$: the information propagates at speed $c$ into the electromagnetic waves.

The derivation of gravitational radiation from Einstein's field equations 1.2 is more complicated than that of electromagnetic radiation from Maxwell's equations, due to the nonlinearity of the first. Maxwell's equations are linear because the electromagnetic field does not itself carry charge; on the other hand, we may say that any gravitational wave is itself a distribution of energy and momentum that contributes to the gravitational field of the wave: it is impossible to separate the contributions of gravitational waves to the curvature from the contributions of the Earth, the Sun, the galaxy, or anything else. Thus, there is no way to find general radiative solutions of the exact Einstein's equations.

Here we present only the weak-field radiative solutions, which describe waves carrying not enough energy to affect their own propagation.

If we suppose to be far from the source of the fields, the space-time will be nearly flat and the metric will be close to the Minkowski metric $\eta_{\mu\nu}$:

$$g_{\mu\nu} = \eta_{\mu\nu} + h_{\mu\nu} \tag{1.5}$$

with $|h_{\mu\nu}| \ll 1$. Now Einstein field equations 1.2 can be written to first order in $h$,

$$R^{(1)}_{\mu\nu} = -8\pi G S_{\mu\nu} \tag{1.6}$$

with

$$R_{\mu\nu} \simeq R^{(1)}_{\mu\nu} \equiv \frac{1}{2}\left(\Box h_{\mu\nu} - \frac{\partial^2}{\partial x^\lambda \partial x^\mu} h^\lambda{}_\nu - \frac{\partial^2}{\partial x^\lambda \partial x^\nu} h^\lambda{}_\mu + \frac{\partial^2}{\partial x^\mu \partial x^\nu} h^\lambda{}_\lambda\right)$$

and

$$S_{\mu\nu} \equiv T_{\mu\nu} - \frac{1}{2}\eta_{\mu\nu} T^\lambda_\lambda$$

We can also perform a further simplification to this equations and, in some steps, write equations 1.6 as

$$\Box h_{\mu\nu} = -16\pi G S_{\mu\nu} \tag{1.7}$$

These equations are actually very similar to 1.3 and naturally we can write retarded solutions

$$h_{\mu\nu}(\mathbf{x}, t) = -4G \int d^3\mathbf{x}' \frac{S_{\mu\nu}(\mathbf{x}', t - |\mathbf{x}' - \mathbf{x}|)}{|\mathbf{x}' - \mathbf{x}|} \tag{1.8}$$

These solutions describe the physical phenomenon of the gravitational waves produced by the source $S_{\mu\nu}$. They are transverse waves traveling with the same finite speed of propagation $c$ of the electromagnetic waves and the same intensity decrease as function of distance from the source.

Far from the source, as $|\mathbf{x}' - \mathbf{x}| \to \infty$, the retarded solution approaches a plane wave, and the equations 1.7 are reduced to the homogeneous ones, $\Box h_{\mu\nu} = 0$. Here, a solution is

$$h_{\mu\nu} = e_{\mu\nu} \exp\left(ik_\lambda x^\lambda\right) + e^*_{\mu\nu} \exp\left(-ik_\lambda x^\lambda\right) \tag{1.9}$$

with

$$k_\mu k^\mu = 0 \tag{1.10}$$

and

$$k_\mu e^\mu{}_\nu = \frac{1}{2} k_\nu e^\mu{}_\mu \tag{1.11}$$

$e_{\mu\nu} = e_{\nu\mu}$ is a 4x4 symmetric tensor and is called the *polarization tensor*. In general, a 4x4 matrix have 10 independent components; the gauge invariance 1.11 reduce them to only 6, but it can be shown that of these six there are only two physically significant degrees of freedom, i.e. only two independent physical polarizations. [5] The commonly used couple of independent polarization is

$$e^+_{\mu\nu} = \begin{pmatrix} 0 & 0 & 0 & 0 \\ 0 & 1 & 0 & 0 \\ 0 & 0 & -1 & 0 \\ 0 & 0 & 0 & 0 \end{pmatrix} \quad \text{and} \quad e^\times_{\mu\nu} = \begin{pmatrix} 0 & 0 & 0 & 0 \\ 0 & 0 & 1 & 0 \\ 0 & 1 & 0 & 0 \\ 0 & 0 & 0 & 0 \end{pmatrix} \tag{1.12}$$

and it forms a basis for the polarization space. The two elements are pronounced respectively *plus* and *cross* polarizations. We can obtain any other polarization (for example the circular polarizations) by a suitable linear superposition of these two.

Reducing wave described in equation 1.9 to a wave traveling along the $z$-axis, i.e. $\mathbf{k} = k \cdot \hat{\mathbf{z}}$, we get

$$h_{\mu\nu} = e_{\mu\nu} \cos\left(k_\lambda x^\lambda\right) = e_{\mu\nu} \cos\left(\omega t - kz\right) \tag{1.13}$$

Using the polarization in 1.12, the general form of 1.13 is made up of a linear combination of the two orthogonal states

$$h^+_{\mu\nu} = h^+ e^+_{\mu\nu} \cos\left(\omega t - kz\right) \tag{1.14}$$

and

$$h^\times_{\mu\nu} = h^\times e^\times_{\mu\nu} \cos\left(\omega t - kz + \varphi\right) \tag{1.15}$$

where $\varphi$ is an arbitrary phase angle, and $h^+$ and $h^\times$ are the amplitudes of the components. A graphical explanation of these two polarization is shown in Fig. 1.1.

## 1.3. The Effects of Gravitational Waves

To understand what happens to the space-time when a gravitational waves passes through it, it can be useful to consider tho nearby bodies located in the same $xy$-plane at $A = (\xi, 0)$ and $B = (0, 0)$. If we suppose the weak field condition 1.5 to be true, their proper separation is

$$ds = \xi' \approx \sqrt{|g_{11}(t,0)|}\xi \approx \left[1 + \frac{h_{11}(t,0)}{2}\right] \xi$$

Applying the wave in equation 1.14, the proper space-time interval between $A$ and $B$ undergoes a strain of amplitude

$$\epsilon^+_x = \frac{\xi' - \xi}{\xi} = \frac{h_{11}(0,0)}{2} = \frac{h^+}{2} \tag{1.16}$$

Thus $\frac{h^+}{2}$ is the amplitude of the differential change in lengths between nearby points along the $x$-axis. A similar reasoning suggests that the same wave would produce a tidal effect along $y$-axis of

$$\epsilon^+_y = -\frac{h^+}{2} \tag{1.17}$$

If the distance between two point is small (with respect to the wavelength of the gravitational radiation) the strain amplitude can be obtained as follows. Suppose to have $A = \left(-\frac{l_0}{2}, 0\right)$ and $B = \left(\frac{l_0}{2}, 0\right)$. Then their proper separation is

$$l(t) = \int_{-\frac{l_0}{2}}^{+\frac{l_0}{2}} dx \sqrt{|g_{11}(t-x,0)|} = \int_{-\frac{l_0}{2}}^{+\frac{l_0}{2}} dx \left[1 + \frac{h_{11}(t-x,0)}{2}\right] \tag{1.18}$$

Using equation 1.14 this gives

$$l(t) = l_0 + \frac{h^+}{2} \int_{-\frac{l_0}{2}}^{+\frac{l_0}{2}} dx \cos(\omega t - kx) \tag{1.19}$$

Then the change in path length is

$$\begin{aligned} \Delta l(t) \equiv l(t) - l_0 &= \frac{h^+}{2k}\left[\sin\left(\omega t + \frac{kl_0}{2}\right) - \sin\left(\omega t - \frac{kl_0}{2}\right)\right] \\ &= \frac{h^+}{k}\cos(\omega t)\sin\left(\frac{kl_0}{2}\right) \\ &= \Delta L \cos(\omega t) \end{aligned} \tag{1.20}$$

where $\Delta L \equiv \frac{\lambda h^+}{2\pi}\sin\left(\frac{\pi l_0}{\lambda}\right)$ is the amplitude of the oscillations. Therefore the strain amplitude is

$$\epsilon_x^+ = \frac{\Delta L}{l_0} = \frac{\lambda h^+}{2\pi l_0}\sin\left(\frac{\pi l_0}{\lambda}\right)$$

that is consistent with the nearby bodies explanation, tending to 1.16 when $l_0 \ll \lambda$.

We conclude that, according to equations 1.16, 1.17 and 1.20, under the effect of a $e^+_{\mu\nu}$ polarized gravitational wave, the proper distance between two nearby bodies varies in the plane perpendicular to the wave direction with

$$x(t) = x_0\left(1 + \frac{h^+}{2}\cos\omega t\right) \tag{1.21}$$

$$y(t) = y_0\left(1 - \frac{h^+}{2}\cos\omega t\right) \tag{1.22}$$

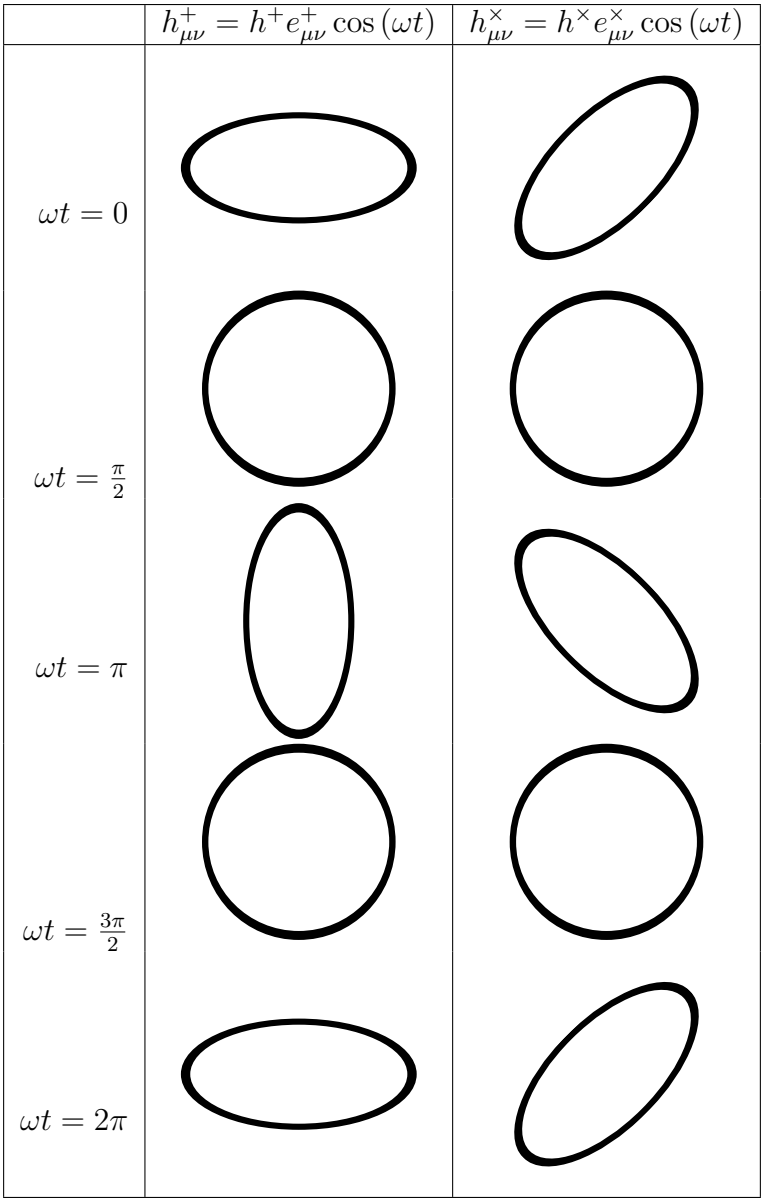


**Figure 1.1.:** The effect of gravitational waves in two different polarization ($e^{+}_{\mu\nu}$ and $e^{\times}_{\mu\nu}$) on a circle of test masses followed over one cycle. The wave is traveling along the $z$-axis, the paper is the $xy$-plane at $z = 0$, and the observer is looking towards the source.

# 2 The Search for Gravitational Waves

Now that we understand the effects of gravitational waves on the space-time, we need to look for the sources and to estimate the typical amplitude of their radiation when it reach the Earth.

In principle, gravitational waves can experience almost all the familiar peculiarities of propagation typical of electromagnetic waves. Nevertheless nobody has so far detected any direct evidence of gravitational waves.

A **direct detection** is defined as the measurement of the perturbation $h(t)$ as function of the time, while the term **indirect detection** refers to the observation of phenomena that suggest the presence of a gravitational radiation, without making possible any measurement of its waveform.

Even if, as of 2014, no direct detection of gravitational waves has yet been claimed, there are strong indications that such radiation exists, because at least a pair of sources may already has been detected.

## 2.1. The First Indirect Observation: PSR B1913+16

The most famous indirect detection dates back to 1974: it is the binary system made by pulsar *PSR B1913+16* and another neutron star, orbiting around their center of mass. The orbit period is $P_b = 7.75\,\mathrm{h}$ and the projected orbital velocity is $v \sim c/1000$: this suggest that there can be some measurable relativistic effects. Among the best known results are measurement of the general relativistic advance of periastron at a rate $\sim 35 \times 10^3$ times that of Mercury in the solar system and, above all, the effect of gravitational radiation damping, causing a measurable rate of orbital decay. [7]

Peters and Matthews [8] showed that, according to general relativity, the resulting rate of change in orbital period, measured in the orbiting system reference frame,

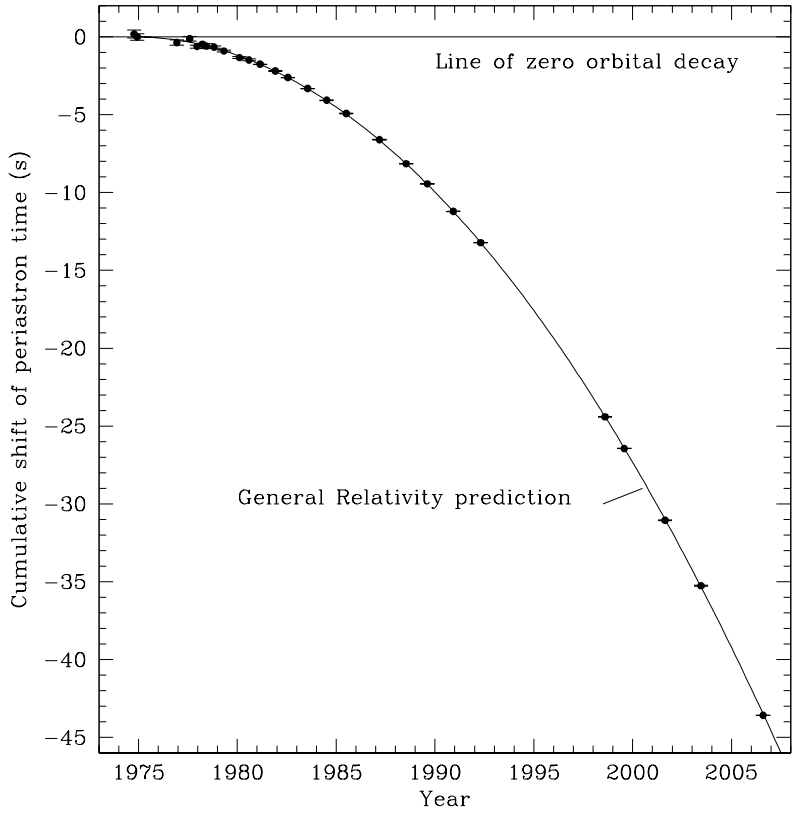


**Figure 2.1.:** Orbital decay caused by the loss of energy by gravitational radiation of PSR B1913+16 system. The parabola depicts the expected shift of periastron time relative to an unchanging orbit, according to general relativity. Data points represent Weisberg's measurements, with error bars mostly too small to see. [7]

should be proportional to

$$\dot{P}_b^{GR} \propto (P_b)^{-\frac{5}{3}}$$

obtaining for *PSR B1913+16* a current value of

$$\dot{P}_b^{GR} = (-2.402531 \pm 0.000014) \times 10^{-12}\,\mathrm{s/s}$$

This value is being measured since the discovery of these pulsars, as shown in Fig. 2.1. To properly compare the values, we have to take into account a small additional contribution $\Delta\dot{P}_b = (-0.027 \pm 0.005) \times 10^{-12}\,\mathrm{s/s}$ to the observed $\dot{P}_b$ due to the relative acceleration of that frame with respect to the solar system barycenter. The most recent measurement of $\dot{P}_b$ was made by Weisberg in 2010 [7] and the agreement with the predicted value is extraordinary:

$$\frac{\dot{P}_b - \Delta\dot{P}_b}{\dot{P}_b^{GR}} = 0.997 \pm 0.002 \tag{2.1}$$

This result provides conclusive evidence for the existence of gravitational radiation, as predicted by Einstein's theory.

## 2.2. BICEP2 and Inflationary Gravitational Radiation

The experiment BICEP2 is a Cosmic Microwave Background (CMB) polarimeter specifically designed to search for the signal of inflationary gravitational waves in the B-mode power spectrum around $\ell \sim 80$. Theoretically, inflation predicts that the quantization of the gravitational field coupled to exponential expansion produces a primordial background of stochastic gravitational waves with a characteristic spectral shape. These gravitational waves would have imprinted a unique signature upon the CMB. Gravitational waves induce local quadrupole anisotropies in the radiation field within the last-scattering surface, inducing polarization in the scattered light. This polarization pattern would include a "curl", or B-mode, component at degree angular scales that cannot be generated primordially by density perturbations. [9]

In March 2014, BICEP2 collaboration claimed the measurement of a large excess of signal in the power spectrum, compatible (with significance $> 5\sigma$ from the null hypothesis) with the presence of gravitational radiation. Of course, this result is very recent and still needs to be confirmed. In case, it would represent the second, independent evidence of the existence of gravitational waves.

## 2.3. Sources of Gravitational Waves

According to general relativity, gravitational waves are radiated by objects whose motion involves acceleration, provided that the motion is not perfectly spherically symmetric (like an expanding or contracting sphere) or cylindrically symmetric (like a spinning disk or sphere). More technically, in almost all situations the second time derivative of the quadrupole moment of an isolated system's stress-energy tensor must be nonzero in order for it to emit gravitational radiation. [10] This is analogous to the changing dipole moment of charge, or current, necessary for electromagnetic radiation.

Einstein's theory predicts that gravitational radiation is produced in extremely small quantities in ordinary atomic processes. The probability that a transition between two atomic states will proceed by emission of gravitational, rather than electromagnetic, radiation is of order $GE/e^2$, where $E$ is the energy released and $e$ is the elementary charge. For $E = 1\,\mathrm{eV}$ this probability is about $10^{-54}$. This also implies that gravitational waves are so weakly absorbed by matter that absorption has been important only near the Plank era of the big bang (i.e. $t \ll 10^{-43}\,\mathrm{s}$), and the same thing happens for their scattering and dispersion.

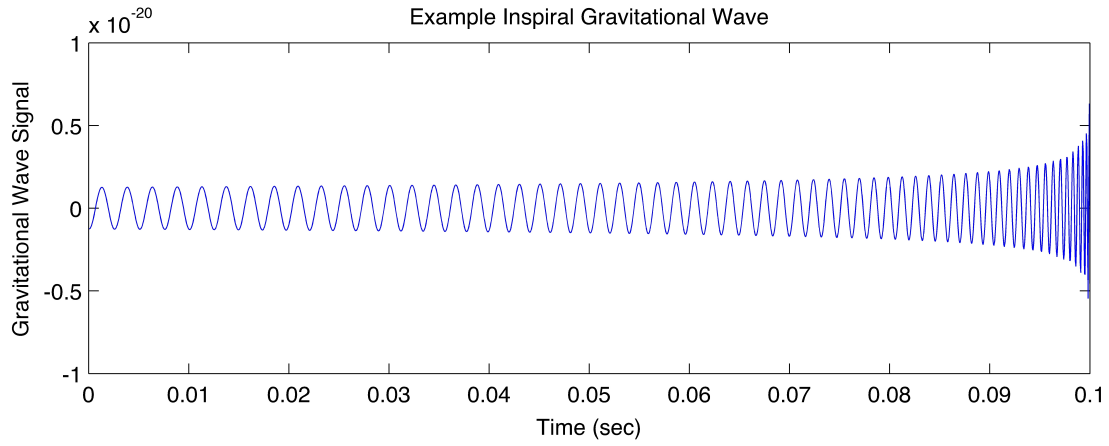


**Figure 2.2.:** Example of an inspiral gravitational wave from the coalescence of a binary system. [11]

The most energetic gravitational waves likely to be observed on Earth are those produced in near macroscopic events, i.e. stellar collapse in our galaxy. It can be useful to divide the waves (and the relative sources) in three classes:

- *bursts*, which last for only few cycles, or at most for times short, compared to a typical observing run;
- *periodic waves*, which are superposition of sinusoids with frequencies that are more or less constant over time, compared to an observing run;
- *stochastic waves*, which fluctuate stochastically and last for a time long compared to an observing run.

We briefly analyze some candidate sources of detectable gravitational radiation with some prediction of the properties of their waves. We will not explain the full details of achieved results, because often a simple treatment of the problem is not enough. Depending on the strength of the source, one can resort several degree of approximation. However it is important to remark that the strongest emitters, that are obviously the most interesting ones, are likely to violate our weak field assumptions. When there is no small parameter in which one can expand, the only way to compute the full details of the wave field emitted by them is by numerical techniques.

## 2.3.1. Burst Sources

### Coalescence of Compact Binaries

General relativity predicts that a point mass $m$ fixed in a rotating coordinate system at $(r = r_0, \theta = 0, \phi = 0)$ with angular velocity $\Omega$, losses energy through the emission

of gravitational radiation at twice the frequency of the orbit, with power

$$P(2\Omega) = \frac{32G\Omega^6 m^2 r_0^4}{5c^5} \tag{2.2}$$

A direct calculation of the power emitted by a planet orbiting around its star suggest that it is very weak: for example, Jupiter's loss of energy through gravitational radiation, because of its orbit around the Sun, is $\sim 5.3\,\mathrm{kW}$. [5]

However, this value can be significant if we study the behavior of binary system of massive stars orbiting around their center of mass, close enough to be driven into coalescence by gravitational radiation reaction, in a time less than the age of universe. These systems are usually two neutron stars, two black holes, or a neutron star and a black hole whose orbits have degraded to the point that the two masses are about to coalesce. In this phase the system generates spiral gravitational waves. The binary star system *PSR B1913+16* is an example of such a system.

As the two masses rotate around each other, their orbital distances decrease and their speeds increase: this causes the frequency of the gravitational waves they emit to increase up to $f \simeq 1\,\mathrm{kHz}$ (in the most common case of two neutron stars) until the two objects definitively merge into one. An example of the expected signal from an event of this kind is shown in Fig. 2.2.

The characteristic amplitude of the burst waves at a distance $r$ from the source can be obtained with this relation:

$$h_c \sim 10^{-22} \left(\frac{M}{M_\odot}\right)^{\frac{1}{3}} \left(\frac{\mu}{M_\odot}\right)^{\frac{1}{2}} \left(\frac{100\,\mathrm{Hz}}{f_c}\right)^{\frac{1}{6}} \left(\frac{100\,\mathrm{MPc}}{r}\right) \tag{2.3}$$

where $M$ and $\mu$ are respectively the total mass of the system and the reduced mass (expressed in solar masses), and $f_c$ is a characteristic frequency of the waves. [10]

At present, there are significant uncertainties in the astrophysical rate predictions for compact binary coalescences. A realistic estimation of double neutron star system coalescence rate is $\sim 100\,\mathrm{Myr}^{-1}$ for a galaxy similar to Milky Way that corresponds to volumetric rate of $\sim 1\,\mathrm{Mpc}^{-3}\,\mathrm{Myr}^{-1}$. [1] For example, the aforementioned *PSR B1913+16* binary system is going to coalesce in $\sim 300\,\mathrm{Myr}$.

### Supernovae

In general, a type II supernova will emit gravitational radiation, except in the unlikely event that the explosion is perfectly symmetric. There have been several attempts to simulate the waveform of such an event, and the expected signature is now pretty well known. An example is given in Fig. 2.3: according to this model, the maximum

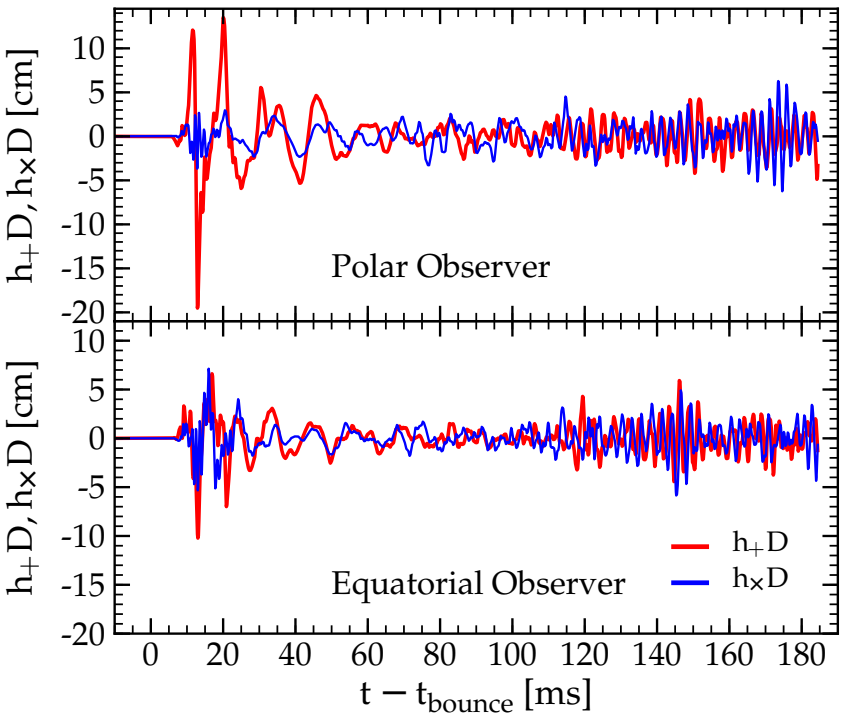


**Figure 2.3.:** Gravitational wave polarizations $h^+$ and $h^\times$ (rescaled by distance $D$) obtained in a simulation (Ott et al., 2013 [12]) as a function of post-bounce time seen by and observer on the pole ($\theta = 0$, $\phi = 0$; top panel) and on the equator ($\theta = \pi/2$, $\phi = 0$; bottom panel)

amplitude of waves is expected to be $h \approx 20\,\mathrm{cm}/D$, that correspond to $h \approx 10^{-22}$ at a distance $D = 10\,\mathrm{kpc}$.

A more generic formula to obtain the order of magnitude of $h$ at a distance $r$ from the source is

$$h_c \sim 2.7 \times 10^{-20} \left(\frac{E_{GW}}{M_\odot}\right)^{\frac{1}{2}} \left(\frac{1\,\mathrm{kHz}}{f_c}\right)^{\frac{1}{2}} \left(\frac{10\,\mathrm{Mpc}}{r}\right) \tag{2.4}$$

where $E_{GW}$ is the energy emitted through gravitational radiation by the supernova, expressed in solar masses, and $200\,\mathrm{Hz} \lesssim f_c \lesssim 10\,\mathrm{kHz}$ is the characteristic frequency of the waves in these events. [10] Its value depends strongly on the asymmetry of the explosion. Recent simulations indicate an expected value of $E_{GW} \sim 10^{-8} M_\odot$. [13]

## 2.3.2. Periodic Sources

### Pulsars

Pulsars are highly magnetized, rotating neutron stars. Possible asymmetries in mass distribution lead to the emission of gravitational radiation. The larger are those

asymmetries and the more rapidly they rotate, the stronger will be the radiation. Due to their high stability, pulsars are hypothesized to emit continuous, narrow-band, quasi-sinusoidal gravitational waves.

These sources are expected to produce comparatively weak gravitational waves since they evolve over longer periods of time, and are usually less catastrophic than inspiral or burst sources. The characteristic amplitude of these waves, measured at a distance $r$ from the pulsar rotating around $z$-axis, can be obtained as

$$h_c \sim 8 \times 10^{-20} \epsilon \left( \frac{I_{zz}}{10^{38}\,\mathrm{kg\,m^2}} \right) \left( \frac{f}{1\,\mathrm{kHz}} \right)^2 \left( \frac{10\,\mathrm{kpc}}{r} \right) \tag{2.5}$$

with fiducial equatorial gravitational ellipticity $\epsilon$ defined as

$$\epsilon = \frac{Q_{xx} - Q_{yy}}{I_{zz}}$$

where $Q_{xx}$ and $Q_{yy}$ are quadrupole moments with respect to $x$ and $y$ axes, and $I_{zz}$ is the moment of inertia around $z$-axis. [10]

Equation 2.5 leads to expected amplitudes $h \sim 10^{-24 \div 25}$ for the most interesting known pulsars, in the limit case in which they loss energy only through the emission of gravitational radiation. Despite the weakness of the waves, in principle the signal can be seen averaging it over many periods. Actually known pulsars usually have precisely determined frequency evolutions and sky-positions making them ideal targets for gravitational wave detectors. If a pulsar is monitored regularly through electromagnetic observations it can yield a coherent phase model, which allows gravitational wave data to be coherently integrated over months or years. [14]

### Ordinary Binary Stars

Ordinary binary star systems are the most reliably understood sources of gravitational waves. From the measured mass and orbital parameters of a binary and its estimate distance, one can compute with confidence the details of its waves.

Unfortunately, ordinary binaries have orbital periods usually longer than an hour, that correspond to $f \sim 1\,\mathrm{mHz}$. Because of seismic noise, detectors in earth laboratories cannot hope to see waves at such low frequencies.

The characteristic amplitude of such waves measured at a distance $r$ from the source is

$$h_c \sim 10^{-20} \left( \frac{M}{M_\odot} \right)^{\frac{2}{3}} \left( \frac{\mu}{M_\odot} \right) \left( \frac{f_c}{10\,\mathrm{mHz}} \right)^{\frac{2}{3}} \left( \frac{100\,\mathrm{pc}}{r} \right) \tag{2.6}$$

where $f_c$ is twice the frequency of the orbit. [10]

### 2.3.3. Stochastic Background

The discovery of the CMB in 1964 suggests that there can be a gravitational analogous. This type of background is called *Stochastic Gravitational-Wave Background* (SGWB) and could be the result of processes that took place very shortly after the Big Bang, but since we know very little about the state of the universe at that time, it is hard to make predictions.

While the evolution of the universe following the *Big Bang Nucleosynthesis* (BBN) is well understood, there is little observational data probing the evolution prior to BBN, when the universe was less than one minute old. The gravitational wave spectrum should carry information about exactly this epoch of the universe evolution.

Nevertheless, such a background might also arise from processes that take place fairly recently (within the past several billion years) and this more recent contribution might overwhelm the parts of the background which contain information about the state of the early universe. [15]

The spectral properties of the stochastic background are characterized by the density parameter $\Omega_{GW}(\nu)$, a dimensionless value defined as

$$\Omega_{GW}(\nu) = \frac{1}{\rho_{cr}} \frac{d\rho_{GW}}{d\ln\nu}$$

where $\rho_{cr}$ is the critical energy-density required to just close the universe and $d\rho_{GW}$ is the energy density of gravitational radiation contained in frequency range $\nu$ to $\nu + d\nu$. [16] This parameter is one of the contribute to the sum in Friedmann equation (assuming the universe to be flat)

$$\sum_i \Omega_i + \Omega_\Lambda = 1 \tag{2.7}$$

where $\Omega_i$ are the density parameters for the various matter species and $\Omega_\Lambda$ for the cosmological constant.

It is hard to make a theoretical estimation of this density parameter, but an upper limit can be obtained from direct and indirect measurements. If we assume $\Omega_{GW}(\nu)$ to be constant, i.e. a frequency independent gravitational wave spectrum, experimental results of LIGO and Virgo give an upper limit (95% CL) of its value: $\Omega_{GW} < 6.9 \times 10^{-6}$. Other upper limits achievable with several theoretical models and some experiments are presented in Fig. 2.4.

The network of advanced detectors actually under development will be able to probe the isotropic SGWB at the level of $\Omega_{GW} \sim 10^{-9}$ or smaller. [17]

### 2.3.4. The Impracticality of Artificial Sources

No artificial generator of gravitational waves seems practicable. For example, consider a dumbbell consisting of two masses of $10^3$ kg each, at either ends of a 2 m-long rod,

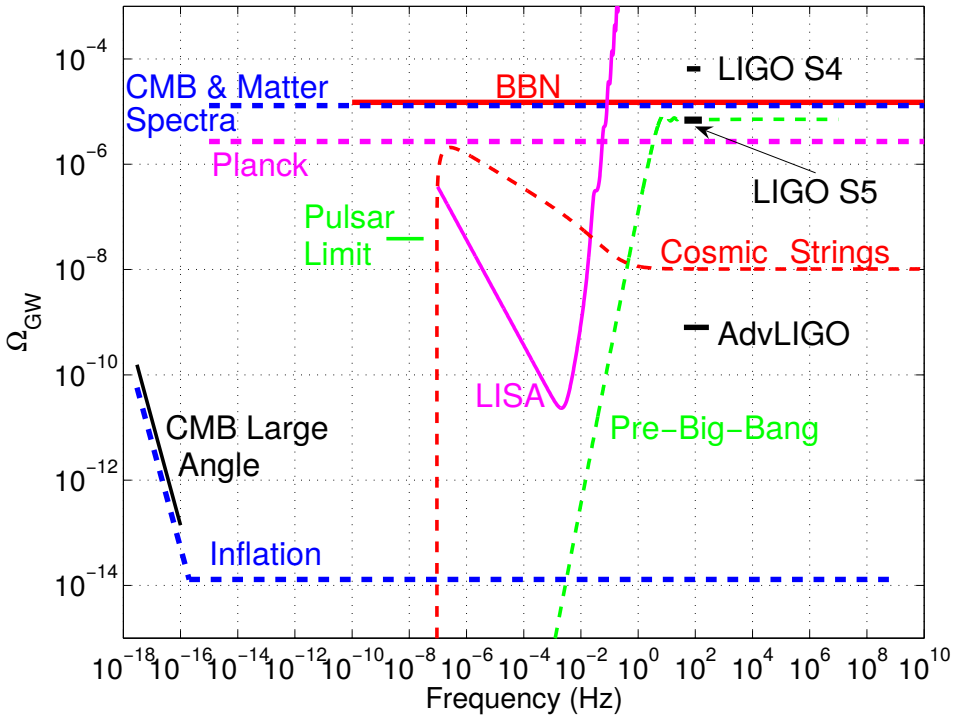


**Figure 2.4.:** Comparison of different SGWB density parameter upper limits, according measurements and models. Note that the BBN and CMB bounds apply only to backgrounds generated prior to the BBN and the CMB decoupling respectively, while the LIGO bound also probes the SGWB produced later (for example in "cosmic strings" model). [17]

that spins about an axis orthogonal to the connecting rod passing through the center of mass, at frequency $f = 10\,\mathrm{kHz}$. Neglecting for simplicity the contribution of the connecting rod (that would be of course subjected to a huge tension), the amplitude of the gravitational waves generated by this device will be

$$h = 2.6 \times 10^{-33} \left( \frac{1\,\mathrm{m}}{r} \right)$$

Now, the "wave zone" approximation is valid for $r > 30\,\mathrm{km}$, where $h \sim 10^{-37}$, 15 magnitudes lower than any astronomical source.

In the 1980s, gravitational wave emissions from the particle beams in high energy accelerators, as well as from nuclear explosion, have also been evaluated, and found wanting. [18] It is the reason that experimental study of gravitational waves is directed toward astronomical sources, that generate, by far, the strongest gravitational waves we are likely to encounter. [19]

## 2.4. Detectors of Gravitational Waves

A gravitational-wave detector is any device designed to measure gravitational waves. Since the 1960s gravitational-wave detectors have been built and constantly improved. Some types of detectors, both proposed and realized, are here grouped according to their bandwidth:

- *High frequency detectors*: Weber bar, interferometer, super-fluid interferometers and superconducting circuits.
- *Low frequency detectors*: Doppler tracking of spacecraft, interferometer in space, Earth's normal modes, Sun's normal modes, vibration of blocks of the Earth's crust, skyhook.
- *Very low frequency detectors*: pulsar timing, timing of orbital motions, anisotropies in the temperature of the cosmic microwave radiation (indirect detection).

Note that, due to the stochastic movements of the ground, only high-frequency detectors can be earth-based. The most common types of detectors are resonant bars (aka Weber bars) and interferometers.

### 2.4.1. Weber Bars

Resonant bars have represented the first type of gravitational-wave detector. A large, solid bar of metal isolated from outside vibrations, designed to detect the expected wave motion is called a Weber bar. Strains in space due to an incident gravitational wave excite the resonant frequency of the bar, and these vibrations could be amplified to detectable levels. When a burst of gravitational waves hits and excites the oscillator, this will vibrate for a time span much longer than the duration of the burst (typically 1ms), thus allowing the extraction of the signal from the detector noise. [20] Their sensitivity is limited to a very narrow bandwidth, so that Weber bars are not sensitive enough to detect anything but extremely powerful gravitational waves.

For example, *AURIGA* (Antenna Ultracriogenica Risonante per l'Indagine Gravitazionale Astronomica) is an ultracryogenic resonant bar gravitational wave detector in Italy. It is located at the Laboratori Nazionali di Legnaro of the INFN. Nowadays, the other working experiments are *MiniGrail* (Netherlands) and *Mario Schenberg* (Brazil).

### 2.4.2. Interferometers

Interferometric detectors are the most interesting devices ever conceived to detect gravitational waves. Indeed we can determine the distance between two test masses (nothing more than mirrors) by measuring the round trip travel time of light beams

sent over large distances, and thus it is natural to aim at Michelson interferometer. The key difference with the 1887 interferometer is that here we need not connect the mirrors in a single rigid structure, but each mass is left in free fall, so that it responds in a indepentend way to gravitational effects.

We can calculate the time that it takes to that ray to travel in each arm of our interferometer, when it is crossed by a gravitational wave. In equations 1.21 and 1.22 We have already seen the effect on the distance between two points; in a Michelson interferometer the arms are orthogonal and their lengths $L$ equal each other ($L = x_0 = y_0$), so that the relative variation

$$\begin{aligned} \Delta L(t) &= 2[x(t) - y(t)] = 2L \cdot h^{+} \cos \omega t \\ &= 2L \cdot h(t) \end{aligned} \tag{2.8}$$

where the additional factor 2 takes into account for the round trip in the interferometer, and $h(t) = h^{+} \cos \omega t$. Remembering that for light $ds^2 = 0$, this correspond to a difference in time of arrival

$$\begin{aligned} \Delta\tau(t) &= \frac{\Delta L(t)}{c} = \frac{2L}{c} h(t) \\ &= \tau_0 \cdot h(t) \end{aligned} \tag{2.9}$$

where $\tau_0$ is the travel time in absence of gravitational radiation. Corrections to this due to the effect of the gravitational wave itself are negligible. [19] We can also express 2.9 as a phase shift:

$$\Delta\varphi(t) = \frac{2\pi c}{\lambda_L} \tau_0 \cdot h(t) \tag{2.10}$$

where $\lambda_L$ is the wavelength of the light used in the interferometer. It is clear that the effect is directly proportional to $h$: this immediately says that the longer the optical path in the apparatus, the larger will be the phase shift due to the gravitational wave.

This scaling law doesn't hold for arbitrarily long arms because, on the other hand, this reduces the bandwidth of our experiment. Indeed, for $\lambda_{GW} \sim L$ the approximation done to get equations 1.21 and 1.22 is no longer valid. Using the correct physical description in equation 1.20, we can get a graph of the sensitivity of a Michelson interferometer, expressed in $\Delta\varphi$ per $h$ unit as function of $f_{GW}$. It is shown in Fig. 2.5, for several values of $L$: looking at the behavior at high frequencies, given a certain $f_{GW}$ there is a $L$ beyond which there are no further gains.

Of course, the feasibility of a earth-based interferometer with $L > 5$km is almost null, at least for the cost. Luckily an optical arrangement could come to the aid of us: implementing two Fabry-Pérot cavities in both Michelson interferometer arms,

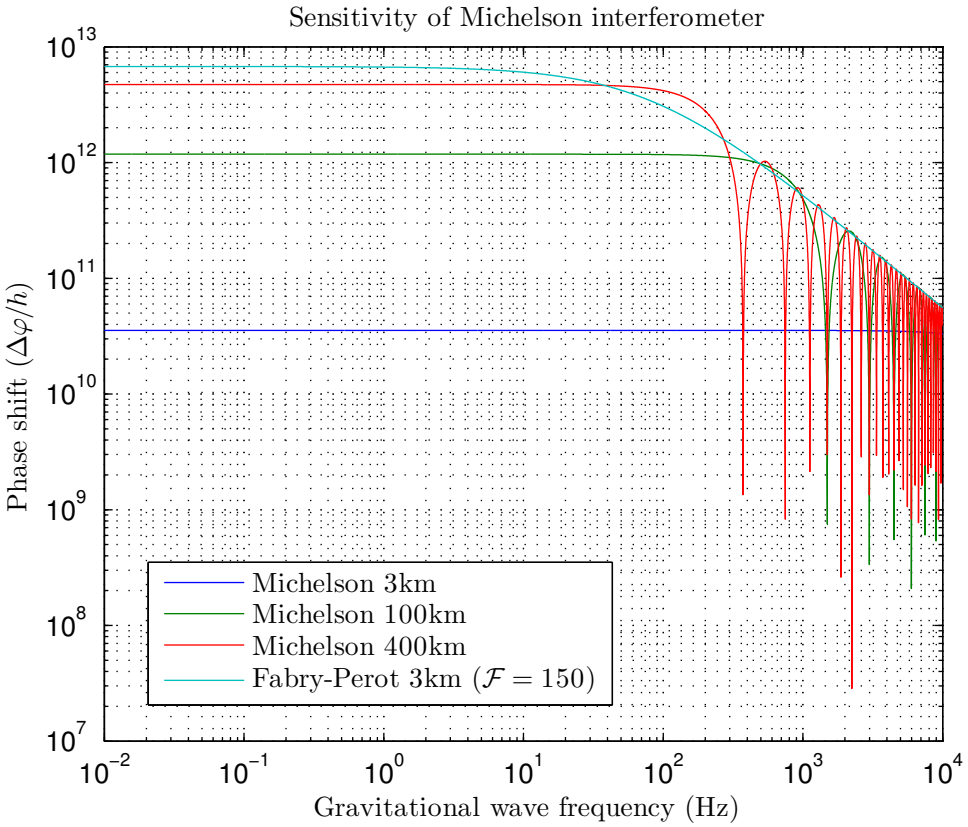


**Figure 2.5.:** Phase shift per $h$ unit $\left(\frac{\Delta\varphi}{h}\right)$ in a $L$-long Michelson interferometer as function of $f_{GW}$. The light has wavelength $\lambda_L = 1.064\,\mu\text{m}$. The peaks correspond to $\lambda_{GW} = L/n$ with $n \in \mathbb{N}$, when a whole numbers of waves fit into the interferometer, canceling the effects. [21]

we achieve the same performance of a longer interferometer. In brief, photons are trapped in the cavities for an average time

$$\tau_s = \frac{2L}{c}\frac{\mathcal{F}}{\pi} \tag{2.11}$$

or, in other words, travel $\mathcal{F}/\pi$ times through the cavity before to come out. The quantity $\mathcal{F}$ is a quality index of the cavity, and it is called *finesse*. From Fig. 2.5, it is shown as the sensitivity of a 3km long interferometer with $\mathcal{F} = 150$ Fabry-Pérot cavities is roughly equivalent to a 400 km standard interferometer.

So far there have been at least 4 working interferometric detectors: *LIGO* (USA, 3 detectors in 2 sites), *VIRGO* (Italy), *GEO 600* (Germany), and *TAMA 300* (Japan). An interesting experiment is *eLISA*: it will be the first dedicated space-based gravitational wave detector, using laser interferometry to monitor the fluctuations in the relative distances between three spacecrafts, arranged in an equilateral triangle with $10^9$ m arms (almost the diameter of the Sun).

# Part II.

# Accelerometer Control

# 3 An Introduction to Control Theory

Feedback is a central feature of life. The process of feedback governs how we grow, respond to stress and challenge, and regulate factors such as body temperature, blood pressure and cholesterol level. The mechanisms operate at every level, from the interaction of proteins in cells to the interaction of organisms in complex ecologies.

Nowadays feedback controls are essential in any field of science and engineering. Also Virgo contains several control systems. The highest level is represented by a closed loop control system that is used both during the lock acquisition of the interferometer and the steady state (*science mode*) operations. It must be capable of the maintaining the interferometer controlled at the design sensitivity with good stability and duty cycle. It controls the position of the optical elements of the interferometer, which in turn are controlled by other local closed loop control systems. Also further levels of control exist: for example, the accelerometers used in Virgo seismic isolation system use a feedback control to work to the best of their abilities.

In this chapter we introduce some basic concepts of control theory applied to continuous-time systems. Later, these basis will be extended to discrete-time systems.

## 3.1. Linear Time-Invariant Systems

It is possible to distinguish two main classes of systems:

- *linear systems*
- *nonlinear systems*

A system is called linear if the superposition principle applies. The superposition principle states that *the net response at a given place and time, caused by two or more stimuli, is the sum of the responses which would have been caused by each stimulus individually.* Hence, for a linear system, the response to several inputs can be calculated by treating one input at a time and adding the results. It is this

principle that allows one to build up complicated solutions to the linear differential equation from simple solutions. In an experimental investigation of a dynamic system, if cause and effect are proportional, thus implying that the superposition principle holds, then the system can be considered linear.

A differential equation is linear if its coefficients are constants or functions only of the independent variable. Dynamic systems that are composed of linear time-invariant lumped-parameter components may be described by linear time-invariant differential equations - i.e. constant-coefficient differential equations. Such systems are called *Linear Time-Invariant systems* (or *LTI* systems). On the other hand, systems that are represented by differential equations whose coefficients are functions of time are called *linear time-variant systems*. [22]

Eventually, systems that does not satisfy the superposition principle, which means that the output is not directly proportional to the input, are called *nonlinear systems*.

## 3.2. Transfer Functions

In control theory, functions called *transfer functions* are commonly used to characterize the input-output relationships of components or systems that can be described by linear, time-invariant, differential equations. They are defined as the ratio of the Laplace transform of the output (response function) to the Laplace transform of the input (driving function) under the assumption that all initial conditions are zero. Laplace transform $\mathcal{L}[\cdot]$ and its inverse transform $\mathcal{L}^{-1}[\cdot]$ are defined in Appendix A, together with some properties.

Consider the linear time-invariant system defined by the following differential equation:

$$a_n \overset{(n)}{y} + a_{n-1} \overset{(n-1)}{y} + \ldots + a_1 \dot{y} + a_0 y = b_m \overset{(m)}{x} + b_{m-1} \overset{(m-1)}{x} + \ldots + b_1 \dot{x} + b_0 x \quad (3.1)$$

where $y = y(t)$ is the output of the system and $x = x(t)$ is the input. The transfer function $G(s)$ of this system is

$$G(s) = \frac{Y(s)}{X(s)} = \frac{b_m s^m + b_{m-1} s^{m-1} + \ldots + b_1 s + b_0}{a_n s^n + a_{n-1} s^{n-1} + \ldots + a_1 s + a_0} = \frac{\sum_{i=0}^{m} b_i s^i}{\sum_{j=0}^{n} a_j s^j} \quad (3.2)$$

where $X(s) = \mathcal{L}[x]$ and $Y(s) = \mathcal{L}[y]$ .

A common notation convention, where lower case letters denote signals and capital letters their Laplace transforms, is used in the thesis. Furthermore, in order to obtain a lighter notation, the explicit dependence of signals on time $t$ will be usually omitted, as also the explicit dependence of their Laplace transforms on $s$.

By using the concept of transfer function, it is possible to represent system dynamics by algebraic equations in $s$. If the highest power of $s$ in the denominator of the transfer function is equal to $n$, the system is called an $n^{th}$-order system.

It follows from equation 3.2 that the output can be written as

$$Y = G \cdot X \tag{3.3}$$

From convolution theorem we know that

$$x * y = \mathcal{L}^{-1}\left[\mathcal{L}\left[x\right] \cdot \mathcal{L}\left[y\right]\right] = \mathcal{L}^{-1}\left[X \cdot Y\right] \tag{3.4}$$

Applying the inverse Laplace transform to both sides of 3.3, and using 3.4, we find the relation between input and output in time domain

$$\begin{aligned} y\left(t\right) &= \int_{-\infty}^{+\infty} x\left(\tau\right) g\left(t-\tau\right) d\tau \\ &= \int_{-\infty}^{+\infty} g\left(\tau\right) x\left(t-\tau\right) d\tau \end{aligned} \tag{3.5}$$

where $g\left(t\right) = \mathcal{L}^{-1}\left[G\left(s\right)\right]$, and both $g\left(t\right)$ and $x\left(t\right)$ are 0 for $t < 0$. The function $g\left(t\right)$ represents the impulse response of the system: applying an unit-impulse input $x\left(t\right) = \delta\left(t\right)$ to the system indeed, equation 3.5 states that $y\left(t\right) = g\left(t\right)$. Similarly, $G\left(s\right)$ is the unit-impulse response in frequency domain.

If the transfer function of a system is unknown, it is hence possible to obtain complete information about the dynamic characteristics of the system by exciting its input with an impulse or with white noise, and measuring the response at the output. The Laplace transform of the output is the transfer function of that system, and it gives a full description of the dynamic characteristics of the system. Of course this method can be used also to check the goodness of a mathematical model of the system. [22]

Also other forms of mathematical models exist. For example, often it is advantageous to use **state-space representation**: it consists of 4 matrices ($A$, $B$, $C$ and $D$) that, if $u$ is the input vector, $y$ is the output vector and $x$ is the state vector, represent the state in this form:

$$\begin{aligned} \dot{x}\left(t\right) &= A\left(t\right) x\left(t\right) + B\left(t\right) u\left(t\right) \\ y\left(t\right) &= C\left(t\right) x\left(t\right) + D\left(t\right) u\left(t\right) \end{aligned}$$

Unlike the frequency domain approach, the use of the state space representation is not limited to systems with linear components and zero initial conditions. This representation is extensively used in Virgo control systems.

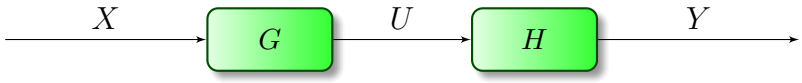


**Figure 3.1.:** Series connection

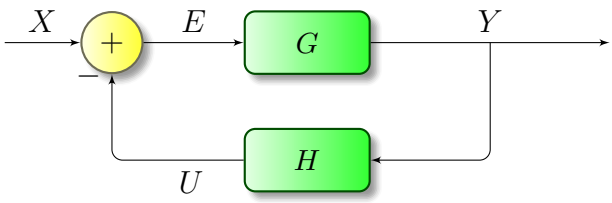


**Figure 3.2.:** Closed loop system

## 3.3. Feedback Control Systems

A system with transfer function $H$ can be connected in cascade to a system described by $G$, as depicted in Fig. 3.1. The output of $G$ and the input of $H$ must have the same physical dimension. We will always assume also that the input impedance of $H$ (that is a measure of how much a structure opposes motion when subjected to a given force) is much higher than the output impedance of $G$. Under this hypothesis, the transfer function $T$ of the new system is given by the product

$$T = \frac{Y}{X} = G \cdot H \tag{3.6}$$

If the assumption on the impedances is not valid, so the presence of $H$ modifies the behavior of $G$, and equation 3.6 is no longer valid. An extension of the concept of electrical impedance to a mechanical system can be found in Appendix B.

A widely used configuration is when one or more systems are connected to form a *feedback control system*, often referred to as a *closed-loop control system*, i.e. when the output of a system $G$ is fed back (directly or filtered by another system $H$) to a summing point with the input, as shown in Fig. 3.2.

The output of $G$ and the input of $H$ must have the same physical dimension, and of course also the output of $H$ and the input of $G$. The output of the sum $E$ is called *error signal*. The closed loop system in Fig. 3.2 is equivalent to a system whose transfer function $T$ is, subject to the similar conditions on impedances previously mentioned,

$$T = \frac{Y}{X} = \frac{G}{1 + G \cdot H} \tag{3.7}$$

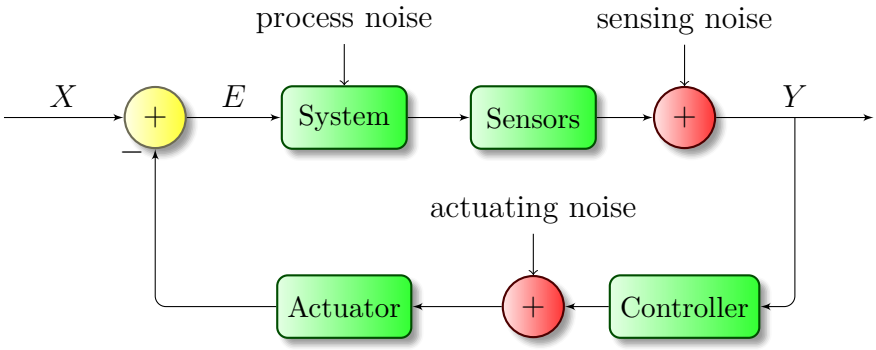


**Figure 3.3.:** Real closed loop system

if $e = x - u$, and is called the *closed-loop transfer function*. Otherwise, if $e = x + u$,

$$T = \frac{Y}{X} = \frac{G}{1 - G \cdot H} \tag{3.8}$$

The ratio of the feedback signal $U$ to the error signal $E$ is called the *open-loop transfer function*:

$$\frac{U}{E} = G \cdot H \tag{3.9}$$

The key role of the feedback element $H$ is to modify the output before it is compared with the input, so as to bring the output of the system to a desired behavior.

### 3.3.1. Actual Feedback Controls

A modern controller senses the operation of a system, compares it against the desired behavior, computes corrective actions based on a model of the system response to external inputs and actuates the system to effect the desired change. This basic feedback loop of sensing, computation and actuation is the central concept in control.

A typical example of a real control system is shown in Fig. 3.3. It can be decomposed in two parts: a *plant*, which is assumed to be given and unalterable, and is represented by a physical system and some noisy sensors; a *controller*, which is the dynamic system that is to be designed, and that consists of a filter and an actuator. In modern control systems, computation of the feedback filter is typically implemented on a DSP or in a computer, requiring the use of Analog-to-Digital (ADC) and Digital-to-Analog (DAC) converters.

Uncertainty enters the system through noise in sensing and actuating subsystems, external disturbances that affect the feedback system operation and uncertain dynamics in the system (parameter errors, unmodeled effects, etc.).

### 3.3.2. Advantages and Disadvantages

An advantage of the closed-loop control system is that the use of a well designed feedback makes the system response relatively insensitive to external disturbances and internal variations in system parameters that always occur. It is thus possible to use relatively inaccurate and inexpensive components to obtain the accurate control of a given plant, whereas doing so is impossible in the open-loop case.

On the other hand, stability is a major problem in the closed-loop control system, which may tend to over correct errors, thereby causing instability. An open-loop control system is easier to build because system stability is not a major problem: a series connection of two stable system is always stable. [22]

Moreover, the actuation of a feedback control usually introduces unwanted noise to the system. The signal-to-noise ratio cannot be improved using a feedback control. This can be proved analytically or just following a simple idea: a controller is not able to distinguish signal from noise. It amplifies and processes everything without distinctions. It's important to remember this: the purpose of a feedback control is not the improvement of the Signal-to-Noise Ratio (SNR).

## 3.4. Stability of a Linear System

There are several ways to investigate the stability of a closed-loop system. Let's take into account the denominator $1 + G \cdot H$ of the transfer function 3.7. The equation

$$1 + G \cdot H = 0 \tag{3.10}$$

is called *characteristic equation* of the system. Its roots are called poles of the system and their position in $s$ plane strongly determines the stability of the system. It's possible to demonstrate that a system is stable if and only if all of them lie in the left-half $s$ plane.

### 3.4.1. Nyquist Stability Criterion

The *Nyquist stability criterion* is a powerful tool to analyze the stability of a system using its open-loop transfer function. It states that

> *the closed-loop system is stable if and only if the graph in the s plane of the open-loop transfer function* $G(i\omega) \cdot H(i\omega)$ *for* $-\infty < \omega < +\infty$, *encircles the point* $-1$ *as many times anticlockwise as* $G(s) \cdot H(s)$ *has right half-plane poles (provided that there are no hidden unstable modes caused by unwanted cancellations of poles and zeros in the closed-loop system). [23]*

# 4 Digital Filters

Despite the work of this thesis consists in the implementation of a digital filter, the techniques so far described are to be applied to analog systems. Luckily it is quite simple to extend these concepts to the digital world, also because often digital signals are derived from analog signals by periodic sampling. Almost everything in continuous-time systems has a counterpart in discrete-time systems.

In this chapter are presented definitions and basic techniques to handle a digital system, that will be used later in this thesis.

## 4.1. Definitions

Before continuing, it is useful to make some definitions. It's possible to distinguish two families of signals:

- *continuous-time signals*, defined at any value of the time variable $t$, and thus represented by continuous variable functions;
- *discrete-time signals*, defined only at discrete times and so represented as sequences of number.

Furthermore, also the amplitude of the signals can be either continuous or discrete. So, signals are also grouped in:

- *analog signals*, when both time and amplitude are continuous;
- *digital signals*, when both time and amplitude are discrete.

Similarly, *continuous-time systems* are systems for which both the input and output are continuous-time signals and *discrete-time systems* are those for which the input and output are discrete-time signals; *analog systems* are systems for which the input and output are analog signals and *digital systems* are those for which both input and output are digital signals.

## 4.2. Linear Shift-Invariant Systems

As we have already seen, it is very useful to study a system in the frequency domain using Laplace transform: the first thing to do is to extend it to discrete-time signals. For discrete-time systems, the natural replacement is the *Z-transform* $\mathcal{Z}[\cdot]$, defined in Appendix A together with some properties.

An important class of discrete-time systems is represented by the *Linear Shift-Invariant systems* for which the input $x(n)$ and the output $y(n)$ satisfy an $N^{th}$-order linear constant-coefficient difference equation of the form

$$\sum_{k=0}^{N} a_k y(n-k) = \sum_{r=0}^{M} b_r x(n-r) \tag{4.1}$$

Shift-invariant means that if $y(n)$ is the response to $x(n)$, then $y(n-k)$ is the response to $x(n-k)$, $\forall k \in \mathbb{Z}$. This class of system is the analogous, in the digital domain, of LTI systems described by equation 3.1.

Similarly to 3.2, the transfer function of a linear shift-invariant system is defined as the ratio of the Z-transform of the output to the Z-transform of the input:

$$G(z) = \frac{Y(z)}{X(z)} = \frac{\sum_{i=0}^{M} b_i z^{-i}}{\sum_{j=0}^{N} a_j z^{-j}}$$

where we have used the Z-transform time shifting property $\mathcal{Z}[y(n-k)] = z^{-k}\mathcal{Z}[y(n)]$. As for Laplace transform, $G$ represents also the Z-transform of the response to the unit-sample sequence

$$\delta(n) = \begin{cases} 1 & \text{if } n = 0 \\ 0 & \text{if } n \neq 0 \end{cases} \tag{4.2}$$

whose Z-transform is $\mathcal{Z}[\delta(n)] = 1$.

## 4.3. Design of Digital Filters from Analog Filters

The traditional approach to the design of digital filters involves the transformation of an analog filter into a digital filter, meeting prescribed specifications. This is a reasonable approach because:

1. the art of analog filter design is highly advanced and it is favorable to utilize the design procedures already developed for analog filters, that usually are rather simple to implement;

2. in many applications it is interesting to use a digital filter to simulate the performance of an LTI analog filter.

Transforming an analog system to a digital system is tantamount to obtain a discrete-time transfer function $G_d(z)$ from a continuous-time transfer function $G_a(s)$. In such transformation we generally require that the essential properties of the analog frequency response be preserved in the frequency response of the resulting digital filter. Loosely speaking, this implies that we want the imaginary axis of the $s$-plane to map into the unit circle of the $z$-plane. A second condition is that a stable analog filter should be transformed to a stable digital filter. That is, if the analog system has poles only in the left-half $s$-plane, then the digital filter must have poles only inside the unit circle. [24] A common procedure that satisfies these requirements is called *bilinear transformation* and it is described in sec. A.3. It states that is possible to obtain $G_d(z)$ from $G_a(s)$ with these two conditions by the substitution

$$s \to \frac{2}{T}\frac{1-z^{-1}}{1+z^{-1}} \tag{4.3}$$

where $T$ is the sampling period. It's easy to prove that the $s$-plane imaginary axis is mapped in the $z$-plane unit circle. Indeed, according to equation 4.3, points in the unit circle, where

$$z = e^{i\omega_d T} \tag{4.4}$$

are mapped in purely imaginary $s = i\omega_a$:

$$s = \frac{2}{T}\frac{1-e^{-i\omega_d T}}{1+e^{-i\omega_d T}} = i\frac{2}{T}\tan\left(\frac{T}{2}\omega_d\right) = i\omega_a$$

That is, the discrete-time filter behaves at frequency $\omega$ the same way that the continuous-time filter behaves at frequency $\omega_a$

$$\omega_a = \frac{2}{T}\tan\left(\frac{T}{2}\omega_d\right) \tag{4.5}$$

This means that every feature that is visible in the frequency response of the continuous-time filter is also visible in the discrete-time filter, but at a different frequency, as shown in the example in Fig. 4.1. This effect of the bilinear transformation is called *frequency warping*, and it can be neglected for frequencies $\omega_d \ll 2/T$, where $\omega_d \approx \omega_a$. However some applications inside Virgo require a so high precision that this effect must be considered: for example there are some high-Q notch filters whose cut-frequencies must to be placed with very high precision. This is done by *pre-warping* the filter design, that is designing the continuous-time filter to compensate for this effect.

The periodicity of equation 4.5 is a direct consequence of the aliasing predicted by Nyquist sampling theorem.

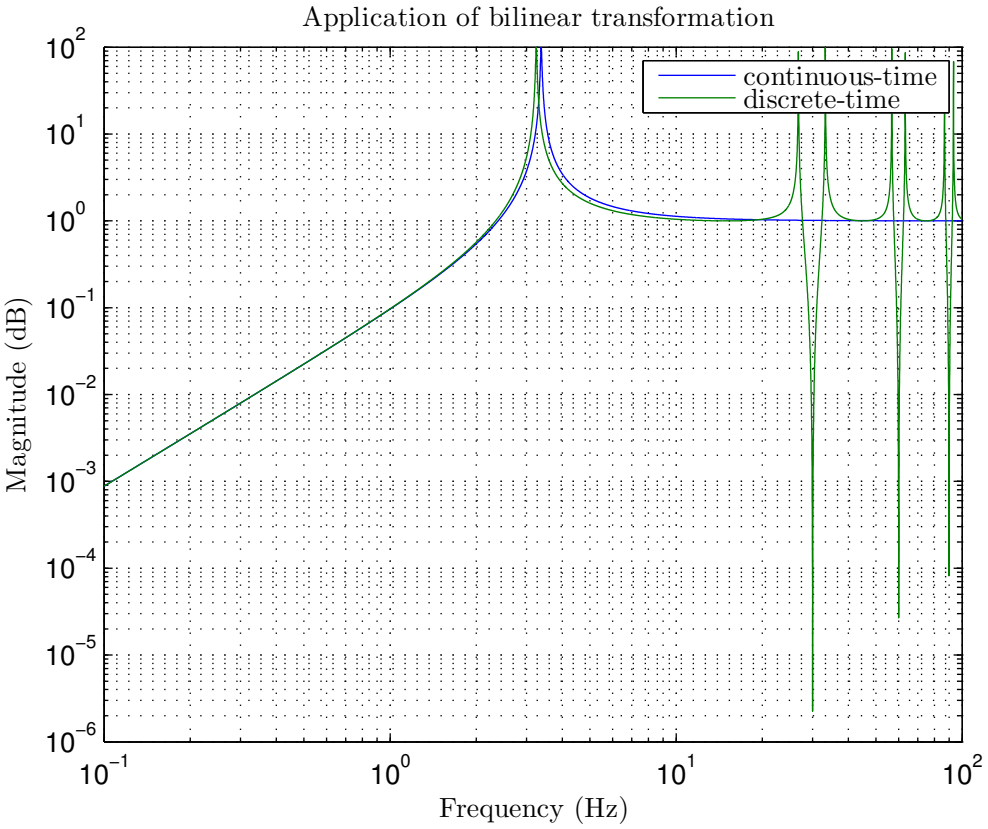


**Figure 4.1.:** Example of application of bilinear transformation to a generic continuous-time high pass filter (in blue), sampled at $f_c = 3030\,\text{Hz}$. The discrete-time system (in green) has the peak in a slightly different frequency due to the warping, and it is periodic with period $f_c$.

# 5 Seismic Isolation System in Advanced Virgo

This chapter describes the operation of the seismic isolation system in Advanced Virgo, explaining how (and how much) they are able to attenuate the seismic noise at the level of the optical elements of the interferometer.

## 5.1. Seismic Noise

The sensitivity of interferometric antennas for gravitational waves is limited at low frequency by seismic noise. This term indicates the stochastic movements of the soil, due to a multitude of causes that include nearby anthropogenic activities (such as traffic or heavy machinery), as well as natural phenomena like wind, sea waves, the position of the moon, ...

Its Power Spectral Density (PSD) at ground level is not flat, and strongly depends on environmental conditions. An empiric estimation (also known as *standard seismic noise*) is

$$S_{x_0}(f) \sim \left| 10^{-7} \left( \frac{1\,\mathrm{Hz}}{f} \right)^2 \frac{\mathrm{m}}{\sqrt{\mathrm{Hz}}} \right|^2 \tag{5.1}$$

and it corresponds to a white noise in ground acceleration. A spectrum of seismic noise measured in Virgo Central Building is presented in Fig. 5.1: it shows in more detail the features of seismic noise in condition of quiet micro-seism, and compares it with the model in 5.1.

In particular, at the Virgo site, the wind effect is visible under 0.1 Hz, the ocean between 0.1 and 0.2 Hz, the Mar Tirreno between 0.2 and 1 Hz, the traffic between 1 and 5 Hz. This noise (also called micro-seism, or $\mu$-seism) obviously fluctuates according to the environmental conditions, as shown in Fig. 5.2.

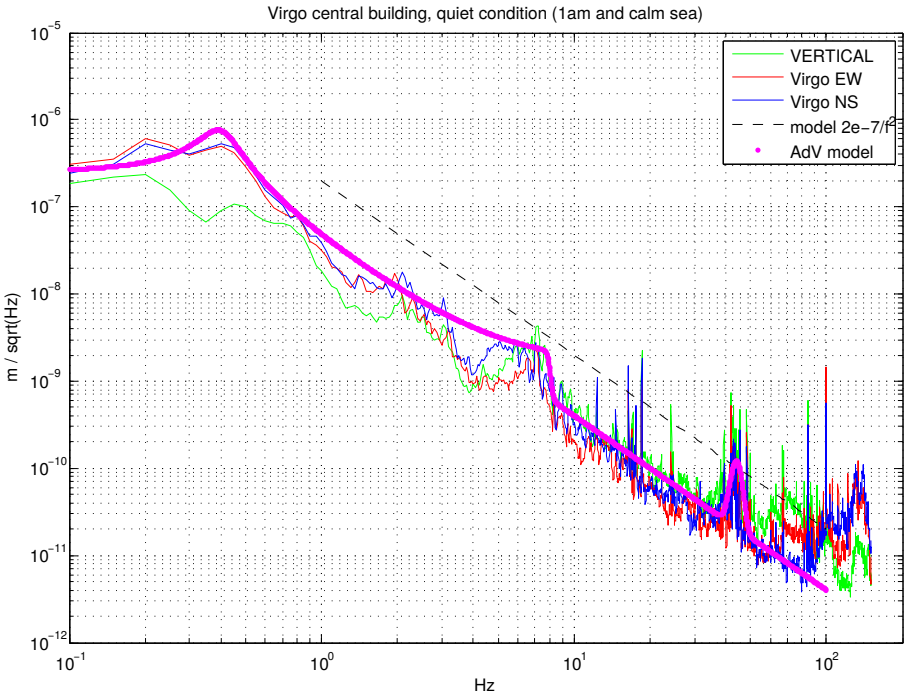


**Figure 5.1.:** Seismic noise in the Virgo Central Building, in a condition of quiet micro-seism. The green curve shows the spectral amplitude of the vertical seismic red curve the East–West horizontal vibration and the blue curve the North–South horizontal seismic vibration. The dashed black line is the model in 5.1 (actually multiplied by a factor 2). The magenta markers show a more complex model used in Advanced Virgo to reproduce the main features of the seismic noise. [25]

The seismic noise enters in the Virgo noise budget through both the residual vibration transmitted by the mechanical structures to the mirrors and the direct coupling due to the Newtonian attraction force of the suspended test masses to the soil (the so–called Newtonian or Gravity Gradient Noise).

## 5.2. Superattenuators

Therefore, if Advanced Virgo wants to measure displacement of magnitude $10^{-20}$ m, the interferometer must be strongly isolated from the seismic noise. **Superattenuators** (SA), often referred to also as *suspensions*, are complex mechanical structures implemented in Virgo to insulate optical elements from seismic noise, that make strong use of control theory.

The Virgo/Virgo+ Superattenuators have performed reliably fulfilling the require-

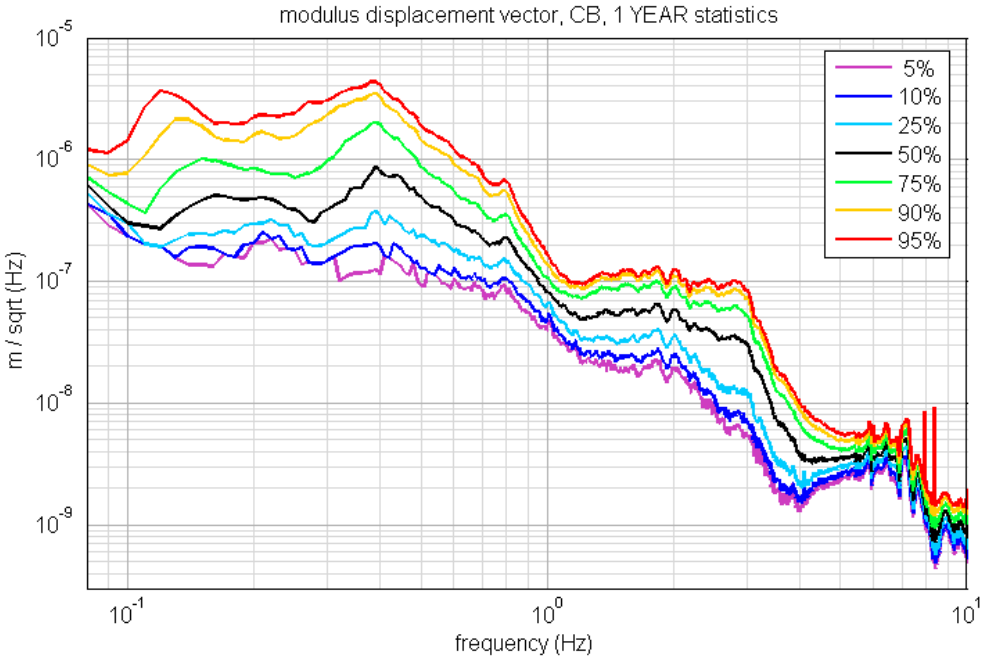


**Figure 5.2.:** Statistical property of the spectral amplitude of the micro-seismic displacement noise measured in the Virgo Central Building. For each frequency bin, it is reconstructed the probability to find a seismic amplitude below the threshold indicated by each curve. [25]

ments and, since the time of project design, their passive attenuation performance was considered to be compliant with the AdV requirements. Nevertheless, even if the essence of the suspension will be kept unchanged, some upgrades of mechanical and electronic elements are ongoing, in order to achieve better performances during periods with adverse meteorological conditions.

Advanced Virgo comprises 10 SAs all operating in Ultra-High Vacuum chambers. Seven SAs are installed in the central building while the additional three are located in north end, west end buildings (3 km far from central area) and mode cleaner building. Two classes of SAs are at present foreseen, short and long, depending on actual chain length and number of seismic filters used in the chain.

They have been designed to fulfill two main specifications:

1. reduce ground vibration transmission, in order to make mirror residual displacement below the interferometer sensitivity starting from a few hertz and thus to make seismic noise negligible above 10 Hz;

2. reduce the mirror swing displacement in the low frequency range below a few hertz, where the seismic noise is amplified by the filter chain resonances.

We are going to see how these aims are fulfilled.

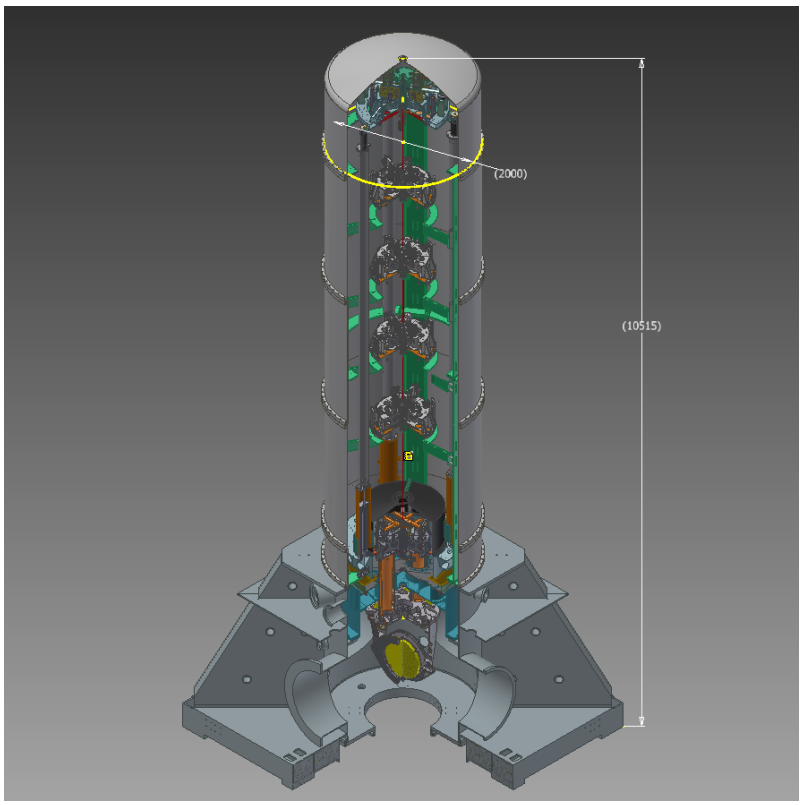


**Figure 5.3.:** The Virgo Superattenuator: the mechanical filter chain adopted to attenuate seismic vibration in the detection band, the three-leg inverted pendulum pre-isolator, the top filter of the chain (F0) and the payload are well visible. Dimensions in mm.

### 5.2.1. Passive Attenuation

The first specification is passively achieved by the SA chain of mechanical filters, that acts as a five-stage pendulum (see Fig. 5.3). Each stage behaves as a simple pendulum, and acts a second order low-pass filter; in an $n$-stage pendulum the horizontal motion of the suspension point, at a frequency $f$ much higher than the frequencies of the normal modes, is transmitted to the suspended mass with a reduction factor proportional to $f^{2n}$. This is true because the mechanical impedances are properly matched (see Appendix B).

In order to decrease the frequency detection threshold it is necessary to reduce the resonant frequencies of the chain and thus to increase the length of the pendulums. The Virgo SA chain of pendulums has an overall height of about 8 m and all its horizontal normal modes are below $\sim$ 2 Hz, providing the required attenuation starting from about 4 Hz. Vertical vibrations would be also partially transferred to the laser beam (horizontal) direction because of the unavoidable mechanical couplings between different degrees of freedom (estimated to be below one per cent)

and because of the Earth curvature that makes widely separated pendulums non parallel to each other (misalignment of $3 \times 10^{-4}$ rad for 3 km-long arms).

The top stage of the chain is formed by another mechanical filter named *Filter 0* (F0) lying over a top table suspended by thin wires from a pre-isolation tripod, usually called *Inverted Pendulum* (IP): in AdV its three legs are monolithic, made by a single aluminum tube, in order to avoid dangerous yielding in the junctions and to eliminate undesired structural modes due to the presence of intermediate links. IP modes will be at $30 - 40$ mHz, achieving a significant seismic attenuation in the horizontal direction also in the pendulum chain resonance range ($0.1 - 2$ Hz).

The 4 middle stages are called *Standard Filters* (SF). A SF is essentially a rigid steel cylinder (70 cm in diameter and 18.5 cm in height) supporting a set of maraging steel cantilevered triangular blades clamped along the outer surface of the filter body. Once properly loaded, the main vertical resonance of the blade system is around 1.5 Hz, that becomes $< 0.5$ Hz under the effects of the anti-springs, devices installed on SF to reduce the frequencies of the vertical resonances. [26]

SFs precede the last stage called, for historical reason, *Filter 7* (F7). It was designed to suspend and steer the payload, a system that is composed by the marionette and the mirror. The marionette allows the steering of the mirror with electromagnetic actuators in three degrees of freedom. In Virgo/Virgo+, F7 included the reference mass, that was designed to compensate the recoil of the mirror. However, it is removed in the new AdV payload design.

### 5.2.2. Superattenuator Control System

For the second scope, there is a digital feedback control system that takes care to suppress by a factor of about 10 the micron-wide mirror motion due to the $\sim 80$ chain resonances. It uses the information of 20 local sensors, plus 3 global sensors available when the full Virgo interferometer is locked. DSP-based boards use the information of these sensors to compute a real-time control, that eventually drives coil-magnet actuators for the feedback action. [27]

Local sensors consist of:

- three horizontal accelerometers (only in the top stage, placed at 120°)
- two vertical accelerometers (only in the top stage, over the "cross bar")
- Linear Variable Differential Transformer (LVDT) displacement sensors (almost everywhere in the structure)
- optical readout of payload displacement (in the last stage)
- dual-axes electrolytic tilt-meter (in the last stage)

The three global sensors provide the relative displacement of suspended optical elements along three main directions: the beam direction $z$ plus two angles around

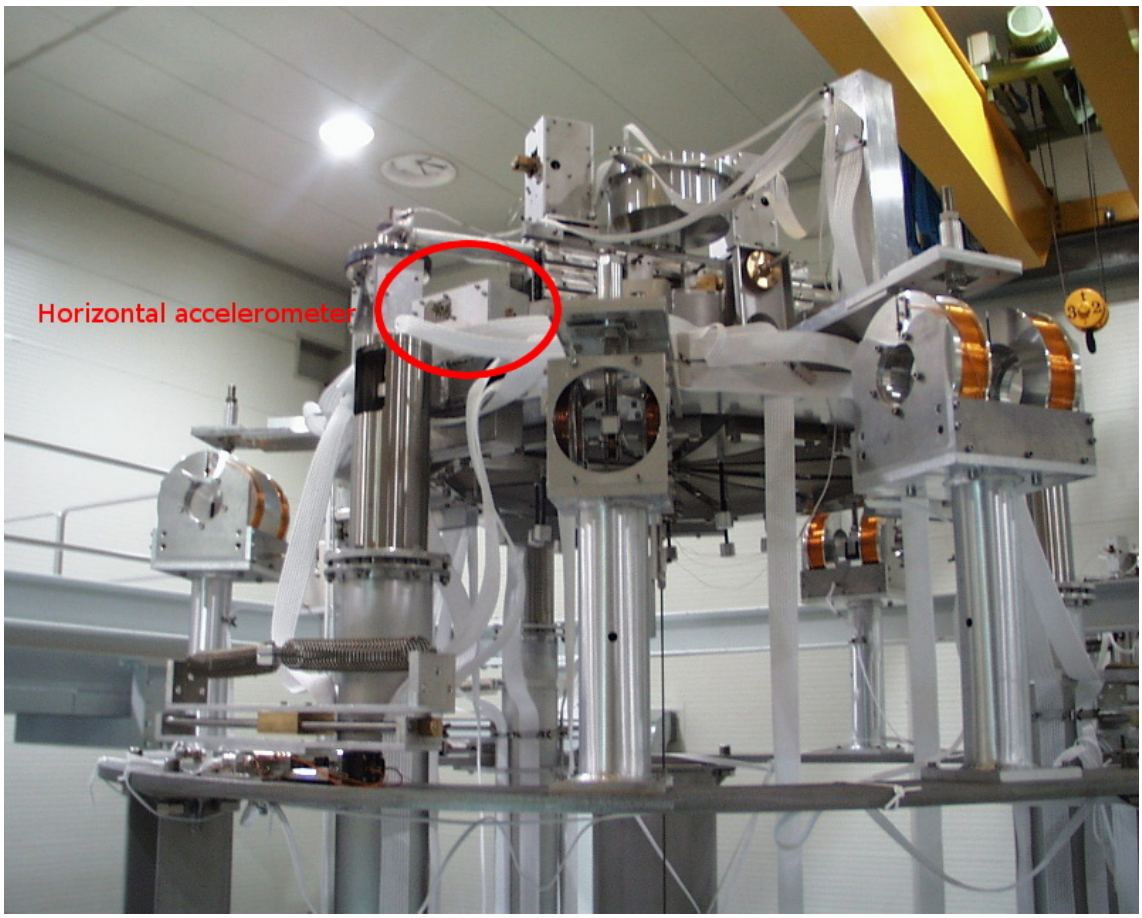


**Figure 5.4.:** Top stage of the North Input Superattenuator. One of the three horizontal accelerometer is highlighted in the red circle.

second horizontal axis $x$ and vertical axis $y$. They are defined as global because the information is provided by the Virgo global control through the status of the whole interferometer, and not of a single Superattenuator. Coil-magnet actuators are placed at the top stage and at the F7 level, on the marionette and directly on the mirror (except for the piezo actuators that are going to be placed at the base of IP).

The feedback control software is called **Inertial Damping** (ID). It runs on dedicated boards, exploiting the huge computing power of modern DSPs. Two distinct DSPs control independently the top stage and the payload.

In particular, top stage control loops are always active regardless of the status of the interferometer (i.e. not only when the interferometer is locked acquiring data). Its sensors monitor the displacement of the top stage in the DC $-$ 100 Hz bandwidth with an equivalent sensitivity of $10^{-11}\frac{\mathrm{m}}{\sqrt{\mathrm{Hz}}}$ for accelerometers, and $10^{-8}\frac{\mathrm{m}}{\sqrt{\mathrm{Hz}}}$ for LVDT displacement sensors. The digital control loop operates at 10 kHz sampling frequency, the minimum rate required in order to avoid the introduction of actuation noise in the gravitational wave detection bandwidth. Three degrees of freedom are currently

controlled (two translations in the horizontal plane and the rotation along the vertical axis), and a forth one (vertical translation) is active in some suspensions. The last Virgo+ performances allowed a residual displacement less than 1 µm at the level of suspended payload and a relative speed between long arm cavities input and end mirrors of about 0.25 µm/s, compliant with AdV requirements.

Payload control system works a little bit differently, allowing two different operational modes: when the interferometer is unlocked, payload control makes use of measurements made in respect with a local reference frame, while, when the Virgo interferometer is in locked state, payload control uses the set points distributed by global control and alignment computers. Also here there are three controllable degrees of freedom: longitudinal displacement (along the Virgo laser beam direction, $z$), rotation around the vertical axis and rotation along the horizontal axis orthogonal to laser beam direction. Only small corrections can be achieved in this stage, so that the low frequency part of the $z$ error signal is forwarded to top stage control, where bigger displacement can be achieved. The performances of the payload control system meet AdV requirements, allowing a residual angular displacement of less than 1 µrad using local sensors and less than 1 nrad using global sensors, when the interferometer is locked.

In this way, SAs reduce the seismic noise by a factor $10^{15}$ at 10 Hz, at the level of the mirrors (see Fig. 5.5 for the complete transfer function). During Virgo data acquisition runs, the control system did not limit neither sensitivity nor duty cycle, that was close to 100%. [2]

## 5.3. Control System towards Advanced Virgo

As already described in the previous sections, several changes to the mechanical structure of Virgo SA are in progress to fulfill AdV requirements. Of course, these are not the only improvements.

### 5.3.1. Gyroscope and Tilt Control

The introduction of gyroscopes has been taken into account, in order to monitor a degree of freedom poorly controlled in Virgo, that dominates the seismic noise at low frequency: the tilt. Indeed, even if ground seismic tilt was never directly measured by our site, we expect, under "good weather" conditions, a power spectrum density in the order of

$$S_{tilt}(f) \sim \left| 10^{-7} \left( \frac{1\,\mathrm{Hz}}{f} \right) \frac{\mathrm{rad}}{\sqrt{\mathrm{Hz}}} \right|^2 \tag{5.2}$$

Of course this value strongly depends on the weather conditions, and can grow a lot in the low frequency region in presence of strong wind and remote earthquakes, just

like the "ordinary" seismic noise. [28] Accelerometers on SA top stage are sensitive both to tilt and acceleration, making impossible to decouple two independent degrees of freedom that cannot be controlled in the same way. Indeed, if a traditional accelerometer subject to a gravitational acceleration $g$ is tilted an angle $\alpha$ with respect the vertical direction, it detect an acceleration

$$a = g \sin \alpha$$

Problems occur when a tilt produces a signal that is misinterpreted as a horizontal acceleration by the control loop, and loop forces the top stage to move even in absence of horizontal displacement of the ground. This is why a pure-tilt inertial sensor is mandatory to increase the duty-cycle of the interferometer, subtracting the tilt signal from the IP accelerometers and then providing the error for its control. [29]

According to some estimations, a tilt control system implemented on the SA would be the straightforward solution to reduce by at least one order of magnitude the mirror swing in $0 - 200\,\mathrm{mHz}$ range and to fulfill AdV specifications with a wide safety margin in any weather conditions.

However, even if this problems is known since the construction of the first Virgo, a suitable sensor is difficult to source mostly due to the high sensitivity required, that shall be at the level of $10^{-8} \frac{\mathrm{rad}}{\sqrt{\mathrm{Hz}}}$ in the tens of mHz band. Several kind of gyroscopes has been analyzed since the beginning of Virgo project, but none of them has been found complying gravitational wave detector requirements.

A prototype of a single axis *Hemispherical Resonator Gyroscope* (HRG) produced by Medicon (Russia) is currently under test by INFN Pisa Virgo group. HRG are the de facto standard gyroscopes used in the inertial guidance of space missions (launched aboard more than 100 spacecrafts). A recent measurement performed by Virgo Pisa group discloses that this kind of gyroscope is so far the most suitable sensor for our purpose and, even if the knowledge of this devices is still too modest to hypothesize an implementation in AdV, they are probably going to became part of the experiment in the next future.

In the meanwhile, an alternative approach is under investigation, that consist in the extrapolation of the tilt from accelerometers and LVDT displacement sensors. This because theoretically the position of a rigid body has six degrees of freedom, and can be detected by six independent sensors.

Regarding the actuators for the tilt control, piezoelectric actuators are going to be installed below the bottom flange supporting the three IP feet. It is also possible to conceive the use of these actuators to compensate the excess of vertical seismic noise on the suspension top stage, presently exciting the angular payload motion.

### 5.3.2. Electronics

In order to ensure a long term operation and maintenance for AdV, and to overcome the physical and technical obsolescence of hardware, the Superattenuator electronics

have to be upgraded: most of electronic devices together with the overall architecture was designed in mid 1990s and has been in operation for 11 to 13 years almost without any interruption. The average lifetime of the components about ten years, so that devices have become obsolete and components are often no longer available. Analog to digital and digital to analog converters, once state of the art, are today out of production since years. Therefore it is necessary to upgrade the whole control system for being ready to operate in AdV through the next ten years, as it has been done for Virgo and Virgo+.

The first DSP board, based on *Motorola DSP96002*, was put in operation in 1998. During the next few years, few minor upgrades produced 3 successive releases of the board. In 2005 the design for a completely new device, based on *Analog Devices ADSP21160*, started. First prototypes were ready by the end of 2006 and a couple of years were spent in software development. The installation was completed in 2010. Therefore a new design for a processing unit on which rely for the incoming ten years is mandatory, since the 2005 one would be too old even for initial AdV (2015). [2]

A new board has been developed, that mainly includes a powerful DSP, analog-to-digital and digital-to-analog converters, with a Field Programmable Gate Array (FPGA) that lets these devices communicate each other and with all the other boards of the experiment.

The chosen DSP is a *Texas Instruments TMS320C6678*, an eight-core fixed and floating point digital signal processor based on KeyStone Architecture, that can run at a core speed up to 1.4 GHz, executing 6 double precision floating point operations per cycle per core, corresponding to a total computing power of 8.4 GFLPOS per core for double precision floating point. It supports a large number of high speed standard interfaces including RapidIO ver. 2, PCI Express Gen2, and Gigabit Ethernet. For high throughput, low latency communication between devices, this device also sports a 50-Gbaud full-duplex interface called HyperLink. The functional diagram is depicted in Fig. 5.7. [30]

For analog-to-digital conversion, the choice fell on *Analog Devices AD7760*. AD7760 is a high performance, 24-bit $\Sigma - \Delta$ ADC that can work up to 4 MSPS. All signals generated by SA sensors are amplitude modulated, with a modulation frequency ranging from 10 kHz up to 50 kHz. The ADC will sample at high rate for then producing a decimated output. The minimum time delay that will be introduced by the ADC is 1.5 µs with an output data rate of 4 MHz. Decimation down to 10 kHz costs additional 100 µs. Noise in the 1 kHz to 100 kHz range is white and about $20\frac{\text{nV}}{\sqrt{\text{Hz}}}$, that is 2 orders of magnitude better that what it was in Virgo+ for SA accelerometers and LVDT displacement sensors. At low frequency the noise is dominated by $1/f$; if in Virgo this limited the sensitivity of the sensors, now it is going to become negligible, because ADC will acquire the signal before the demodulation: a proper band pass filter around the carrier wave will easily allow to remove $1/f$ noise.

A strong effort to select a digital-to-analog converter for AdV has been made during

the last years. The only point where SA control system can somehow affect overall experiment performances is via actuators and their driving electronics. The choice was finally set to *Analog Device AD1955*. AD1955 is a high performance 2-channel DAC for audio purposes. It includes a multibit $\Sigma - \Delta$ modulator, high performance digital interpolation filters, and continuous-time differential current output DACs. The choice of an "audio" converter was taken only after accurate testing in the sub-audio frequency range where chip behavior is not fully specified by supplier. However, we will see that the $1/f$ noise of this device worsen the sensitivity of Virgo's accelerometers at low frequencies.

The new board is also equipped with an FPGA *Altera Cyclone IV*. It takes care to the front end communication, in particular with DAC and ADC, and deal with the on-board DSP through a PCI Express link. It can execute also simple filtering on the acquired data, before to send is to the DSP.

### 5.3.3. Control Techniques

In Virgo/Virgo+ the data of displacement sensors and accelerometers in the top stage, physically placed at 120°, were mixed up with a *sensing matrix*, in order to reconstruct the displacement along three independent degrees of freedom of the system: two translational $x$ and $y$, plus one rotational $\theta$. Then a PID-based algorithm was used to compute the feedback forces in that directions, and eventually coil-magnet actuators driven with a similar mixing matrix. In control theory terminology, this "diagonalization" means breaking down a Multiple-Input and Multiple-Output (MIMO) system into many Single-Input and Single-Output (SISO) systems, that are much easier to be controlled. [31]

For Advanced Virgo, this algorithm is going to be completely redesigned, using modern techniques for multivariable feedback design and optimal control theory. An optimal control is a set of differential equations describing the paths of the control variables that minimize a cost functional. Linear-Quadratic-Gaussian (LQG) control is one of the most used techniques used in MIMO systems, and it is candidate to be used for Superattenuator control system.

Also the bandwidth of the control is going to be increased. The loop unity gain frequency in SA control system was about 5 Hz, but could be raised at least up to the first mode of the new monolithic IP legs.

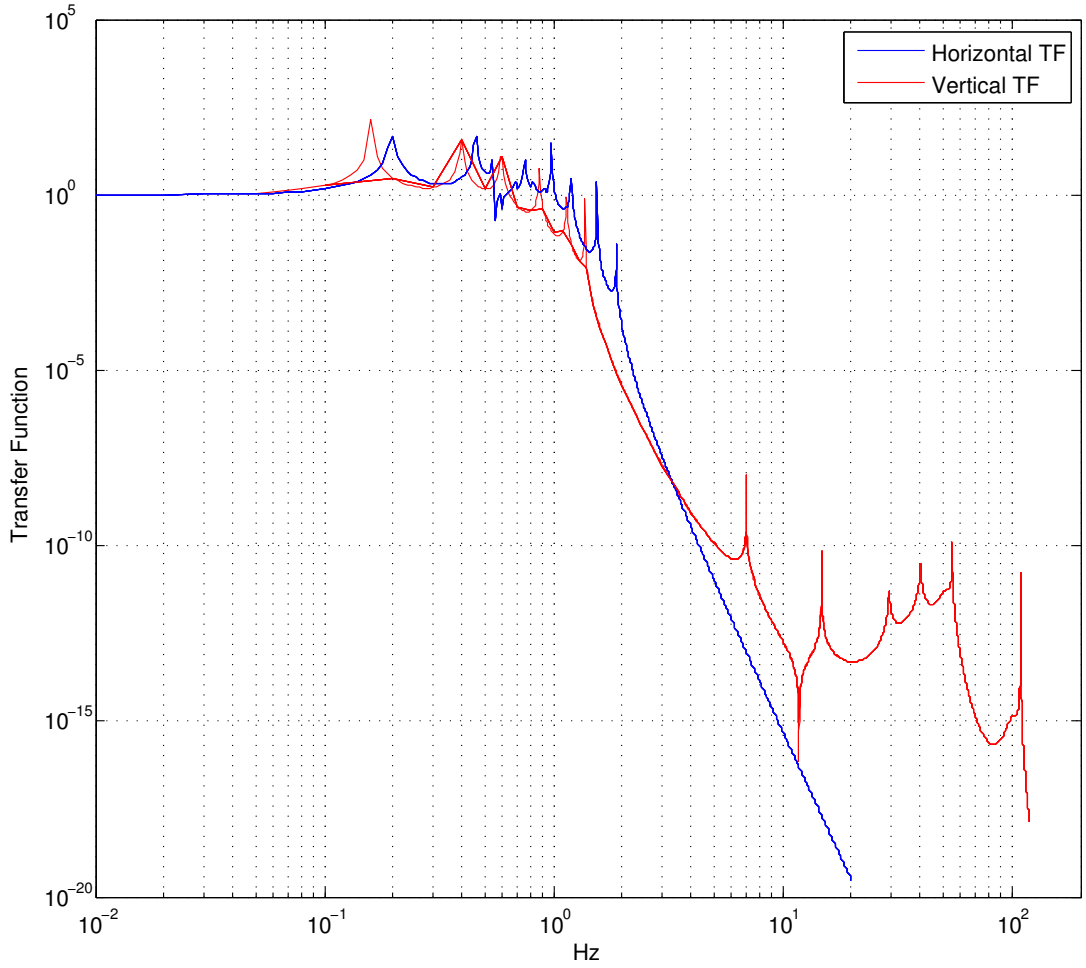


**Figure 5.5.:** Transfer Functions of the Virgo SA chain. To determine the effective filtering the role of the inverted pendulum must be inserted. Blue curve: horizontal transfer function from the F0 to the mirror. Red curve: vertical transfer function from ground to mirror. [25]

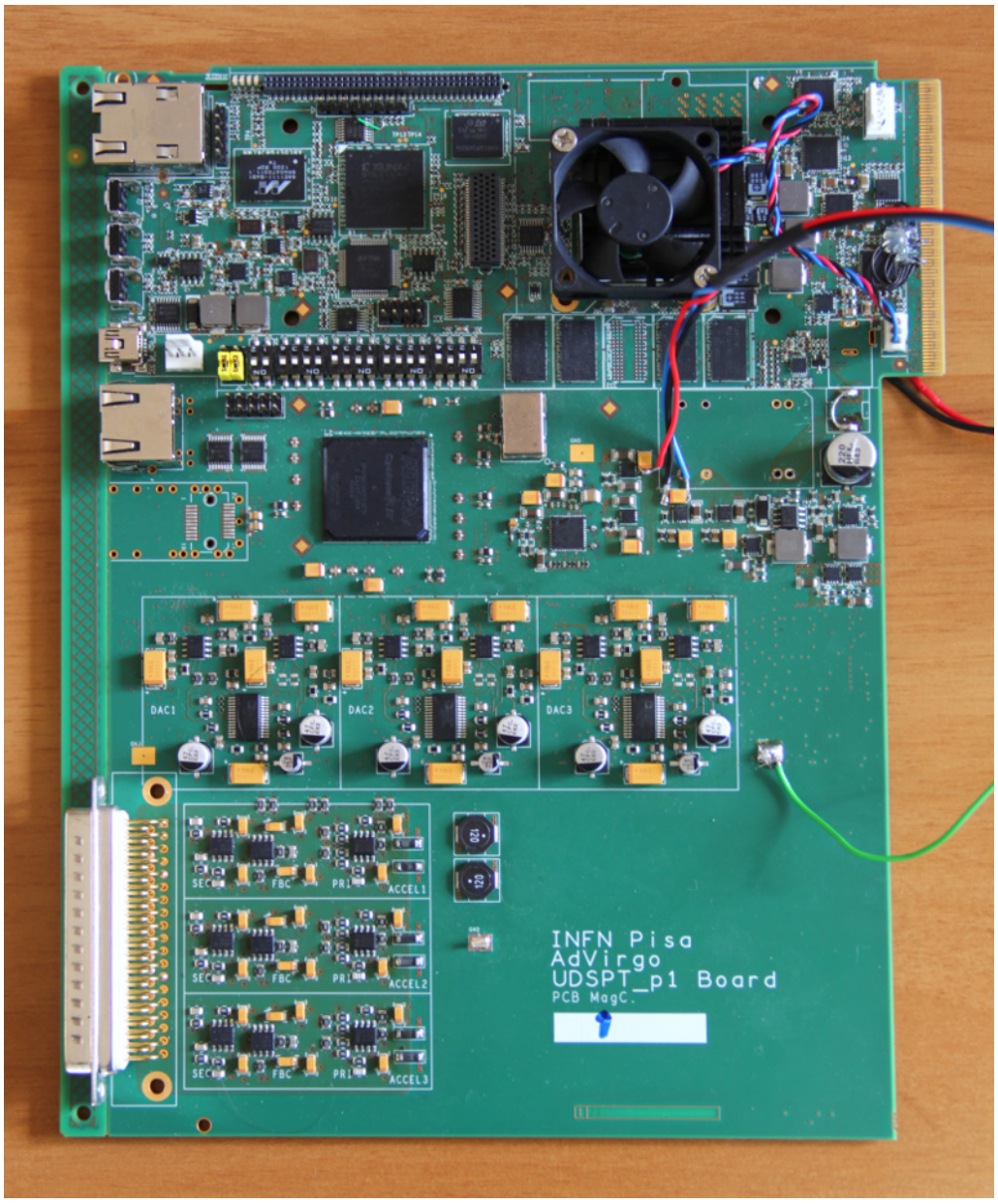


**Figure 5.6.:** Prototype of the new board. DSP is covered by the fan. FPGA is at the center of the image, while at the bottom there are 6 DAC channels and accelerometer front-end components. 6 ADC channels are on the back.

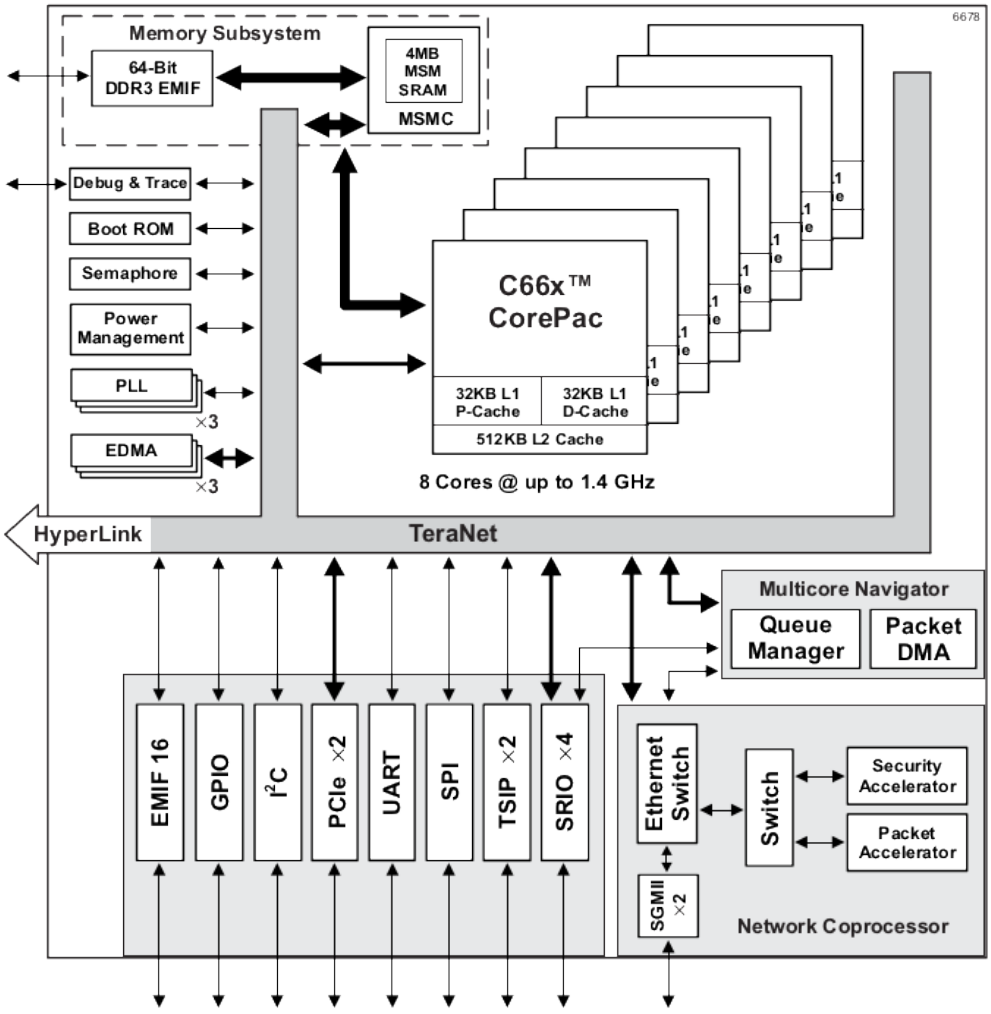


**Figure 5.7.:** Functional diagram of the TMS320C6678 device.

# 6 Accelerometer Design and Control

In this chapter is described the behavior of Virgo accelerometers, starting from a simple dynamic equation up to the description of their internal control systems, both as it was in Virgo/Virgo+ and how it will be updated in Advanced Virgo.

For the top stage, the position in the bandwidth up to a certain frequency (called *cross-frequency*) is obtained directly by displacement sensors, while, above, it is measured integrating twice the output of accelerometers.

An accelerometer is a devices that measures proper acceleration, which is the acceleration it experiences relative to free fall, and is the acceleration felt by people and objects. An accelerometer at rest, relative to the Earth's surface, will measure approximately $g = 9.8\,\mathrm{m/s^2}$ upwards, because any point on the Earth's surface is accelerating upwards, relative to the local inertial frame (the frame of a freely falling object near the surface). To obtain the acceleration due to motion with respect to the Earth, this "gravity offset" must be subtracted, introducing also corrections for the effects caused by the Earth's rotation. Due to this fact, two different accelerometers have been implemented in Virgo, to measure either horizontal or vertical acceleration. The vertical accelerometer is based on the same principle as the horizontal one, but the mechanics is different to achieve a low resonant frequency while compensating for the acceleration of gravity. In this thesis we take into account only horizontal accelerometer, whose design is shown in Fig. 6.1.

In brief, looking inside the box (see Fig. 6.2) they consist of a mass suspended by two maraging blades in order to form an inverted pendulum. A *Linear Variable Differential Transformer* (LVDT) displacement sensor measures the position of the mass with respect to the external aluminum structure. Finally, there is a coil-magnet actuator to apply an arbitrary force to the suspended mass.

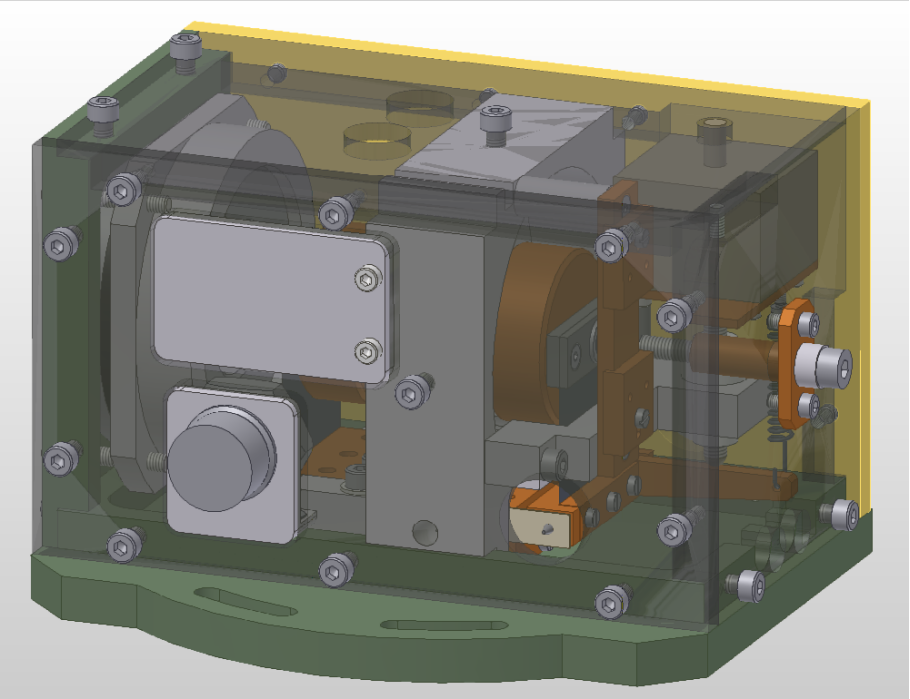

**Figure 6.1.:** AutoCAD project of Virgo horizontal accelerometer. The outer box, what is transparent in the picture, actually is made by aluminum. At the base, the horizontal longer dimension is 16.1 cm. [32]

## 6.1. A Simple Dynamics Description

In a quite simple model, the dynamics of the mass inside the accelerometer is described by a differential equation. If we call $x(t)$ the position of the pendulum and $x_0(t)$ the position of the box, with respect to an inertial frame or reference, the equation of motion of the pendulum inside the accelerometer is that of a driven damped harmonic oscillator in one dimension

$$m\ddot{x}(t) + \gamma\left(\dot{x}(t) - \dot{x}_0(t)\right) + k\left(x(t) - x_0(t)\right) = f(t) \tag{6.1}$$

where $m$ is the mass of the pendulum, $\gamma$ is the viscous damping coefficient, $k$ is the elastic constant and $f(t)$ is an external force applied to the mass. From now on I'm going to omit the dependence on the time of $x$, $x_0$ and $f$, in order to get a lighter notation:

$$m\ddot{x} + \gamma\left(\dot{x} - \dot{x}_0\right) + k\left(x - x_0\right) = f \tag{6.2}$$

This is of course a LTI system because its input/output behavior is governed by set of ordinary linear time-invariant differential equations. [23]. In Laplace transform, under the assumption that all initial conditions are zero, this reduces to

$$ms^2X + \gamma s\left(X - X_0\right) + k\left(X - X_0\right) = F \tag{6.3}$$

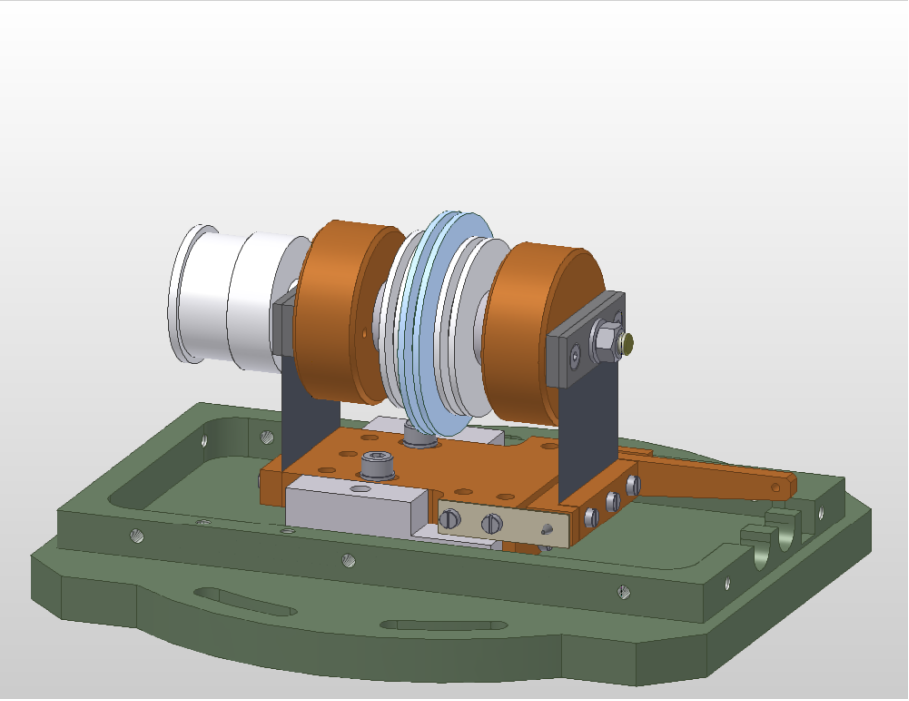

**Figure 6.2.:** Insight of the most important components of Virgo horizontal accelerometer. At the center is clearly visible inverted pendulum, with the supports for LVDT primary and two secondary coils. The primary coil is attached to the external support, while the secondary coils are fixed to the pendulum. On the left, the coil support for the feedback force. A lever, on the right, can be used to set the right working point for the system. [32]

Firstly we will study the simpler case without external forces, $F = 0$. If we define

$$\omega_0^2 = \frac{k}{m}$$

and

$$Q = \frac{m\omega_0}{\gamma}$$

the equation 6.3 can be rewritten as

$$s^2 X + \frac{\omega_0}{Q} s \left(X - X_0\right) + \omega_0^2 \left(X - X_0\right) = 0 \tag{6.4}$$

The ratio between $X$ and $X_0$ is the transfer function $X_0 \to X$:

$$\frac{X}{X_0} = \frac{\frac{\omega_0}{Q} s + \omega_0^2}{s^2 + \frac{\omega_0}{Q} s + \omega_0^2} \tag{6.5}$$

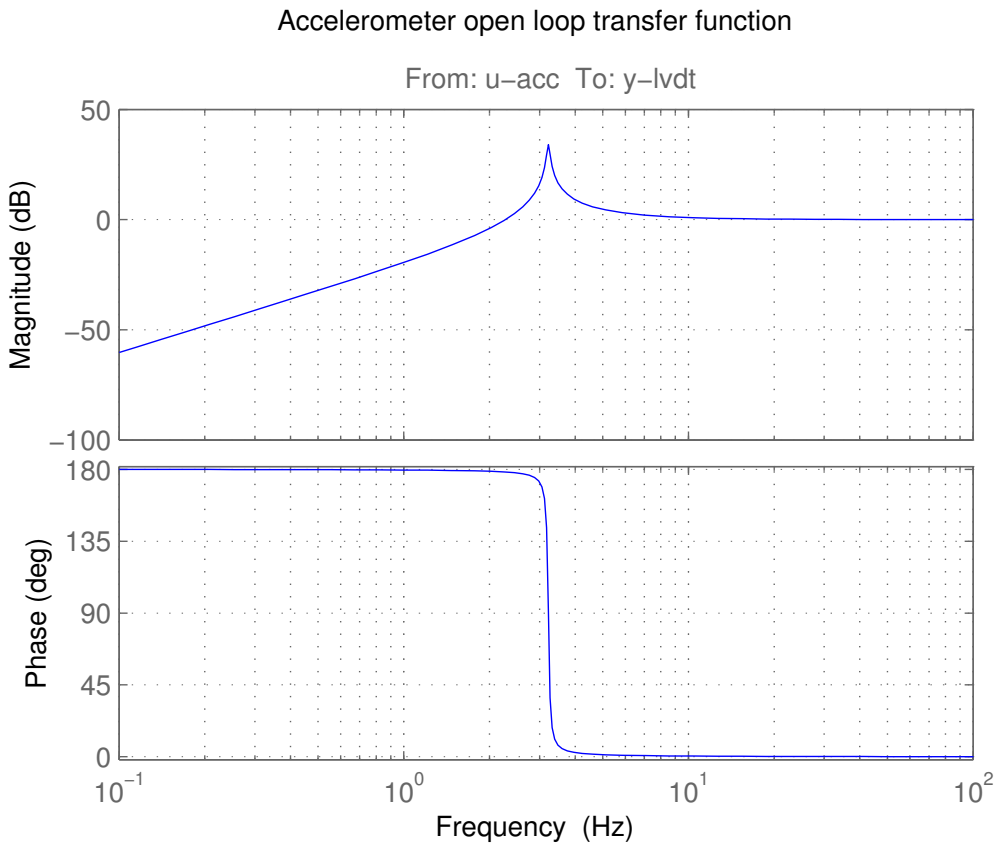


**Figure 6.3.:** Bode diagram of transfer function 6.6, with $\omega_0 = 2\pi \cdot 3.2\,\mathrm{Hz}$ and $Q = 50$.

Actually, the LVDT position sensor in the accelerometer measures the internal position $x - x_0$. So, the transfer function between $x_0$ and the position read by the LVDT is

$$\frac{X - X_0}{X_0} = \frac{\frac{\omega_0}{Q}s + \omega_0^2}{s^2 + \frac{\omega_0}{Q}s + \omega_0^2} - 1 = \frac{s^2}{s^2 + \frac{\omega_0}{Q}s + \omega_0^2} \tag{6.6}$$

To get the response in magnitude and phase to a particular angular frequency $\omega$, $s$ has to be replaced with $s = i\omega$. It's easy to see that, when $\omega \ll \omega_0$, $X - X_0$ is proportional to $s^2 X_0$, i.e. the signal $x - x_0$ is proportional to the second derivative $\ddot{x}_0$, acceleration of the sensor. The Bode plot of this transfer function is shown in Fig. 6.3.

## 6.2. Feedback Control

Up to now we have seen the dynamics of a damped oscillator when no external force acting on the system. Actually, an external force can be applied and, in this case,

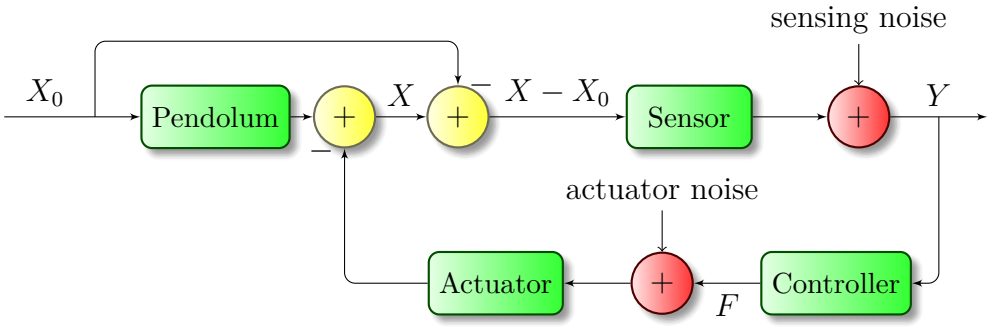


**Figure 6.4.:** Schematic diagram of Virgo accelerometer control. The actuator noise is placed before the actuator because it is essentially generated by the DAC, as we will see later.

the accelerometer becomes a system with two input and one output: the first input is the signal $x_0$, the second input is the external force $f$, while the output is of course $x - x_0$. In this case, the system can be studied applying the superposition principle. In the equation 6.5, we have already presented the response of $x$ to a stimulus in $x_0$ with $f = 0$. The other characteristic transfer function is $\frac{X}{F}$, that can be obtained from equation 6.3, imposing $x_0 = 0$ (i.e. assuming no external acceleration):

$$s^2 X + \frac{\omega_0}{Q} s X + \omega_0^2 X = \frac{F}{m} \tag{6.7}$$

This equation leads to the transfer function $F \to X$

$$\frac{X}{F} = \frac{1}{m} \frac{1}{s^2 + \frac{\omega_0}{Q} s + \omega_0^2} \tag{6.8}$$

In principle, the external force can be anything. In the particular case in which this force is function of the output of the system, we get a feedback control. In our case, being the output of the system $x - x_0$, the external force is described by a transfer function $H$

$$\frac{F}{X - X_0} = m \cdot H \tag{6.9}$$

where $m$ is the mass, so that $H$ is dimensioned as $\omega^2$.

According to the schematic diagram in Fig. 3.3, the whole system, including also the main sources of noise, is conceptually depicted in Fig. 6.4: the pendulum and actuator transfer functions strongly depend on the dynamics of the accelerometer and they can't be changed, unless we modify the instrument. On the other hand,

the user tunes the controller in order obtain the desired behavior. The process noise is omitted, as the system thermal noise of the pendulum substantially does not contribute.

The SNR is given by

$$\mathrm{SNR} = \frac{|T_{x_0}|^2 \cdot S_{x_0}}{|T_s|^2 \cdot S_s + |T_a|^2 \cdot S_a} \tag{6.10}$$

where the terms $T_i$ are the transfer functions of the input of the relative term to the output, and $S_i$ are the power spectral densities of inputs. In particular, the indices $a$ and $s$ concern respectively the actuation noise and the sensing noise, while $x_0$ represents obviously the signal.

Equation 3.7 can be applied to show that, in all $T_i$, the controller term appears only at the denominator: this definitively demonstrates that SNR cannot be improved with feedback control, whichever it may be. Actually the introduction of a controller brings along a power spectral densities $S_a \neq 0$, revealing that a feedback control could actually worsen the SNR if not properly designed.

## 6.3. Virgo/Virgo+ Design

In Virgo/Virgo+, accelerometers were designed with a bandwidth of 100 Hz, due to a lot of unmodeled resonances over this frequency. They were controlled by a dedicated PID-based analog board. A PID controller (PID stands for Proportional-Integral-Derivative controller) is conceptually represented in Fig. 6.5, and is described by this transfer function:

$$H = K_p + K_i \cdot \frac{1}{s} + K_d \cdot s \tag{6.11}$$

Actually, these three values can be interpreted in terms of time: the first term (proportional) depends on the present error $e$, the second (integral) on the accumulation of past errors, and the last one (derivative) is a prediction of future errors, based on current rate of change. The weighted sum of these three actions is used to adjust the process via a control element. The process of selecting the controller parameters $K_p$, $K_i$ and $K_d$ to meet given performance specifications is known as controller tuning.

The usefulness of PID controls lies in their general applicability to most control systems. In particular, when the mathematical model of the plant is not known and therefore analytical design methods cannot be used, PID controls prove to be most useful. [22]

The bode plot of the PID that controlled accelerometers in Virgo is depicted in Fig. 6.6, and its transfer function was:

$$\frac{F}{X - X_0} = m \cdot H = \frac{-53.8s^2 - 865.9s - 3480}{5.019 \cdot 10^{-5}s^2 + 0.39s}\,\mathrm{N/m} \tag{6.12}$$

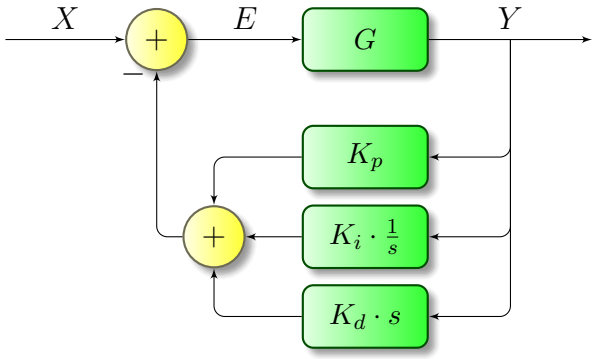


**Figure 6.5.:** Schematic diagram of a PID controller

Two zeros are placed in the proximity of the resonance, and an additional pole at 1.2 kHz; furthermore, in the controller there was a third order low pass filter to limit disturbances at frequencies higher than $\sim 1$ kHz.

The feedback force (more precisely the voltage sent to the actuator coil) was taken as output of the system (as shown in Fig. 6.7). The transfer function $\frac{F}{X-X_0}$ of the closed loop system is shown in Fig. 6.8: at frequencies $< 100$ Hz the output is proportional to $s^2 X_0$, and beyond it is highly suppressed in order to reduce effects of uncertainties.

In other words, the PID-based controller forced the pendulum to the zero-position, in a certain bandwidth: to do this, it applied a feedback force proportional to its acceleration (of course in that bandwidth). This is why the acceleration could be read as the voltage sent to the actuator coil.

## 6.4. Advanced Virgo Design

As seen before, a feedback worsens SNR: so, why don't we free the pendulum, using the accelerometer without any controller? There are at least two reasons that make a feedback free configuration to be risky. Firstly, there are tens of accelerometers in Virgo, and, even if the they are build in the same way, some parameters could change (masses, Q-values, $\omega_0$, ...). Secondarily, the LVDT that measures $x - x_0$ has a linear range of at most 0.5 mm around the central position, and we must be sure that the pendulum does not leave this region. Beyond, their contribution becomes greater than 1 %, and induces spurious effects during the demodulation. Actually, we must keep this range even narrower because of the noise on primary coil.

In these conditions, the high $Q$ resonance peak at $\omega_0$ would dominate the behavior of the system, making it difficult for us to extract the acceleration from the LVDT signal: indeed, the transfer function 6.6 says that the signal $x - x_0$ is proportional to $\ddot{x}_0$ only for $\omega \ll \omega_0$. Thus, we need to apply a digital shaping filter to it in order

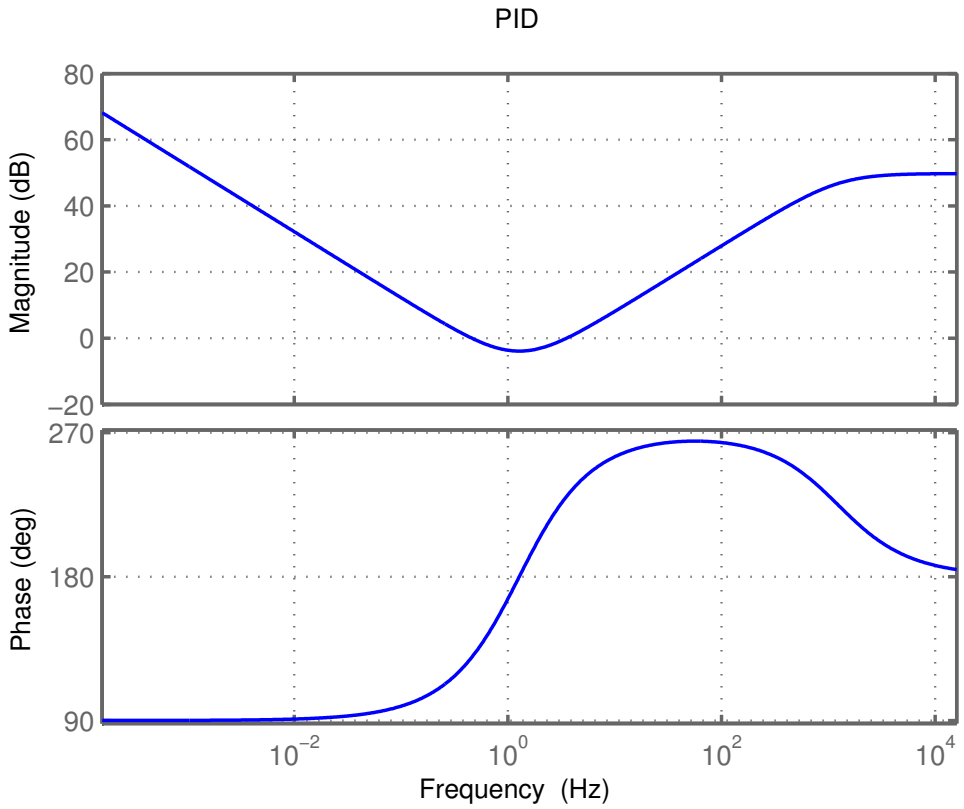


**Figure 6.6.:** Bode plot of PID in Virgo accelerometer control

to extend the bandwidth where the signal is proportional to acceleration, at least up to 100 Hz (this is the bandwidth of Superattenuator inertial control). An inadequate knowledge of the $Q$-value could make this a tough job. Actually, the $Q$-values of Virgo accelerometers are pretty high ($\sim 10^2$) but, depending on several parameters (temperature, materials, ...), they can be not only very different each other, but can also vary during the time.

So, being this the main problem of the free configuration, we can design a very simple controller, that reduces the effects of an high $Q$-value: this will be thoroughly analyzed in the next section.

Today the control engineering offers also several tools to design more sophisticated feedback system, like $LQG$ and $H_\infty$ optimal control theories. Nevertheless, these techniques are especially suited for multivariable feedback systems, i.e. the suspensions, where it is not easy to handle all the resonances and the uncertainties of the model. When applied to a SISO system, like the accelerometer, they do not provide remarkable improvements that could justify a mathematically harder approach to the problem.

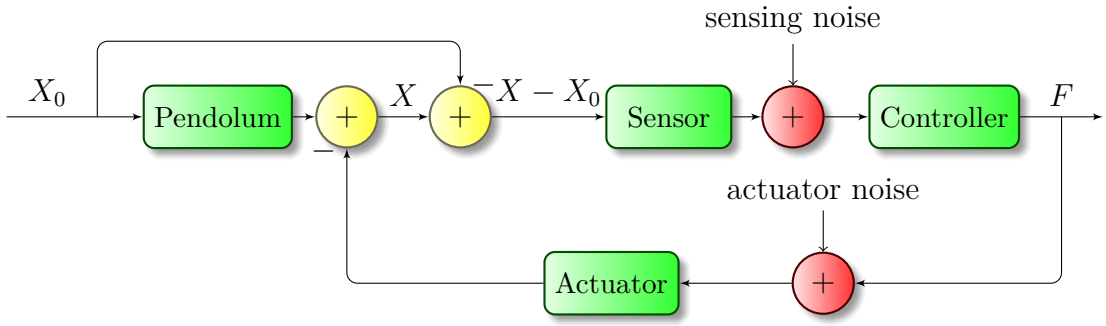


**Figure 6.7.:** Schematic diagram of Virgo accelerometer analog control

### 6.4.1. Critical Damping

A suitable feedback force permits to get a control on the $Q$-value. Indeed, designing a feedback that produces a force proportional to the pendulum velocity $\dot{x} - \dot{x}_0$, or $s\,(X - X_0)$ in the frequency domain, we can change the transfer functions of our systems to get a well defined $Q$-value. This means to apply an external force $F$ with a transfer function $H$ in equation 6.9 with first order in $s$:

$$\begin{aligned} H &= -\frac{\Gamma}{m}s \\ F &= -\Gamma s\,(X - X_0) \\ f &= -\Gamma\,(\dot{x} - \dot{x}_0) \end{aligned} \tag{6.13}$$

where $\Gamma$ is a constant with the dimension of a viscous damping coefficient. With this choice we can write, using equation 6.3,

$$\begin{aligned} ms^2X + \gamma s\,(X - X_0) + k\,(X - X_0) &= -\Gamma s\,(X - X_0) \\ ms^2X + (\gamma + \Gamma)\,s\,(X - X_0) + k\,(X - X_0) &= 0 \end{aligned}$$

that corresponds, just like equation 6.6, to a closed loop transfer function $X_0 \to X - X_0$

$$\frac{X - X_0}{X_0} = \frac{s^2}{s^2 + \left(\frac{1}{Q_F} + \frac{1}{Q}\right)\omega_0 s + \omega_0^2} \tag{6.14}$$

where we have defined $Q_F = \frac{m\omega_0}{\Gamma}$. It should be easy to see that the closed loop system correspond to a new damped harmonic oscillator with a $Q$-value given by

$$\frac{1}{Q_{CL}} = \frac{1}{Q_F} + \frac{1}{Q} \tag{6.15}$$

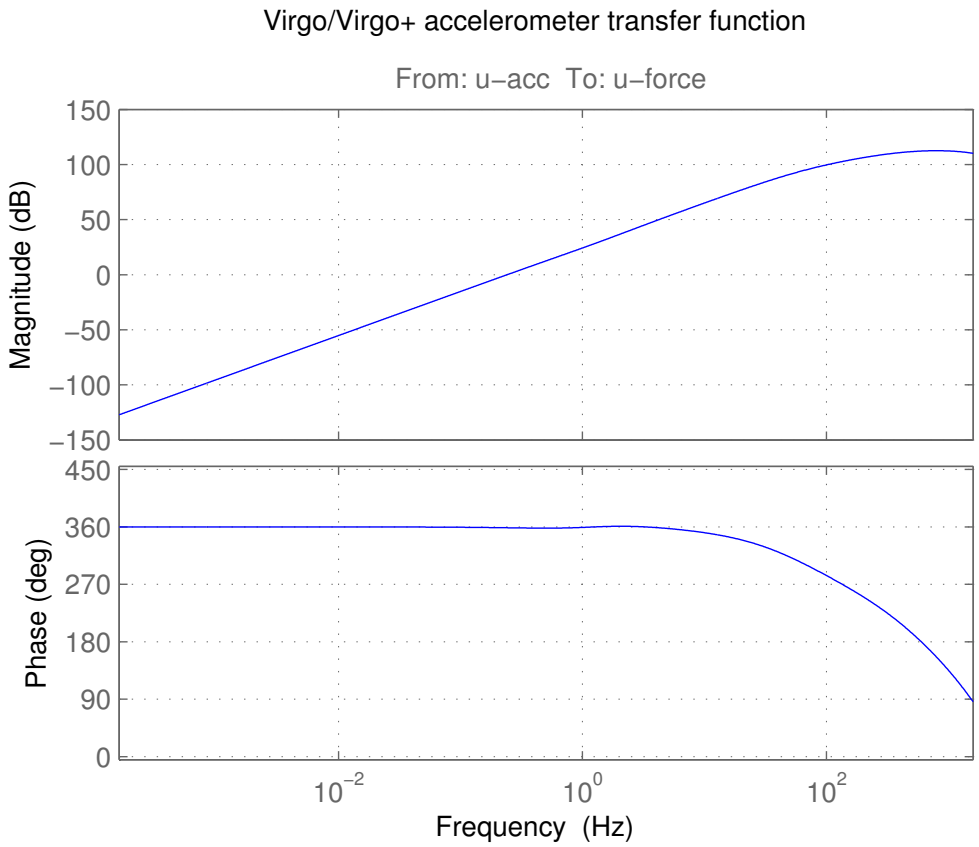


**Figure 6.8.:** Bode plot of input/output ratio $\frac{F}{X-X_0}$ in the Virgo/Virgo+ accelerometer, regulated by its analog controller. Units are N/m.

Typical $Q$-values of Virgo accelerometers operating in vacuum are usually $\sim 150$, but they change during the time and also from a device to the other. If we use a relatively low $Q_F$, such that $Q_F \ll Q$, the effective quality factor loses its dependence on the original, largely unknown $Q$:

$$Q_{CL} = Q_F \tag{6.16}$$

The value of $Q$ in equation 6.4 critically determines the behavior of the system. We can distinguish four kind of oscillators:

1. ($Q < 0.5$) *overdamped*: the system returns exponentially to steady state without oscillating. Smaller values of $Q$ return to equilibrium slower.
2. ($Q = 0.5$) *critically damped*: the system returns to steady state as quickly as possible without oscillating.
3. ($Q > 0.5$) *underdamped*: the system oscillates with the amplitude exponentially decreasing to zero. The angular frequency of the underdamped harmonic oscillator is given by $\omega_1^2 = \omega_0^2 \left(1 - (2Q)^{-2}\right)$.

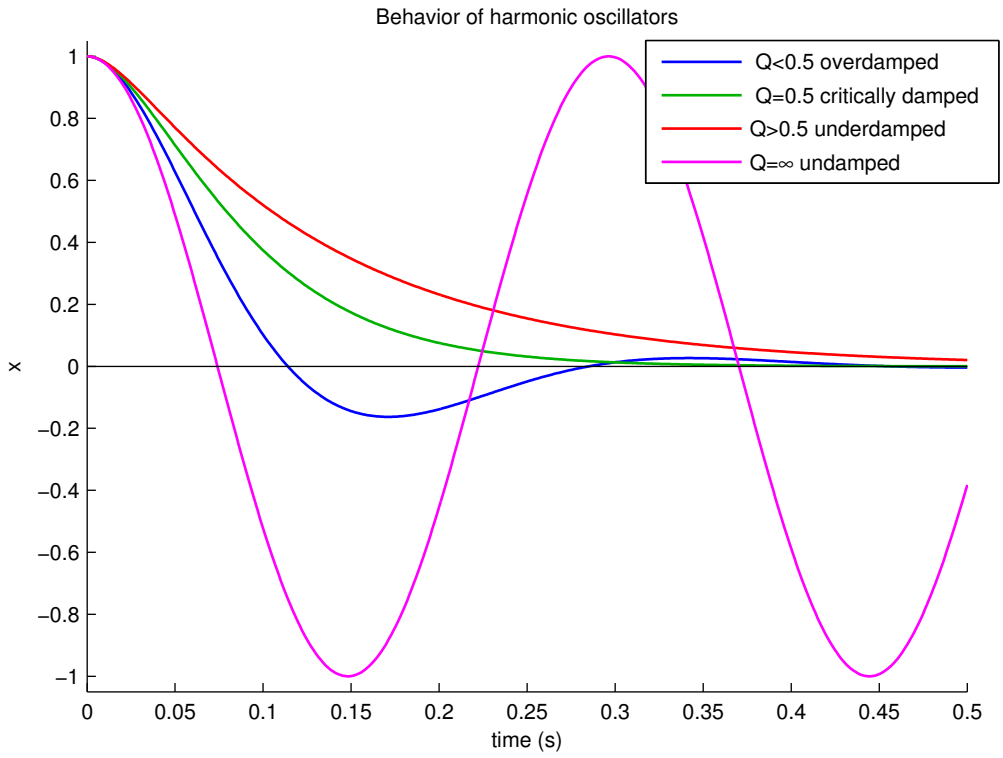


**Figure 6.9.:** Behavior of an harmonic oscillator with $\omega_0 = 2\pi \cdot 3.375\,\mathrm{Hz}$ and initial conditions $[x_0, \dot{x}_0] = [1, 0]$, as function of different $Q$-values.

4. $(Q = \infty)$ *undamped*: the system oscillates forever.

In engineering design, it is often desirable to get a critical damping: as can be seen in Fig. 6.9, this condition allows the fastest stabilization of the system to steady state. In Virgo accelerometer this can be achieved applying a feedback force like 6.14 with a $\Gamma$ such that $Q_F = 0.5$:

$$\Gamma = \frac{m\omega_0}{Q_F} \approx 17 \frac{\mathrm{N}}{\mathrm{m/s}}$$

Being $Q_F \ll Q$, from 6.16 the system transfer function becomes

$$\frac{X - X_0}{X_0} = \frac{s^2}{s^2 + 2\omega_0 s + \omega_0^2} \tag{6.17}$$

and the Bode diagram is shown in Fig. 6.10, compared with the system without feedback.

In conclusion, we can design the accelerometer control using a feedback force 6.13 and taking $X - X_0$ as output: it is proportional to acceleration $s^2 X_0$ for $\omega < \omega_0$, that is $\sim 3\,\mathrm{Hz}$. The extension of the bandwidth where displacement is proportional

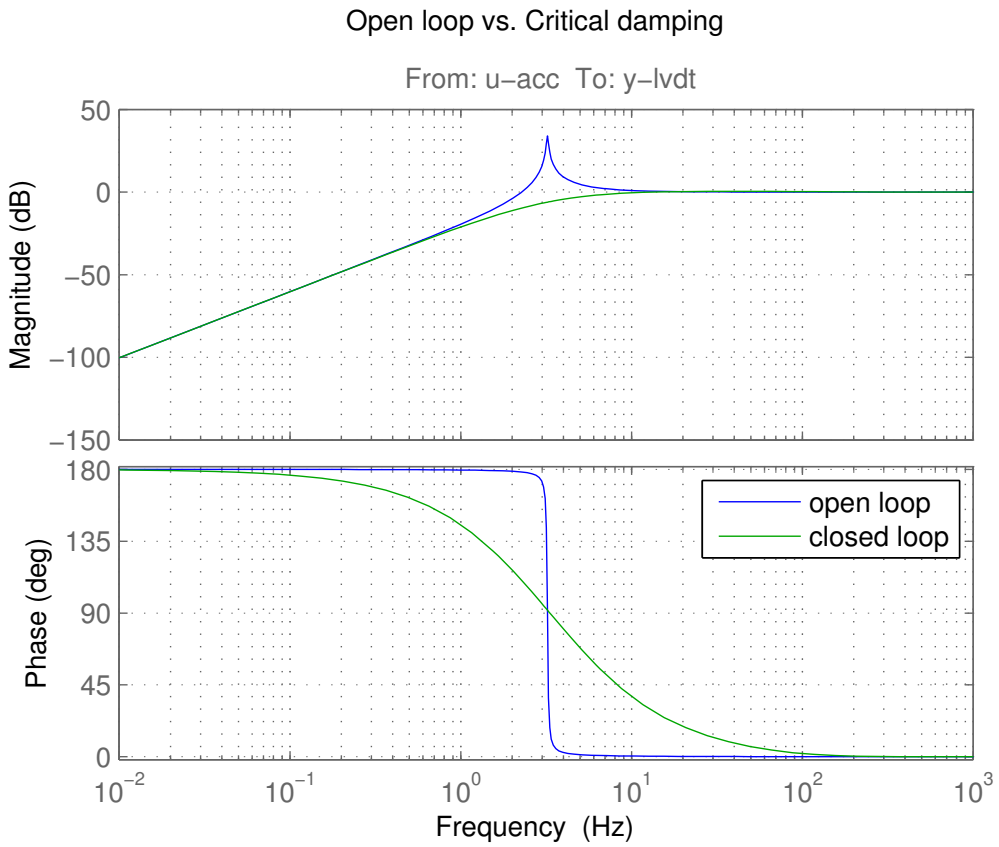


**Figure 6.10.:** Comparison between the transfer functions $\frac{X-X_0}{X_0}$ of the open loop system (equation 6.6, the same as in Fig. 6.3), and of the same system in critically damped closed loop configuration (equation 6.14).

to the acceleration can be easily achieved, applying, on the acquired data, a proper digital filter to reshape the transfer function as we need. Looking at equation 6.17, if we multiply that function transfer by a filter identical to its denominator

$$T_{shaping}(s) = s^2 + 2\omega_0 s + \omega_0^2 \tag{6.18}$$

(i.e. a second order high pass filter with a double zero in $\omega_0$) we get a system whose output is proportional to the acceleration in the whole bandwidth

$$\frac{X - X_0}{X_0} = s^2 \tag{6.19}$$

Of course, we should add to 6.18 at least 2 poles at $\sim 100\,\mathrm{Hz}$ both to get a stable system and to limit the higher frequencies disturbances, that are completely useless for the Superattenuator control system. Indeed, we will see in chapter 9 as, at high frequencies, the thermal noise on LVDT produces an equivalent noise in acceleration proportional to $\omega^2$, exceeding the seismic noise signal at 100 Hz.

Of course, this shaping filter is going to be implemented in the DSP, inside Inertial Damping: the equivalent digital filter $T_{shaping}(z)$ is obtained using bilinear transformation and pre-warping.

We cannot apply the same procedure with reshaping filters directly with the open loop transfer function 6.6, because the transfer functions of the reshaping filters would be tediously tuned accelerometer by accelerometer, as they depends on the exact $Q$-values of the single accelerometers.

Some measured transfer functions are presented in the next chapter, where we show the implementation of this system in a real Virgo accelerometer.

# Part III.

# Implementation of the Digital Control

# 7 Measurement of Transfer Functions

Our group has available a spectrum analyzer *Bruel & Kjaer LAN-XI Type 3160*. It has 4 inputs and 2 outputs, and can be used through the software *PULSE LabShop* to acquire signals in both time domain and frequency domain, to measure transfer functions, coherence and also to generate arbitrary signal, in the frequency range DC to 51.2 kHz. Its noise depends on the peak voltage and in the input range. With input range 10 V peak-to-peak, it is either $< 19\frac{\text{nV}}{\sqrt{\text{Hz}}}$ or $< 313\frac{\text{nV}}{\sqrt{\text{Hz}}}$ depending on the peak voltage $\lessgtr 316\,\text{mV}$. [33]

The characteristic transfer function of the accelerometer is of course $\frac{X-X_0}{X_0}$. However, it's hard to generate white noise in displacement $X_0$. Virgo SAT group has available a structure that can perform controlled movement, but the bandwidth is limited to $\sim 1\,\text{Hz}$, smaller than the expected peak at $\omega_0$.

On the other hand, the simplest transfer function to measure on the accelerometer is $\frac{X}{F}$, already presented in equation 6.8. DSP has been used to generate band limited pseudo-random white noise to be sent to the actuator coil (from 0 to 50 Hz, one line every 7.8125 mHz, with 200 mV RMS through the actuator coil), and then to read the output of LVDT demodulated by Virgo analog board.

Actually, DSP was driving actuator with critical damping control summed to that pseudo-random noise. Indeed, $\frac{X}{F}$ depends only on mechanical properties of the system. This allowed a more precise measurement, because the pendulum was not free to move at its resonance.

## 7.1. Calibration

For the measurements presented in this chapter, the Virgo/Virgo+ accelerometer analog board has been used to demodulate the signal of LVDT and to drive actuator coil, because at that time the new board was not yet ready for the final use.

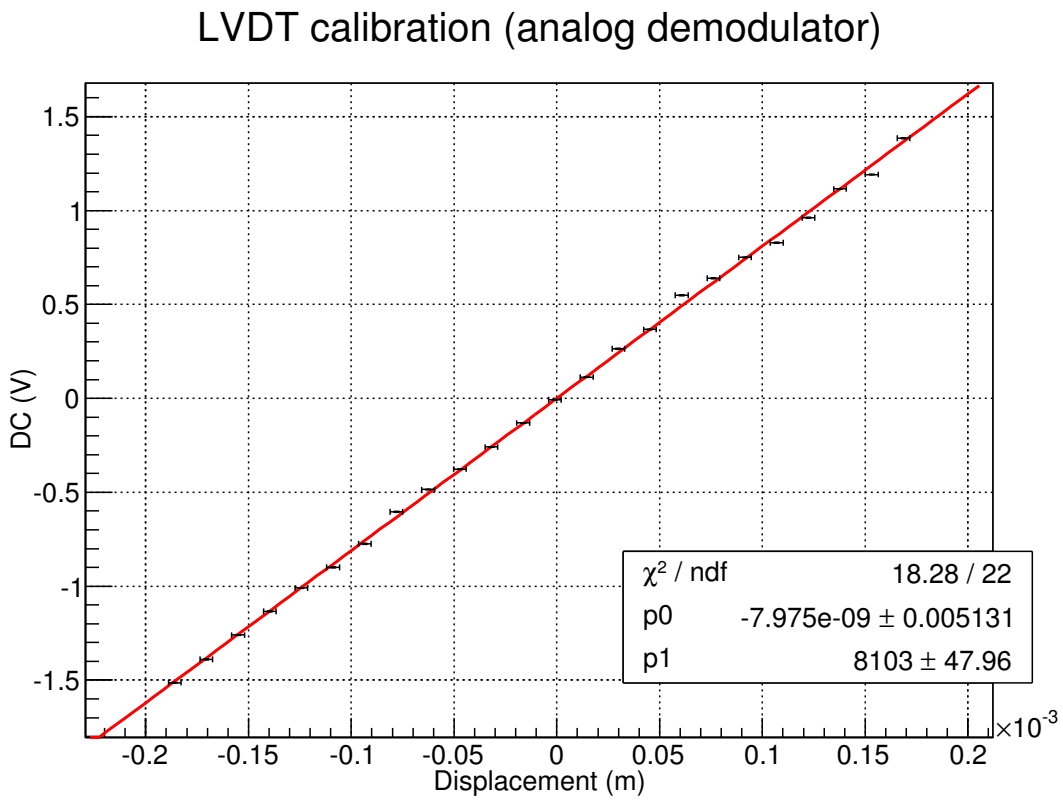


**Figure 7.1.:** Calibration curve of LVDT output around the electrical center, acquired in a open-loop configuration

The output of demodulation is related to the displacement: before to proceed with the measurement of transfer functions, it's useful to analyze and quantify the relation between voltage at the output of demodulator and displacement. The sensitivity at transformer level mostly depends on the geometry of the system and on the current flowing on the primary coil. Then, before the analog-to-digital conversion, the signal is amplified and then demodulated by Balanced Modulator/Demodulator AD630.

As shown in Fig. 7.1, the proportionality from voltage to displacement is direct (at least near the electrical center, i.e. where the output is null) and it has been found to be

$$\xi = 8103 \pm 48\,\mathrm{V/m} \tag{7.1}$$

Second and third order effects cannot be evaluated in this range, but their contribute should be $\sim 1.2\%$ at 0.5 mm from the center. [34] For this measurement, we have tilted the accelerometer inserting gradually some paper sheets under one side of the accelerometer. From the sizes of the accelerometer (161 mm) and the thickness of one sheet (0.100 mm) we get the tilt $\alpha$, that make the mass inside the accelerometer move to the new equilibrium point, where $mg \sin\alpha = -kx$. The dominant uncertainty

is related to the low precision in the manual placement of the sheets under the accelerometer.

In the matter of the actuator, the conversion between voltage and applied force is found to be $\epsilon = 30\,\mathrm{mN/V}$. This value comes from the equation 9.5 explained in chapter 9 about noise budget. In the analog board actuator coil was closed on a resistor $R_D = 1\,\mathrm{k\Omega}$.

## 7.2. Open Loop Transfer Function

The transfer function measured in open loop configuration is shown in Fig. 7.2 (even if for this particular measurement noise was actually generated by *Bruel & Kjaer LAN-XI Type 3160*, as written in the caption). The overall behavior in magnitude and phase matches the expectations, scaling as $\omega^{-2}$ without any remarkable resonance at least up to 100 Hz: effectively the resonance at 5 Hz is not internal to the sensor, being generated by the table used as support for the accelerometer during the measurements. Finally, as we have already disclosed, a great number of resonances appears. However, the roughness in this zone is pretty high also due to the statistical fluctuation for extremely low signals. Since we are going to use the accelerometer only for frequencies below 100 Hz, these resonances can be ignored.

So we have measured the transfer function of accelerometer restricted in this bandwidth (DC to 50 Hz), to get a better estimation of the parameters. It is shown in Fig. 7.3. It has been fitted with a 2 poles model

$$\frac{A}{s^2 + Bs + C} \tag{7.2}$$

using MATLAB function `tfest`. The result of the fit is:

$$A = -541.18 \pm 0.63 \tag{7.3}$$
$$B = 0.4211 \pm 0.0048 \tag{7.4}$$
$$C = 437.823 \pm 0.099 \tag{7.5}$$

with covariance matrix relative to $(A, B, C)$

$$\Sigma = \begin{pmatrix} 0.3912 & -3.1999 \times 10^{-4} & -0.0107 \\ -3.1999 \times 10^{-4} & 2.2970 \times 10^{-5} & 8.7490 \times 10^{-6} \\ -0.0107 & 8.7490 \times 10^{-6} & 0.0099 \end{pmatrix} \tag{7.6}$$

These values are related to physical quantities in this way:

$$\omega_0 = \sqrt{C} \tag{7.7}$$
$$Q = \frac{\sqrt{C}}{B} \tag{7.8}$$
$$\alpha \left(m\omega_0^2\right)^{-1} = \frac{A}{C} \tag{7.9}$$

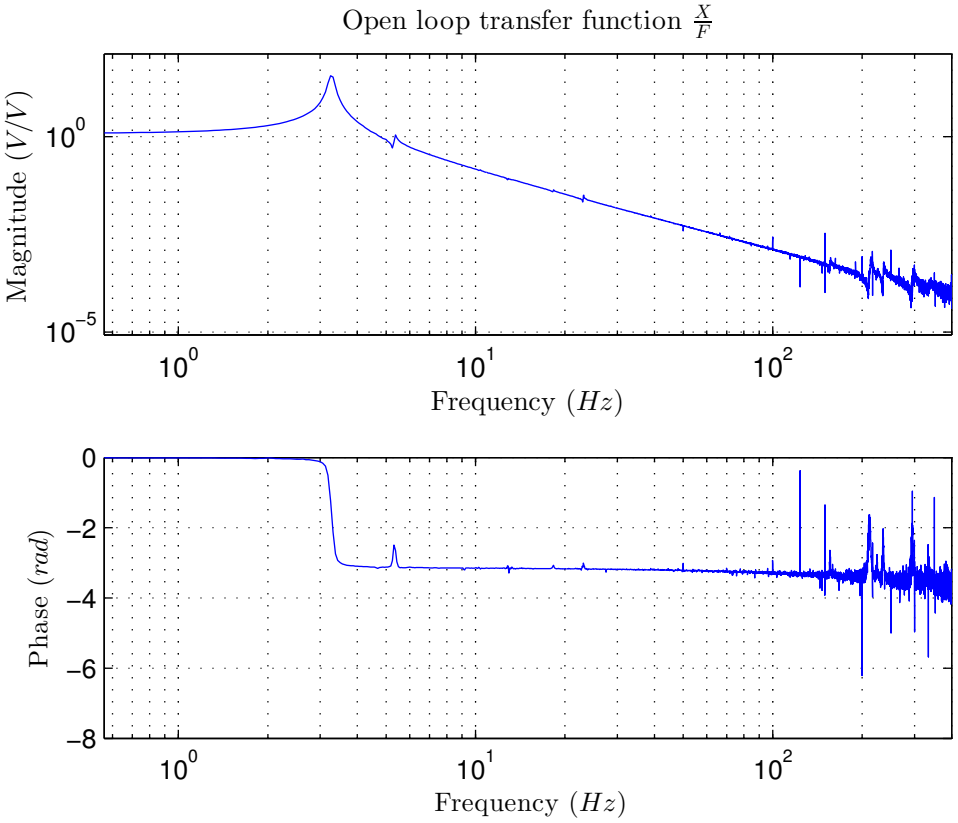


**Figure 7.2.:** Direct measurement of $\frac{X}{F}$ open loop transfer function up to 400 Hz, expressed as ratio of voltages sent to the coil and read after the demodulator, and averaged 5000 times. Actuator was driven by 25 mV RMS of band limited white noise DC-400 Hz generated by *Bruel & Kjaer*. How is going to be shown later, the resonance at 5 Hz it's not internal to the sensor, being generated by the board used as support for the accelerometer during the measurement.

where the last term is the DC value and $\alpha = \xi\epsilon$ is product of the sensitivities on sensing and actuating systems. Propagating uncertainties, we find

$$\frac{\omega_0}{2\pi} = 3.33019 \pm 0.000\,38\,\text{Hz} \tag{7.10}$$

$$Q = 49.69 \pm 0.56 \tag{7.11}$$

The $Q$-value is relatively low, due to the absence of vacuum in our laboratory. Measured DC value is $1.23607 \pm 0.000\,43$ V/V. However, this value is not so interesting, because strongly depends on the electronic, that will be replaced in AdV. The `tfest` fit to estimation is 93.69% (simulation focus).

In conclusion, the model used so far in the text agrees outstandingly with the measurements.

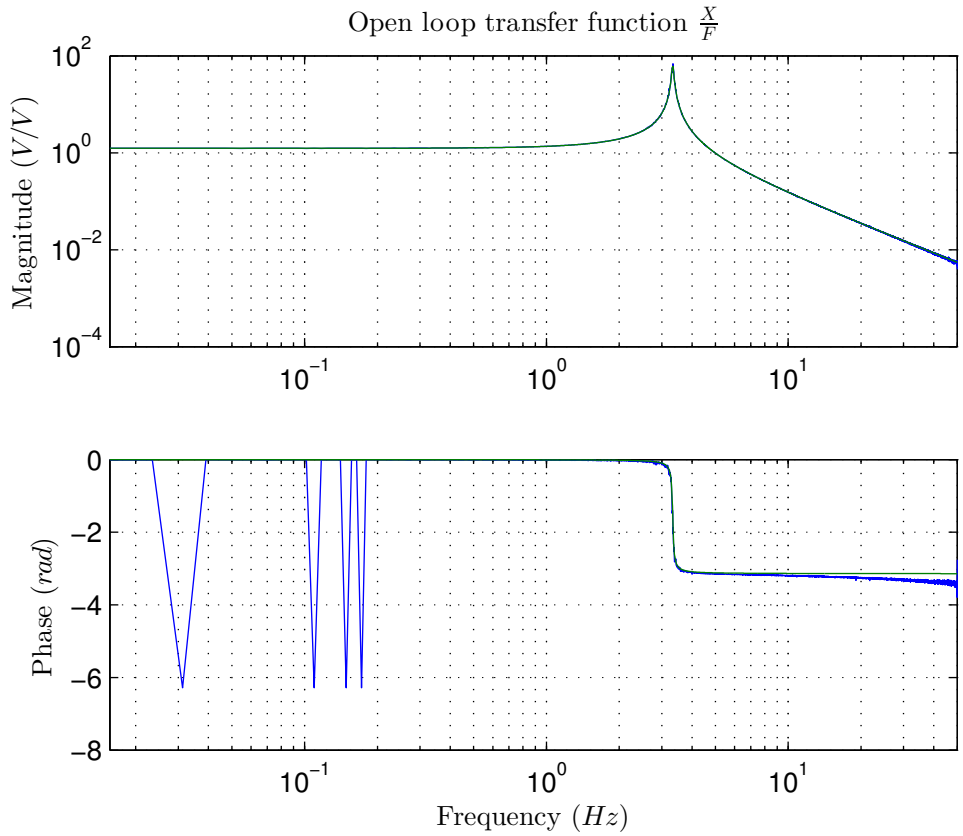


**Figure 7.3.:** Direct measurement of $\frac{X}{F}$ open loop transfer function at low frequency (blue line) and the simple pendulum model (green line). It is expressed as ratio of voltages sent to the coil and read after the demodulator. This time actuator has been driven by a pseudo-random white noise generated by DSP, sending only those lines that would have been acquired by *Bruel & Kjaer*.

### 7.2.1. LVDT Non-Linearity Effects

An effect arisen during measurements has been the presence of spurious signals, due to non-linearity of LVDT: after the demodulation, this generates alias signals at frequencies integer multiple of the original ones. In the open loop configuration, when pendulum is moving mostly at $\omega_0$, this effect is visible at $2\omega_0$, $3\omega_0$, etc. for displacement $> 100\,\mu m$.

This is not a real problem because, as we will see later, we may restrict strongly the movement of the pendulum to prevent also another source of noise: that of signal in primary coil, that becomes dominant for displacement $> 7\,\mu m$.

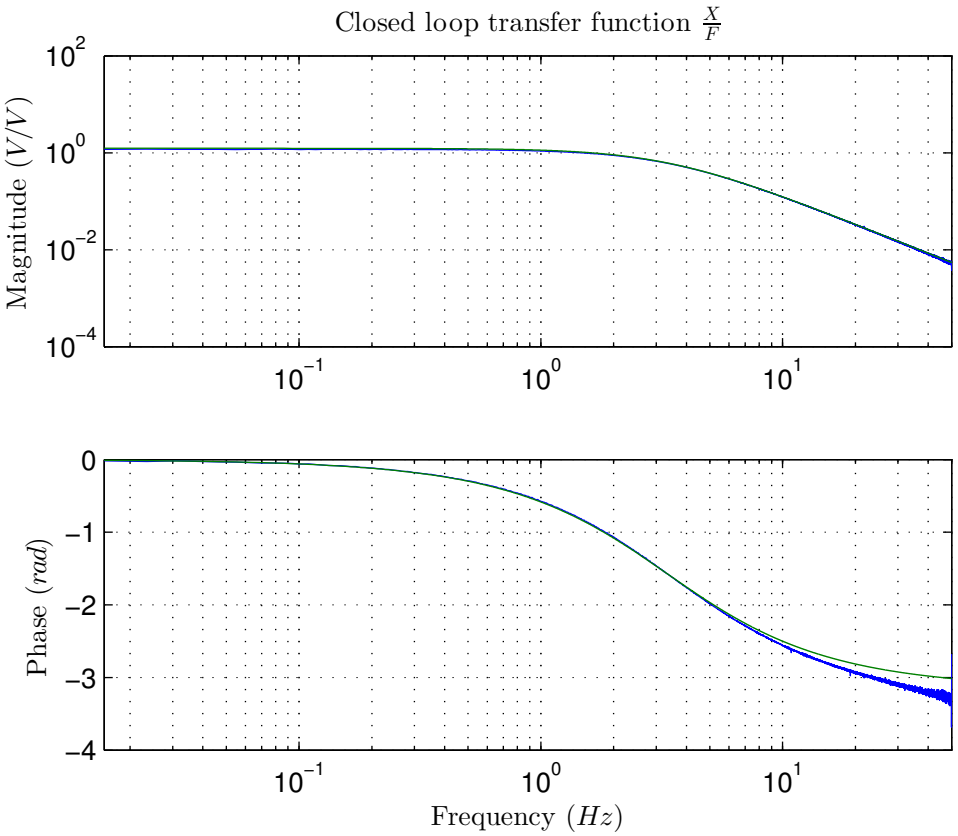


**Figure 7.4.:** Direct measurement of $\frac{X}{F}$ closed loop transfer function at low frequency (blue line) and the simple pendulum model with critical damping (green line). Conditions are the same of Fig. 7.3, because they have been measured together.

## 7.3. Closed Loop Transfer Function

Using the same configuration used for the measurement of open loop transfer function, we have acquired separately the noise, in the time domain, that was sent to the coil summed to the feedback force for the critical damping. Of course the superposition principle applies, so that it's possible to measure both open loop (Fig. 7.3) and closed loop transfer functions, at the same time and in the same conditions.

This time, using the same procedures used in the previous section, the `tfest` fit returns $Q = 0.47499 \pm 0.00047$. The results is presented in Fig. 7.4, and it's in agreement with models: we are really modifying the $Q$-value, attaining a critical damping. The 5% difference between the measured $Q$ and the expected 0.5 can be easily reduced indeed, by tuning poles and zeros of the digital controller.

# 8

# Digital Synthesizer and Demodulation

In this chapter we present how a Linear Variable Differential Transformer sensor works, and how it is dimensioned inside Virgo's accelerometers. Then, it is described an algorithm to read the displacement using the new electronics of Advanced Virgo.

## 8.1. Linear Variable Differential Transformers

A LVDT consists of three solenoidal coils, placed end-to-end around a tube. The coil at the center is the primary coil, and the two outer coils are the called secondary coils. A cylindrical ferromagnetic core, attached to the object whose position is to be measured, is free to move along the axis of the tube.[1] A carrier sine wave

$$V_p(t) = \sin(\Omega t) \tag{8.1}$$

at $\Omega = 2\pi \cdot 50\,\mathrm{kHz}$ with unitary amplitude, drives the primary and causes a voltage to be induced in each secondary. The output of our device is the difference of these two voltages, and it can be written as

$$V_s(t) = A(t)\sin(\Omega t + \varphi) \tag{8.2}$$

where $A(t)$ is the signal directly proportional to the displacement (at least near to the center) and $\varphi$ is a - usually small - primary to secondary coil phase shift. In practice, phase shift is almost certain to exist in the return signal due to the effect of stray capacitance in the transducer and connecting leads, as well as from tolerance and drift effects associated with analog components in the signal path. [35]

[1] Actually, in accelerometer LVDT, there is no ferromagnetic core: the primary coil is attached to the external structure, while secondary coils are integral with the pendulum. In this way, vacuum is used as medium, because of the incompatibility of a standard ferromagnetic core with the ultra high vacuum of Virgo.

### 8.1.1. Operation of a Transformer

Let's see in details how a LVDT works. This will be useful later for the analysis of the propagation of noise from primary coil to secondary coils.

According to Faraday's law of induction, voltage $\mathcal{E}$ induced in a coil made by $N$ turns is given by

$$\mathcal{E} = -N\frac{\partial \Phi}{\partial t} \tag{8.3}$$

where $\Phi$ is the magnetic flux through the loop. In the case of LVDT, magnetic field $B(z, r, t)$ is induced by the current flowing in primary coil: it's value is symmetric with respect to the coil axis $z$, and so depends only on $z$ and on the distance from the axis $r = \sqrt{x^2 + y^2}$ (where $x$ and $y$ are directions orthogonal to $z$). The magnetic flux through a secondary coil of radius $R$ is

$$\Phi(z, t) = \int_0^R \vec{B}(z, r, t) \cdot \hat{n} 2\pi r dr \tag{8.4}$$

The computation of $B$, and then of its flux, is complicated because it involves elliptic integrals. Omitting details, the $z$ component of $B$, $B_z = \vec{B} \cdot \hat{n}$, is given by

$$B_z(z, r, t) = \frac{i(t)\,\mu_o}{2a}\frac{1}{\pi\sqrt{q}}\left(K(k) + \frac{(-\alpha^2 - \beta^2 + 1)\,E(k)}{q - 4\alpha}\right)$$

where:

- $i(t)$ is current in the wire;
- $a$ radius of the current loop;
- $\alpha = \frac{r}{a};\ \beta = \frac{x}{a};\ q = (\alpha + 1)^2 + \beta^2;\ k = \sqrt{\frac{4\alpha}{q}};$
- $K(k)$ and $E(k)$ are complete elliptic integral of the first kind and complete elliptic integral of the second kind, respectively.

Since in a transformer the flux can be written as $\Phi = \mathcal{P} N_p I_p$, where $\mathcal{P}$ is the permeance[2] and $N_p I_p$ is the current-turns of the primary coil, we can figure out that permeance and flux are functions of the distance between coils: if we let this distance variate during time, then signals are differently induced in each secondary coil. A numerical computation (presented in Fig. 8.1) shows that a value $z_0$ exists, such that the derivative $\frac{\partial \mathcal{P}}{\partial z}$ is maximized for $z = \pm z_0$, with value $\delta\mathcal{P}_0$. Those at $z = \pm z_0$ are of course the best places where to put the secondary coils in a LVDT in order to obtain the best SNR, because a perturbation in $z$ would produce the maximum effect on the voltage induced in secondary coils. For the Virgo horizontal accelerometers,

[2]The SI unit of magnetic permeance is "webers per ampere-turn", that is $\mathrm{Wb\,A^{-1}}$.

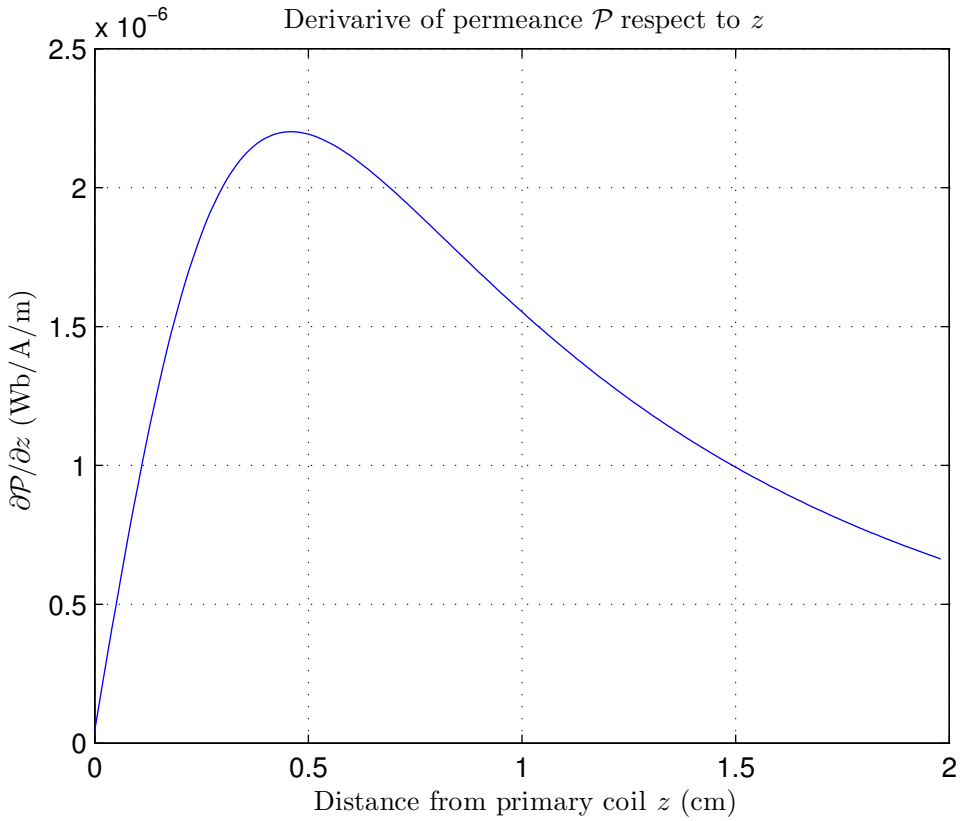


**Figure 8.1.:** Numerical computation of $\frac{\partial \mathcal{P}}{\partial z}$ per current-turns unit flowing a ⌀45 mm primary coil, like that of Virgo accelerometers

the maximum is at $z_0 = 4.7\,\mathrm{mm}$, where $\delta\mathcal{P}_0 = 2.20\,\mu\mathrm{Wb\,A^{-1}\,m^{-1}}$. Actually, in the accelerometer secondary coils were placed at $z_1 = 6\,\mathrm{mm}$, where

$$\delta\mathcal{P}_1 = 2.12\,\mu\mathrm{Wb\,A^{-1}\,m^{-1}}$$

In case of a sensor whose primary coil is driven by a carrier sine wave with angular frequency $\Omega$, the maximum voltage induced in secondary coils is

$$\mathcal{E}_{MAX} = 2N_s\Omega\Phi_{MAX}$$

where $\Phi_{MAX}$ is the maximum of the flux during time and $N_s$ are the turns of secondary coil. Then, sensitivity of LVDT can be obtained with the following relation:

$$\begin{aligned} \frac{\partial \mathcal{E}_{MAX}}{\partial z} = \xi &= 2\Omega N_s \frac{\partial \Phi_{MAX}}{\partial z} \\ &= 2\Omega N_s N_p I_p \delta\mathcal{P}_1 \end{aligned} \tag{8.5}$$

(of course here $N_p I_p$ represents the maximum of the current-turns). In SI, $\xi$ is

expressed as V/m. In our sensor these variables assume the following values:

$$\begin{aligned} \Omega &= 2\pi \cdot 50\,\mathrm{kHz} \\ N_s &= 450 \\ N_p &= 41 \\ N_p I_p &= 1.14\,\mathrm{A} \end{aligned}$$

In this conditions, according to 8.5, the sensitivity of Virgo accelerometer LVDT is

$$\xi = 610\,\mathrm{V/m} \tag{8.6}$$

where voltage are measured at the maximum during a period.

## 8.2. Demodulation of the LVDT Signal

A demodulator allows us to extract $A(t)$ from $V_s(t)$: in essence, it takes the output signal, then multiplies it by the reference signal $\sin(\Omega t + \varphi_0)$ - that, if need be, can be delayed by an arbitrary phase $\varphi_0$ - and, eventually, integrates it over a specified time. Analytically,

$$\begin{aligned} I_0(t) &= A(t)\sin(\Omega t + \varphi) \cdot \sin(\Omega t + \varphi_0) \\ &= \frac{A(t)}{2}\left[\cos(\Delta\varphi) - \cos(2\Omega t + \varphi + \varphi_0)\right] \end{aligned} \tag{8.7}$$

where we have defined

$$\Delta\varphi = \varphi - \varphi_0$$

In the same way, using the orthogonality of sine and cosine functions, it is possible to get an another, independent signal by multiplying by $\cos(\Omega t + \varphi_0)$, i.e. the reference wave shifted by $\pi/2$:

$$\begin{aligned} Q_0(t) &= A(t)\sin(\Omega t + \varphi) \cdot \cos(\Omega t + \varphi_0) \\ &= \frac{A(t)}{2}\left[\sin(\Delta\varphi) + \sin(2\Omega t + \varphi + \varphi_0)\right] \end{aligned} \tag{8.8}$$

In both cases, the resulting signal is $A$, multiplied by the sum of a DC signal and a signal at twice the reference signal frequency $\Omega$. If the bandwidth of $A$ is much smaller than $\Omega$, a proper low-pass filter - with gain 2 at low frequencies - applied to these two signals finally lets us to obtain

$$\begin{aligned} I(t) &= A(t)\cos(\Delta\varphi) \\ Q(t) &= A(t)\sin(\Delta\varphi) \end{aligned} \tag{8.9}$$

i.e. two signals both proportional to $A(t)$ and to a constant. This is the principle of a **lock-in amplifier**, also known as a **phase-sensitive detector** for this reason. The letters $I$ and $Q$ are used in electrical engineering to represent two amplitude-modulated sinusoids that are offset in phase by one-quarter cycle: they stand for *in-phase* and *quadrature* components, respectively.

To get the maximum SNR from the in-phase component $I$, we have to maximize the coefficient $\cos(\Delta\varphi)$. Obviously, the optimal case shows up for $\Delta\varphi = 0$, that can be achieved by tuning $\varphi_0 = \varphi$. Nevertheless, we don't know a priori the value of $\varphi$. Luckily, a slightly non-zero $\Delta\varphi$ implies only a second-order effect in $I$, so that the tuning does not require an extreme precision.

In our system, the simplest way to measure the phase shift is

$$\Delta\varphi = \tan^{-1}\left(\frac{Q(t)}{I(t)}\right) \tag{8.10}$$

However this is not a good approach, as the calculation of $\tan^{-1}$ in double precision floating point takes a long time to the DSP ($\sim 300$ clock cycles), and also because $I(t)$ often goes through zero. This identity is an alternative approach:

$$\frac{I(t)\cdot Q(t)}{I^2(t)+Q^2(t)} = \frac{A^2(t)\sin(\Delta\varphi)\cos(\Delta\varphi)}{A^2(t)} = \frac{\sin(2\Delta\varphi)}{2} \tag{8.11}$$

The main advantage is to have the denominator $A^2(t)$ always greater or equal to 0, making the computation of the division safer. Furthermore,

$$\frac{\sin(2\Delta\varphi)}{2} = \Delta\varphi$$

at the first order in $\Delta\varphi$: this means that it's possible to avoid the calculation of $\sin^{-1}$ (as laborious as $\tan^{-1}$).

### 8.2.1. Effects of a Quadrature Term

In addition to phase shift, that is relatively little annoying, a real LVDT shows also another tedious effect: actually, in the secondary coils voltage 8.2 a term $B$ appears, in quadrature to $A$:

$$V_s(t) = A(t)\sin(\Omega t+\varphi) + B(t)\cos(\Omega t+\varphi) \tag{8.12}$$

In this backdrop, we need to rewrite equation 8.7 and 8.8:

$$\begin{aligned} I_0(t) &= [A(t)\sin(\Omega t+\varphi) + B(t)\cos(\Omega t+\varphi)]\cdot\sin(\Omega t+\varphi_0) \\ &= \frac{A(t)}{2}[\cos(\Delta\varphi) - \cos(2\Omega t+\varphi+\varphi_0)] \\ &\quad -\frac{B(t)}{2}[\sin(\Delta\varphi) - \sin(2\Omega t+\varphi+\varphi_0)] \end{aligned}$$

and

$$\begin{aligned} Q_0(t) &= [A(t)\sin(\Omega t+\varphi)+B(t)\cos(\Omega t+\varphi)]\cdot\cos(\Omega t+\varphi_0) \\ &= \frac{A(t)}{2}[\sin(\Delta\varphi)+\sin(2\Omega t+\varphi+\varphi_0)] \\ &\quad +\frac{B(t)}{2}[\cos(\Delta\varphi)+\cos(2\Omega t+\varphi+\varphi_0)] \end{aligned}$$

These, after the same low-pass filter, become

$$\begin{aligned} I(t) &= A(t)\cos(\Delta\varphi)-B(t)\sin(\Delta\varphi) \\ Q(t) &= A(t)\sin(\Delta\varphi)+B(t)\cos(\Delta\varphi) \end{aligned} \tag{8.13}$$

or equivalently, in matrix notation,

$$\begin{pmatrix} I(t) \\ Q(t) \end{pmatrix} = \begin{pmatrix} \cos(\Delta\varphi) & -\sin(\Delta\varphi) \\ \sin(\Delta\varphi) & \cos(\Delta\varphi) \end{pmatrix} \begin{pmatrix} A(t) \\ B(t) \end{pmatrix} \tag{8.14}$$

In other words, the vector $(I(t), Q(t))$ is nothing more than $(A(t), B(t))$ rotated by an angle $\Delta\varphi$. Now, we have two equations for three unknowns: there is no way to measure $\Delta\varphi$ by the only measure of $(I(t), Q(t))$, so that it's impossible to isolate the displacement signal $A(t)$ from the quadrature term. The presence of a non-adjusted phase shift inevitably leads to a mixing of $A$ and $B$ on the output of the system.

Fortunately, there's no need to be discouraged: if $|B| \ll |A|$ (the dependence on time is omitted from now on), the contribution of the quadrature term can be actually neglected, in order to use either equation 8.10 or 8.11 to measure $\Delta\varphi$. For example, defining

$$r = \frac{B}{A}$$

equation 8.11 using $I$ and $Q$ of 8.13 would become

$$\frac{I\cdot Q}{I^2+Q^2} = \frac{\sin(2\Delta\varphi)+2r\cos(2\Delta\varphi)-r^2\sin(2\Delta\varphi)}{2(1+r^2)}$$

whose denominator is strictly greater than 0 if $r \neq 0$. At the first order in $r$ and in $\Delta\varphi$, it shrinks to

$$\frac{I\cdot Q}{I^2+Q^2} = \Delta\varphi + r \tag{8.15}$$

In conclusion, this ratio can be used for calculate $\Delta\varphi$ in adequate conditions. Furthermore the denominator is always positive, and a division by zero never occurs. The error introduced by the quadrature signal $B$ is just $r$.

Now, the problem becomes how to get $r \to 0$, i.e. $|B| \ll |A|$. Even if $B$ is relatively small and constant over the time, and independent from the displacement, we don't know the initial size of the signal $A$, that could also be zero. Qualitatively, we can apply a relatively strong force to the mass through the coil actuator, in order to get a displacement $x - x_0$ as big as possible: this will increase $A$ while, at the same time, $B$ remains constant. Then, we perform a measurement of $\varphi$, set $\varphi_0 = \varphi$ and eventually release the force. At that point, we'll have $I = A$ and $Q = B$. This can be achieved by a finite-state machine implemented in the FPGA.

## 8.3. An Algorithm to Demodulate with Phase Locking

Today, digital techniques can be applied in order to automate this tuning. In particular, a **Phase-Locked Loop** (PLL) is a control system that generates an output signal whose phase is related to the phase of an input signal. We can use this technique to measure the phase shift and then to tune the oscillator used for the demodulation with a phase $\varphi_0 = \varphi$.

A digital PLL-based loop can be implemented in FPGA, to perform amplitude demodulation using the relation in 8.15 for a smart measurement of $\varphi$ and thus allowing to get the maximum SNR from the in-phase component $I$. Such a system can be used to read LVDT, both those inside the accelerometer and the others used in the Superattenuator inertial control.

The schematic diagram is depicted in Fig. 8.2. The principle is quite simple: after the reconstruction of $I$ and $Q$ from LVDT secondary coils, they are combined to get $\Delta\varphi$. This value passes through an integrator, that slowly changes the initial phase $\varphi_0$ of a sine-cosine wave generator used in the demodulation. Supposing $r \to 0$, as time passes $\varphi_0$ tends to $\varphi$, giving $\Delta\varphi \to 0$. At this point the system is stable: we get $I \to A$, $Q \to B$, and $\varphi_0$ that is a direct measurement of time shift.

First of all the logic has been tested in MATLAB and Simulink, simulating a discrete time model. This has been done mostly to check the performance and to tune the parameters. The result of a simulation with a 1 Hz signal, $B = 0$ and $\varphi = 1.4$ rad is presented in Fig. 8.3: as expected, while the feedback phase $\varphi_0$ tends to the right value, $I \to A$ and $Q \to 0$.

Eventually, I have developed a project in Quartus II 13.1.0, both writing VHDL code and using schematic files, to be implemented in Advanced Virgo electronics. Due to the complex handling of floating point values in a FPGA, all the vectors have been treated as signed and/or unsigned integers, using `numeric_std` package. On the one hand this simplifies several things: for example, the output of ADC belong to this data type, and so no conversions are needed; it is also trivial to perform multiplication and division by powers of two. On the other hand, we need to pay attention to the number of bits used in the arithmetics, to avoid losses of precision.

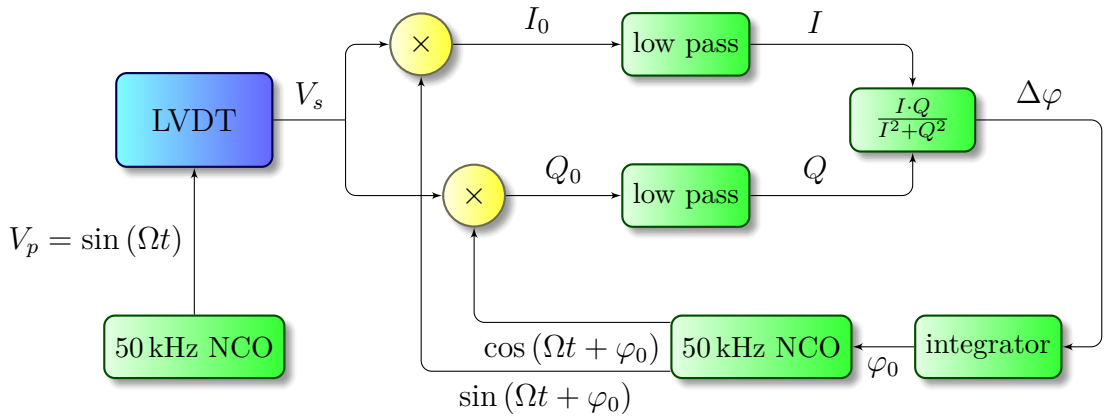


**Figure 8.2.:** Schematic diagram of the PLL-based demodulation with phase locking

## Numerically Controlled Oscillator

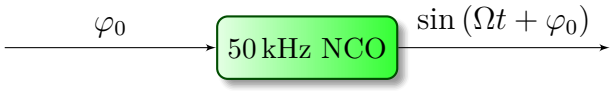


The central block is the *Numerically Controlled Oscillator* (NCO): this term indicates a digital signal generator which creates a synchronous (i.e. clocked), discrete-time, discrete-valued representation of a waveform. A first NCO is used to generate two *coherent* 50 kHz sinusoidal waves, phase-shifted by $\pi/2$ each other, that are used for the demodulation. Another identical and independent NCO is used to drive the primary coil of LVDT.

An NCO generally consists of two parts:

- A *Phase Accumulator* (PA), which adds a frequency control value to the value held at its output at each clock sample.
- A *Phase-to-Amplitude Converter* (PAC), which uses the PA output word as an index into a waveform Look-Up Table (LUT), to provide a corresponding amplitude sample. Sometimes interpolation is used with the look-up table to provide better accuracy and reduce phase error noise.

I have written a VHDL code, based on the excellent LGPL-licensed project *DDS Synthesizer*, developed since 2008 by Martin Kumm. [36] Let's see the essence of the algorithm, whose schematic is in Fig. 8.4, looking at some extracts from the VHDL code.

```
1 -- phase accumulators
2 ftw_accu <= ftw_accu + ftw_i;
```

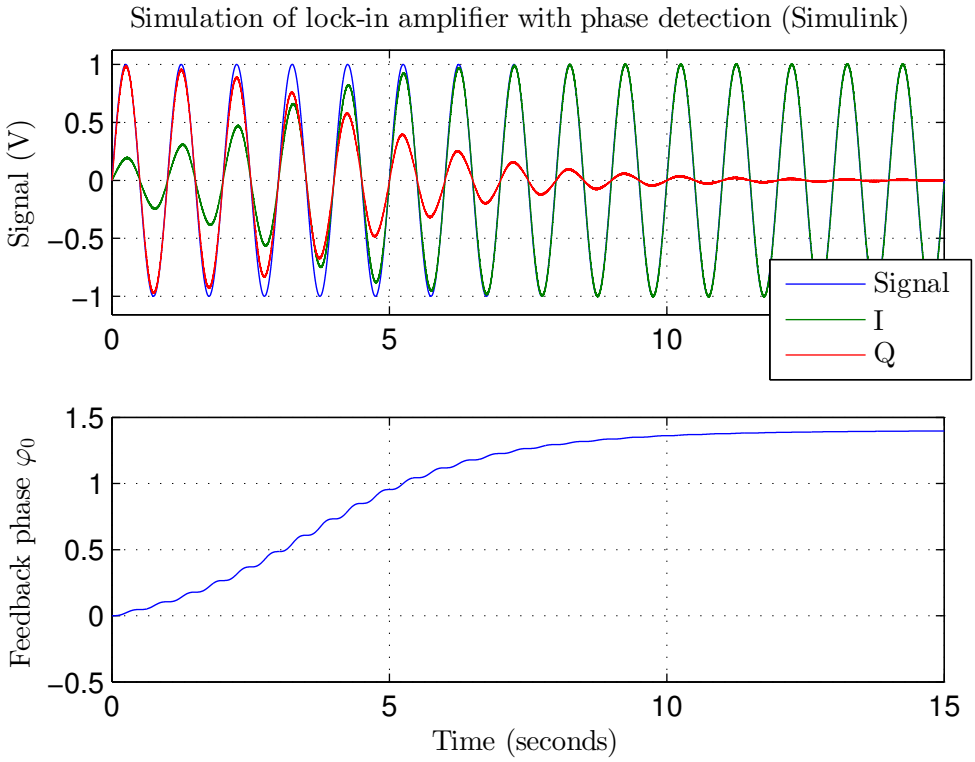


**Figure 8.3.:** Simulation of a PLL-based demodulation with phase locking made in Simulink, using the logic in Fig. 8.2. For reasons explained later, the division on the top right block hasn't been performed: this explains the wavy behavior of the feedback phase.

The frequency tuning word $FTW$ (`ftw_i` in the code) is an unsigned $N$-bit number, that specifies the output frequency $f_{DDS}$ as

$$f_{DDS} = \frac{FTW}{2^N} f_s \tag{8.16}$$

where $f_s$ is the clock frequency. In other words, the frequency resolution is $f_s/2^N$. The frequency tuning word passes through the PA. Its output $F$ (`ftw_accu` in the code) is a periodic ramp and has the same length $N$.

```
1 sin_phase <= ftw_accu(N-1 downto N-M) + phase_i;
2 cos_phase <= ftw_accu(N-1 downto N-M) + phase_i
3  + to_unsigned(2**(M-2),M);
```

At this point, the first $M$ bits of $F$ are defined $\Phi_{sin}$ (`sin_phase`),[3]

$$\underbrace{F_{N-1} \ \ldots \ F_{N-M}}_{\Phi_{sin}} \ F_{N-M-1} \ \ldots \ F_0$$

[3]We're dealing with a big-endian system

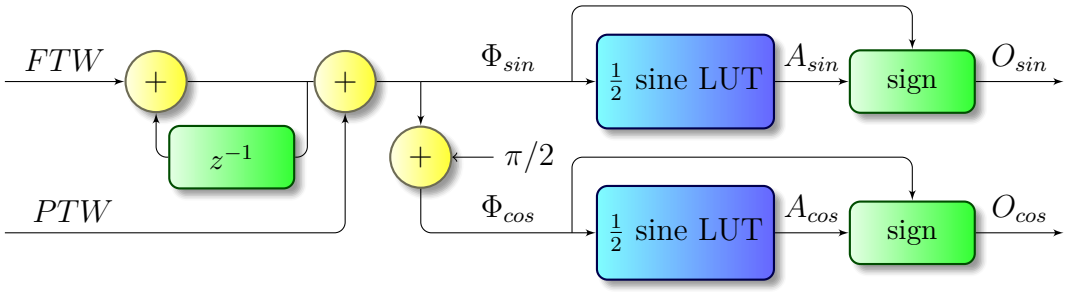


**Figure 8.4.:** Schematic diagram of the Numerically Controlled Oscillator. Phase accumulator is on the left, phase-to-amplitude converter on the right.

and, simultaneously, a variable $\Phi_{cos}$ (`cos_phase`) is defined as $\Phi_{cos} = \Phi_{sin} + 2^{M-2}$. A key feature of this NCO is that it is possible to add an arbitrary value $M$-bit phase tuning word $PTW$ (`phase_i`) to both $\Phi$, that can be interpreted as a initial phase, but that can also change during the time. In this sense, note that $PTW$ acts as the integral of $FTW$: a constant value on $FTW$ and a ramp on $PTW$ would produce the same effect.

```
1 -- lut readout
2 sin_lut_out <= sine_lut(to_integer(sin_phase(M-2 downto 0)));
3 cos_lut_out <= sine_lut(to_integer(cos_phase(M-2 downto 0)));
```

Then $\Phi_{sin}$ and $\Phi_{cos}$ are used to read into a LUT that stores the first half period of a sine (the positive one), multiplied by $2^{P-1}$ and sampled $2^{M-1}$ times at $P-1$ bits, with $M < N$:

$$A_{sin} = 2^{P-1} \left| \sin\left( \frac{\tilde{\Phi}_{sin}}{2^{M-1}} \pi \right) \right| \tag{8.17}$$

and

$$\begin{aligned} A_{cos} &= 2^{P-1} \left| \sin\left( \frac{\tilde{\Phi}_{cos}}{2^{M-1}} \pi \right) \right| \\ &= 2^{P-1} \left| \sin\left( \frac{\tilde{\Phi}_{sin}}{2^{M-1}} \pi + \frac{2^{M-2}}{2^{M-1}} \pi \right) \right| \\ &= 2^{P-1} \left| \cos\left( \frac{\tilde{\Phi}_{sin}}{2^{M-1}} \pi \right) \right| \end{aligned} \tag{8.18}$$

where $A_{sin}$ and $A_{cos}$ (`sin_out_lut` and `cos_out_lut`) are unsigned integers with $P-1$ bits, and $\tilde{\Phi}$ represents the last $M-1$ bits of $\Phi$:

$$\Phi_{M-1} \underbrace{\Phi_{M-2} \ \ldots \ \Phi_0}_{\tilde{\Phi}}$$

Only half a period of sine is stored because of the property $\sin(x) = -\sin(x+\pi)$.[4] The first two bits of $\Phi_{sin}$ and $\Phi_{cos}$ represents the quadrant relative the angle, that is related to the sign of sine and cosine: the sine is positive in the first and in the second ones, while the cosine in the first and in the forth ones. Furthermore, the phase of cosine is one quadrant ahead that of sine: this is why we define only one 2-bit unsigned integer signal `quadrant`, relative to the sine:

```
1 quadrant <= sin_phase(M-1 downto M-2);
```

The remaining last $N - M$ bits of $F$ are discarded in the PAC, as they are needed only for the frequency tuning. They could be used for an eventual interpolation, to provide better accuracy and reduce phase error noise.

In conclusion, the outputs of NCO are two $P$-bit signed integers, $O_{sin}$ (`sin_o`) and $O_{cos}$ (`cos_o`), that consist of $A$ with the adjusted sign, and that are written just after the clock rising edge:

```
1 -- writing output (quadrant is that of sin)
2 sin_o <= sin_lut_out_delay
3   when (quadrant_2delay = "00" or quadrant_2delay = "01")
4   else sin_lut_out_inv_delay;
5 cos_o <= cos_lut_out_delay
6   when (quadrant_2delay = "00" or quadrant_2delay = "11")
7   else cos_lut_out_inv_delay;
```

taking, from the previous iteration,

```
1 -- updating quadrant memory
2 quadrant_delay <= quadrant;
3 quadrant_2delay <= quadrant_delay;
4
5 -- updating output for the next iteration
6 sin_lut_out_inv_delay <= to_signed(-1*to_integer(sin_lut_out), P);
7 sin_lut_out_delay <= sin_lut_out;
8 cos_lut_out_inv_delay <= to_signed(-1*to_integer(cos_lut_out), P);
9 cos_lut_out_delay <= cos_lut_out;
```

The signals, with self-explaining suffixes `_delay` and `_2delay`, are needed to take into account the delays of the algorithm: the latency of this NCO is 2 clock cycles.

In the implementation used in our test, we have used $N = 24$, $M = 10$ and $P = 10$. Look-up tables, compatible with the code, are generated by a MATLAB script, with arbitrary $M$ and $P$.

[4] The original Kumm's algorithm stores only the first quarter of the period of a sine on the LUT, exploiting the property $\sin\left(x+\frac{\pi}{2}\right) = \sin\left(-x+\frac{\pi}{2}\right)$. However, in this way the value of the maximum of the sine is not stored in the LUT and has to be written in the code, generating an exception inside the algorithm: this problem is avoided, storing the whole first half period.

## Low Pass Filters


The output of LVDT is acquired by ADC in a 24-bit value, and multiplied by the 10-bit outputs of NCO to form $I_0$ and $Q_0$, each one with 34 bits. A low pass filter is then needed removes the $2\Omega$ contribution.

Instead of a simple low pass filter, we can use a property of the average. In Z-transform, the average of $n$ samples as this form:

$$\frac{Y}{X} = \frac{1 + z^{-1} + z^{-2} + \ldots + z^{-n+1}}{n} = \frac{1}{n}\frac{1 - z^{-n}}{1 - z^{-1}} \tag{8.19}$$

that corresponds to a simple difference equation

$$y_i = \frac{y_{i-1} + x_i - x_{i-n}}{n} \tag{8.20}$$

Its sinc-like frequency response (see Fig. 8.5) has the property to have a notch in all multiples of $f_c/n$, when the wave has a integer number of periods under the averaging window.[5]

At this point we would like also to downsample the stream of data: ADC are read at $f_c = 3.84\,\text{MHz}$, that is pretty high for our purpose. So, the strategy is the following: an accumulator averages $n = 19$ samples, then its output is read and the accumulator is reset.

Why 19? Because it is the nearest integer to 19.2, which would allow to put a notch at $\frac{3.84\,\text{MHz}}{19.2} = 200\,\text{kHz}$. Choosing $n = 19$, the first notch is actually at $f_c = 202.1\,\text{kHz}$, that is still acceptable. And also, why do we chose 200 kHz and not 100 kHz, where we have the $2\Omega$ contribution of demodulation? Because resampling the stream at 100 kHz would create some aliasing in DC, as the notch has a very narrow band (look at 8.7 and 8.8: the signal $A(t)$ is amplitude modulated around $2\Omega$). This is not a problem if we downsample at 200 kHz, because there should be only a little noise.

This step is performed by *ALTACCUMULATE* Quartus megafunction. Of course, this first average does not filter too much at 100 kHz: from transfer function 8.19,

[5] Sinc-like behavior is a direct consequence of the Fourier transform, in the analog domain, of a unit box ($f(t) = a^{-1}$ if $t < a$ else $f(t) = 0$, where $a > 0$), that is proportional to cardinal sine function $\text{sinc}x = \frac{\sin x}{x}$.

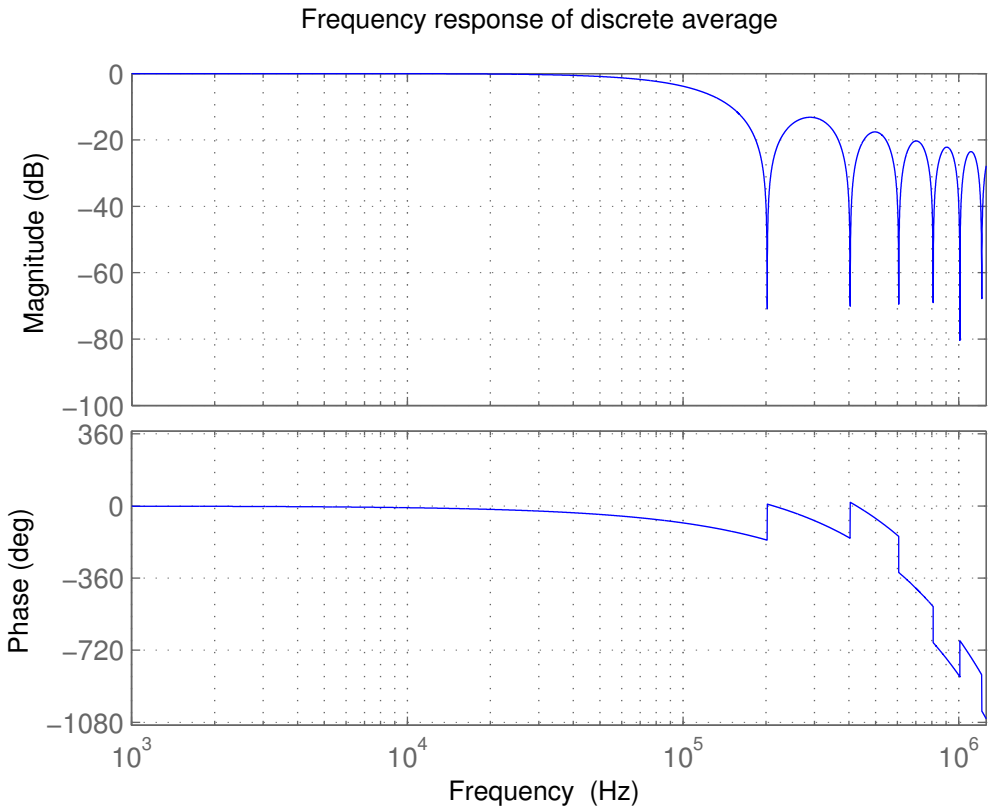


**Figure 8.5.:** Frequency response of a discrete average, with $n = 19$ and $f_c = 3.84\,\text{MHz}$. Notches are at 201.2 kHz and at its multiples, and the phase delay that scales linearly. Note the similarity with the sensitivity of a Michelson interferometer, in Fig. 2.5: despite the different fields of application, the principle is the same.

with $n = 19$ and $z = e^{i2\pi f/f_c}$ (cf. 4.4), there its magnitude response corresponds at

$$\begin{aligned} U_1 &= \left| \frac{1}{19} \frac{1 - \exp\left(-19 \cdot i2\pi \frac{100\,\text{kHz}}{3.84\,\text{MHz}}\right)}{1 - \exp\left(-i2\pi \frac{100\,\text{kHz}}{3.84\,\text{MHz}}\right)} \right| \\ &= \left| \frac{1}{19} \frac{\sin\left(19 \cdot \pi \frac{100\,\text{kHz}}{3.84\,\text{MHz}}\right)}{\sin\left(\pi \frac{100\,\text{kHz}}{3.84\,\text{MHz}}\right)} \right| \\ &\simeq \text{sinc}\,(\pi/2) = -4\,\text{dB} \end{aligned} \tag{8.21}$$

At this point, a second average takes places, with $n = 4$, this time without downsampling (it is called a moving average): being now $f_c = 202.1\,\text{kHz}$, the first two notches are placed at 50.5 kHz and 101 kHz. The magnitude of frequency response

at 100 kHz is

$$\begin{aligned} U_2 &= \left| \frac{1}{4} \frac{1 - \exp\left(-4 \cdot i2\pi \frac{100\,\text{kHz}}{202.1\,\text{kHz}}\right)}{1 - \exp\left(-i2\pi \frac{100\,\text{kHz}}{202.1\,\text{kHz}}\right)} \right| \\ &= \left| \frac{1}{4} \frac{\sin\left(4 \cdot \pi \frac{100\,\text{kHz}}{202.1\,\text{kHz}}\right)}{\sin\left(\pi \frac{100\,\text{kHz}}{202.1\,\text{kHz}}\right)} \right| \\ &= 1.6 \times 10^{-2} = -35\,\text{dB} \end{aligned} \tag{8.22}$$

This is done with a simple VHDL code based on a *First In, First Out* (FIFO). Here is the code (note the implementation of 8.20):

```
1  library ieee;
2  use ieee.std_logic_1164.all;
3  use ieee.numeric_std.all;
4
5  entity moving_average is
6   generic(
7    DATA_WIDTH     : integer := 24
8   );
9   port(
10    clk_i    : in  std_logic;
11    rst_i    : in  std_logic;
12    sample   : in  signed(DATA_WIDTH-1 downto 0);
13    output   : out signed(DATA_WIDTH-1 downto 0)
14   );
15 end moving_average;
16
17 architecture moving_average_arch of moving_average is
18
19  type fifo is array(3 downto 0) of signed(DATA_WIDTH+1 downto 0);
20
21  signal samples_fifo: fifo := (others => (others => '0'));
22  signal sample_long : signed(DATA_WIDTH+1 downto 0)
23   := (others => '0');
24  signal sum: signed(DATA_WIDTH+1 downto 0) := (others => '0');
25
26 begin
27
28  process (clk_i, rst_i)
29
30   begin
31   sample_long <= to_signed(to_integer(sample), DATA_WIDTH+2);
32
33   if rst_i='1' then
34    samples_fifo <= (others => (others => '0'));
```

```
35      sum <= (others => '0');
36
37    elsif rising_edge(clk_i) then
38      -- difference equation of average:
39      sum <= sum + sample_long - samples_fifo(0);
40      -- sliding of FIFO:
41      samples_fifo <= sample_long & samples_fifo(3 downto 1);
42    end if;
43
44  end process;
45  -- division by 4, cropping the last 2 digits of sum:
46  output <= sum(DATA_WIDTH+1 downto 2);
47
48 end moving_average_arch;
```

In the last step of the block, a first order digital low pass filter, with cutoff angular frequency of 100 rad/s, is implemented[6] to further clean the $2\Omega$ signal. Its difference equation and transfer function are[7]

$$\begin{aligned} y_n &= (1-\alpha)\,x_n + \alpha \cdot y_{n-1} \\ \frac{Y}{X} &= \frac{1-\alpha}{1-\alpha \cdot z^{-1}} \end{aligned} \tag{8.23}$$

The term $(1-\alpha)$ in front of $x_n$ and at numerator in the second line is needed to have unity gain in DC. The value $\alpha$ determines the time constant $\tau$ of the filter, with the relation

$$\log \alpha = -\frac{T}{\tau} \tag{8.24}$$

where $T$ is the sampling period, $(202.1\,\text{kHz})^{-1} = 4.9\,\mu\text{s}$ in our case. For a cutoff angular frequency of 100 rad/s, $\tau = (100\,\text{rad/s})^{-1} = 10\,\text{ms}$, we need

$$\log \alpha = -\frac{4.9\,\mu\text{s}}{10\,\text{ms}} \Rightarrow \alpha = 0.999505 \tag{8.25}$$

that is very close to the ratio $\frac{2047}{2048}$ (within 0.001%), thus allowing a simple implementation at 12 bits in the FPGA.

[6] Even if $100\,\text{rad/s} \cong 16\,\text{Hz}$ is smaller than the bandwidth of the accelerometer, it is enough for the measurement of $\varphi$.

[7] Note that such a filter does not correspond to a continuous time filter through bilinear transformation. Actually this transformation is called *impulse invariance*, designing discrete-time filters from continuous-time filters, in which the impulse response of the continuous-time system is sampled to produce the impulse response of the discrete-time system. If obtained from a first order continuous-time low pass filter using bilinear transformation, the transfer function in 8.23 would have an additional term in $z^{-1}$ at the numerator, so that the digital filter would require an additional sum, of a term proportional to $x_{n-1}$. Even if the attenuation at high frequencies would be better, for the purposes of this system it is enough.

In conclusion, the attenuation of 8.23 at 100 kHz is

$$\begin{aligned} U_3 &= \left| \frac{1 - \frac{2047}{2048}}{1 - \frac{2047}{2048} \cdot \exp\left(-i2\pi \frac{100\,\text{kHz}}{202.1\,\text{kHz}}\right)} \right| \\ &= 2.4423 \times 10^{-4} = -72\,\text{dB} \end{aligned} \tag{8.26}$$

Summing 8.21, 8.22 and 8.26, in the filtering block the $2\Omega$ contribution is attenuated by

$$U_{tot} = -111\,\text{dB} \tag{8.27}$$

This is enough for the FPGA-based demodulation with automatic phase detection. Additional filters could be placed later in DSP, also directly on $I_0$: its double-precision floating point handling is for sure much better than what is worth to implement in FPGA.

## From $I$ and $Q$ to $\Delta\varphi$

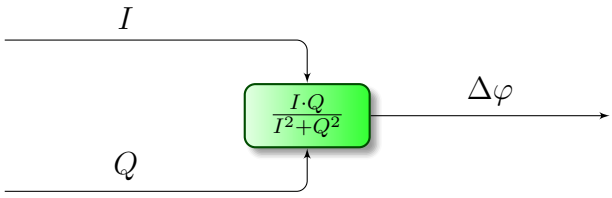


Once passed through the respective low pass filters, $I$ and $Q$ are used to get $\Delta\varphi$ using equation 8.15. Here a problem occurs: a division between 32-bit integers, performed by *LPM_DIVIDE* megafunction, would take both several clock cycles and a lot of resources inside the FPGA. The choice is to avoid the computation of this division, and to carry out only $I \cdot Q$. Neglecting $r$,

$$I \cdot Q = \Delta\varphi \left(I^2 + Q^2\right)$$

For the purpose of the phase-detection feedback, this has a minimum impact. Indeed, during the calibration $I^2 + Q^2$ is quite constant, probably predictable and, by the way, always $> 0$: omitting the division, we only modify the gain of the loop, that can be handled later.

## Integrator

Finally, I have designed an integrator: it consists of a multiplier by a 10-bit tunable constant $\alpha$, with a simple accumulator in cascade. The input of integrator is a 24-bit integer, that becomes 34 after the multiplier. An *ALTACCUMULATOR* sums the 24 most significant bits of $\Delta\varphi$ at $f_c = 202.1\,\text{kHz}$, and it is never reset. The 10 most significant bits of its output are used to tune the $\varphi_0$ in the NCO, to close the loop. The difference equation and transfer function of this integrator are

$$\begin{aligned} y_n &= y_{n-1} + \beta \cdot x_n \\ \frac{Y}{X} &= \frac{\beta}{1 - z^{-1}} \end{aligned} \tag{8.28}$$

The characteristic time is infinite (compare with 8.23 and 8.24), as the unit sample response is the step function.

### 8.3.1. Stability of the System, Simulations and Limits

Due to the high nonlinearity of this system (some elements, like NCO, cannot be represented as transfer functions or state space matrices), its stability has to be verified in a simulation. The most important parameter is the loop gain, tunable through $\beta$ in 8.28: it is inversely proportional to the convergence time, but a too high gain could lead to instability.

After some simulations in MATLAB Simulink, performed to find the best parameters that lead to desired behavior, the project has been tested on a FPGA, using *SignalTap II* to read signals. To simulate the output of a LVDT, a low frequency signal has been synthesized and modulated with a carrier sine, phase-shifted by a random angle $\varphi$ generated by a linear congruential generator. After an hardware reset, the system generated a new phase and then tried to guess it. In these conditions, the algorithm converged to the real $\varphi$ in a couple of seconds, as shown in Fig. 8.6. A small offset between $\varphi_0$ and $\varphi$, it corresponds to few clock cycles, is expected. It is due to delays from the signal generation to the demodulation unit.

The main problem of this system is that it doesn't allow to distinguish a phase shift $\varphi$ from its supplementary $\pi - \varphi$. Indeed, the loop makes the phase $\varphi_0$ shift from the initial zero value toward the correct value, through the shortest path. If the real phase shift $|\varphi| < \frac{\pi}{2}$, then $\varphi_0$ converges to $\varphi$ without any problem. But, if $|\varphi| > \frac{\pi}{2}$, when $\varphi_0$ passes on $\pi - \varphi$, there it find a stable node: these two cases differ only for a sign of the cosine, because $\sin(\varphi) = \sin(\pi - \varphi)$ and $\cos(\varphi) = -\cos(\pi - \varphi)$. Looking at 8.9, this additional minus sign could belong also to the signal $A(t)$, so that the loop is perfectly stable.

In conclusion, a supplementary phase shift and the direction of the displacement cannot be physically distinguished each other. However this is a relative problem, as we usually deal with $|\varphi| \ll \frac{\pi}{2}$.

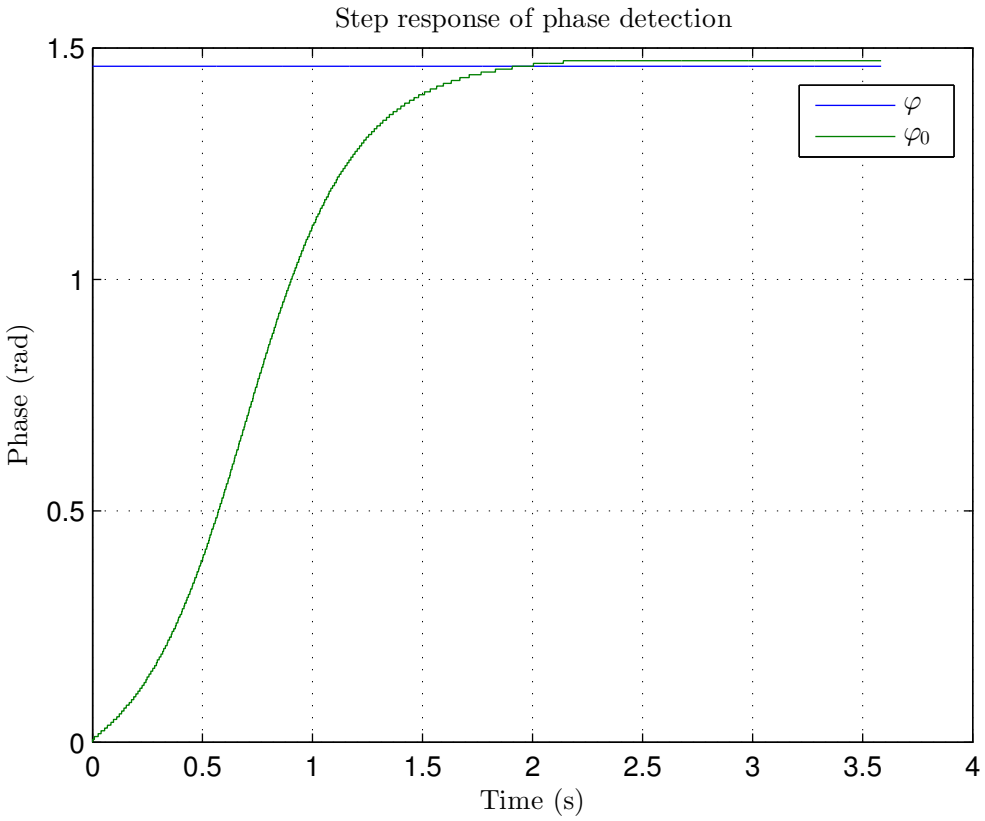


**Figure 8.6.:** Simulation of the algorithm inside the FPGA, acquiring data with *SignalTap II*. Time scale is approximate.

# 9 Accelerometer Noise Budget

The analytical form of accelerometer SNR has been presented in equation 6.10 and shows two main sources of noise in the accelerometer: the contributions come from the sensors and from the actuators. A third contribution is the process noise, that turns out to be negligible.

In this chapter the main contributes of this curve are analyzed and, eventually, compared with the noise budget of the accelerometer with the analog control.

## 9.1. Process Noise

In a mechanical oscillator subject to a viscous damping, thermal noise act as a noise in force with power spectral density

$$\bar{f}_n^2 = \frac{4kTm\omega_0}{Q}$$

(see Appendix B for details). Of course the $Q$-value to be used is the open-loop one ($Q \sim 200$), because the $Q = 0.5$ induced by the feedback doesn't correspond to a real loss of energy for friction (we could define it "cold friction"). This force acts like the feedback force, passing through the transfer function 6.8.

For our pendulum, at low frequencies the equivalent noise in acceleration is

$$S_{thermal}\left(\omega \ll \omega_0\right) = \left|6.5 \times 10^{-11} \frac{\mathrm{m/s^2}}{\sqrt{\mathrm{Hz}}}\right|^2$$

and then decreases as $\omega^{-4}$.

## 9.2. Sensing Noise

### 9.2.1. Noise on Primary Coil

Displacement sensors are LVDT. A 50 kHz sine wave signal is generated by FPGA using the 10-bits digital synthesizer presented in the previous section. The numerical noise is negligible, and in case can be easily reduced by increasing the number of bits. This carrier wave is sent by a DAC to the primary coil. At first sight DAC noise is negligible, because if the distances between coils are identical, it induces the same effects on each secondary coil, that are mutually canceled. However, if there is an offset in the position of secondary coils, that can occur for example when accelerometer is subject to a tilt, then this cancellation doesn't occur anymore and problems can arise.

Quantitatively, the mutual inductance $M$ between primary coil and a secondary coil satisfies the following relation (in Laplace transform) about the voltage on secondary coil

$$N_s s\Phi = M s I_p + L_s s I_s$$

where $L_p$ and $L_s$ are inductance of primary and secondary coils, respectively. The last term is zero in open-circuit configuration. Thus

$$\begin{aligned} M &= N_s \frac{\Phi}{I_p} \\ &= N_s N_p \frac{\Phi}{N_p I_p} \\ &= N_s N_p \mathcal{P} \end{aligned}$$

where $\mathcal{P}$ is the magnetic permeance through secondary coil, and its value at $z = 6\,\text{mm}$ is $\mathcal{P}_1 = 2.9 \times 10^{-8}\,\text{Wb}\,\text{A}^{-1}$ (it comes from the integral of Fig. 8.1). The coupling coefficient $k_{ps}$ (such that $|k_{ps}| \leq 1$) can be defined as

$$k_{ps} = \frac{\sqrt{L_s L_p}}{M}$$

In the accelerometer, being $L_p = 0.13\,\text{mH}$ and $L_s = 12.4\,\text{mH}$,[37] $k_{ps}$ is found to be

$$\begin{aligned} k_{ps} &= \frac{N_s N_p \mathcal{P}}{\sqrt{L_p L_s}} \\ &= 0.42 \end{aligned}$$

For comparison, the coupling coefficient between secondary coils is $k_{ss} \sim 0.1$, reasonably lower due to the greater distance between coils and their smaller dimensions. [37]

The first derivative of $k_{ps}$ with respect to $z$ can be found as

$$\begin{aligned}\frac{\partial k_{ps}}{\partial z} &= \frac{N_p N_s}{\sqrt{L_p L_s}} \frac{\partial \mathcal{P}}{\partial z} \\ &= 30.8\,\mathrm{m}^{-1}\end{aligned}$$

at $z = 6\,\mathrm{mm}$. Of course, a displacement induces opposite variation of $k_{ps}$ on each secondary coil. Using the circuit diagram of the board, a Spice simulation has been used to calculate the noise induced at the output of secondary coils, generated by a unitary white noise on the primary coil. In the range $|z - z_1| < 10\,\mu\mathrm{m}$, the PSD of noise induced on secondary coils by a noise on primary coil is proportional to the PSD of noise on primary coil and to the distances between them:

$$\sqrt{\frac{S_s}{S_p}} = 38 \times 10^{-5} \frac{\mathrm{V}}{\sqrt{\mathrm{Hz}}} (\mu\mathrm{m})^{-1} \left(\frac{\mathrm{V}}{\sqrt{\mathrm{Hz}}}\right)^{-1}$$

In our case, the primary coil noise is mostly $1/f$ noise, caused by instability of DAC AD1955 reference voltage at low frequencies: it modulates the amplitude of the 50 kHz carrier wave, producing effects also at high frequencies. According to a direct measurement of this noise, presented in Fig. 9.1, at 1 Hz it has $3\frac{\mu\mathrm{V}}{\sqrt{\mathrm{Hz}}}$. This means that, for $|z - z_1| > 7\,\mu\mathrm{m}$, this effect induces more than $5\frac{\mathrm{nV}}{\sqrt{\mathrm{Hz}}}$ on the secondary coils. As we'll see later, this would dominate on all the other sources of noise.

This is very important, as could dramatically worsen SNR if not properly kept under control. For example, tilting the sensor with an angle $\alpha = x \cdot \omega_0^2/g = 0.4\,\mathrm{mrad}$ we could obtain such a displacement. However it is more likely for this to occur due to the composite structure of the inverted pendulum of the accelerometer. To prevent this, we can use an inbuilt stepper motor, that can adjust the position of the mass within $\sim 7\,\mu\mathrm{m}$ from the center at the beginning of the measurement. For extra precision, we can also think to apply a DC feedback force.

This noise has never been taken into account until now in Virgo. Even if the old PID controller worked setting error signal to zero (i.e. keeping the mass as close as possible to the electrical center of LVDT), an electrical offset in the amplifiers could let to a mechanical offset in the closed loop system. Looking at the features of the components of the analog controller, an optimistic estimation suggests that this offset introduced a DC displacement $< 1\,\mu\mathrm{m}$ on the pendulum.

### 9.2.2. Noise on Secondary Coils

Secondary coils (see Fig. 9.2) have each one resistance of $210\,\Omega$, closed on a $100\,\Omega$ trimmer that balances possible asymmetries on the two branches. [37] The total resistance turns out to be about $130\,\Omega$: using $\bar{v_n^2} = 4kTR$ (see sec. B.2) it correspond

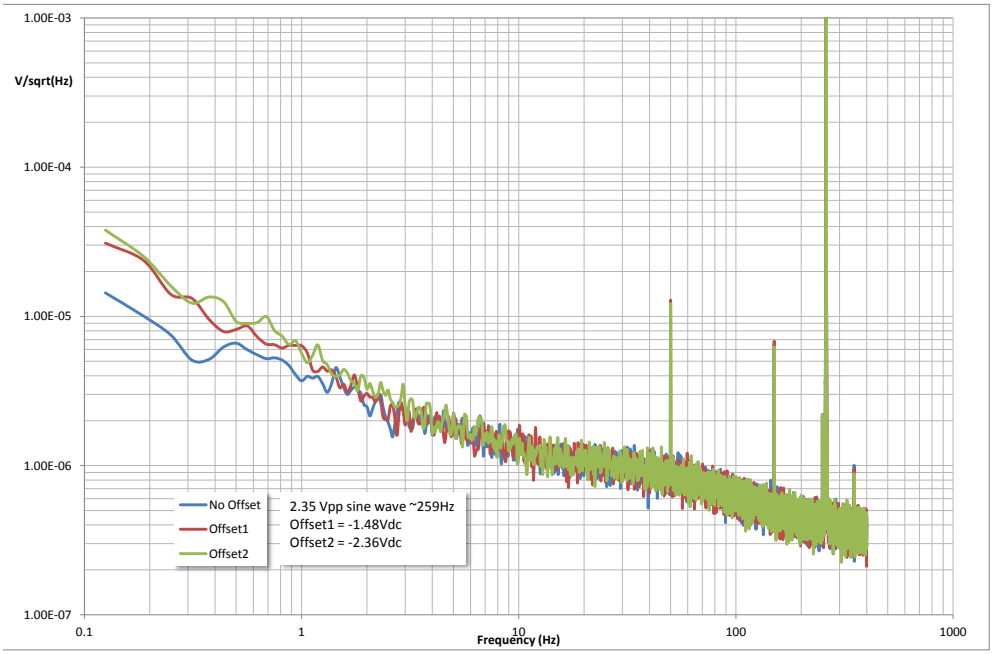


**Figure 9.1.:** Square root of power spectral density of AD1955 noise at low frequencies, in its full dynamic range $-5\,\mathrm{V} \div 5\,\mathrm{V}$, measured by Virgo Pisa group. These kind of converters are audio devices, and producers usually don't provide their noise in the infrasound band. The $1/f$ nature of this noise is clearly visible and the the curve can be approximated by $4 \times 10^{-6} \sqrt{\frac{1\,\mathrm{Hz}}{f}} \frac{\mathrm{V}}{\sqrt{\mathrm{Hz}}}$.

to $1.4 \frac{\mathrm{nV}}{\sqrt{\mathrm{Hz}}}$. An op-amp, with $1 \frac{\mathrm{nV}}{\sqrt{\mathrm{Hz}}}$ of noise in input, amplifies this signal by a factor $\sim 80$. Then the ADC adds $\sim 20 \frac{\mathrm{nV}}{\sqrt{\mathrm{Hz}}}$ (at 6 V peak to peak in input), corresponding to $0.25 \frac{\mathrm{nV}}{\sqrt{\mathrm{Hz}}}$ before the amplification. Finally the demodulation of the signal performed by FPGA introduces a negligible numerical noise. Using the sum of squares,

$$\sqrt{1.4^2 + 1^2 + 0.25^2} \frac{\mathrm{nV}}{\sqrt{\mathrm{Hz}}} = 1.7 \frac{\mathrm{nV}}{\sqrt{\mathrm{Hz}}} \tag{9.1}$$

the noise in sensing results to be white in voltage and dominated by the thermal noise of the secondary coils. This is desirable, being the only contribute that cannot be further reduced, and that does not depend on the electronics. According to 8.6, the noise 9.1 in voltage corresponds to $2.8 \times 10^{-12} \frac{\mathrm{m}}{\sqrt{\mathrm{Hz}}}$ in displacement. In turn, the displacement is proportional to the acceleration for $\omega \ll \omega_0$, with proportionality constant $\omega_0^2$ (see 6.6): in this bandwidth the noise is equivalent to

$$S_{sensing}\left(\omega \ll \omega_0\right) = \left| 1.1 \times 10^{-9} \frac{\mathrm{m/s^2}}{\sqrt{\mathrm{Hz}}} \right|^2 \tag{9.2}$$

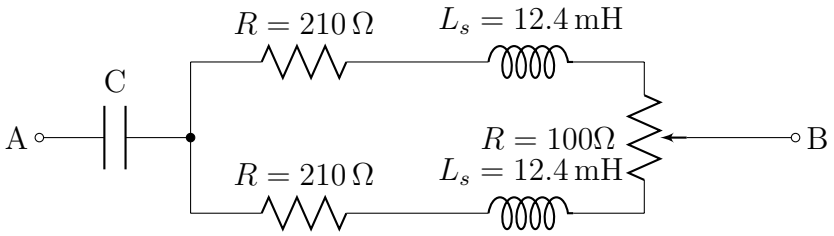


**Figure 9.2.:** Circuit diagram of secondary coils. The two ends A and B are read by a differential amplifier.

For higher frequency it grows as $\omega^4$, in as much as it is amplified by the digital shaping filter $T_{shaping}(s)$ 6.18, and its PSD is provided by

$$S_{sensing}(\omega) = |T_{shaping}(i\omega)|^2 S_{sensing}(\omega \ll \omega_0)$$

Even if $T_{shaping}$ is a digital filter, for this purpose we can use the continuous-time equivalent filter from which it has been extracted through bilinear transformation.

## 9.3. Acting Noise

A feedback force inevitably introduces noise in the system, because it involves noisy components and uncertainties. The basic idea is to calculate first the PSD of the feedback force acting in various environmental conditions, and then to see how much noise it introduces back into the system as equivalent seismic noise.

The closed loop transfer function $X_0 \to F$ is

$$T(s) = \frac{F}{X_0} = \frac{ms^2}{1 + \frac{s^2 + \frac{\omega_0}{Q}s + \omega_0^2}{H(s)}} \tag{9.3}$$

With critical damping, from equations 6.13 and 9.3, the closed loop transfer function $X_0 \to F$ becomes

$$T = -\frac{\Gamma s^3}{s^2 + 2\omega_0 s + \omega_0^2}$$

so that a seismic noise PSD $S_{x_0}(\omega)$ induces a feedback force PSD

$$S_f(\omega) = |T(i\omega)|^2 S_{x_0}(\omega) \tag{9.4}$$

It is insidious to estimate $S_{x_0}(\omega)$ as it depends on the environmental conditions. In equation 5.1 I have presented an estimation of the seismic noise PSD at ground

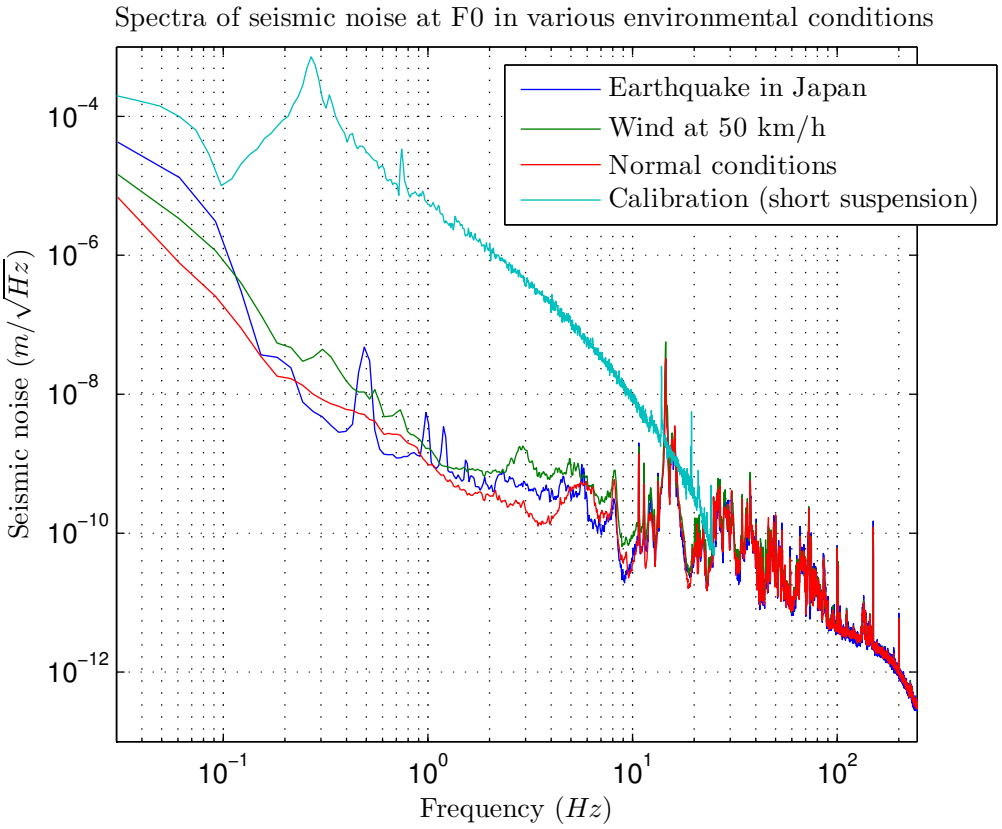


**Figure 9.3.:** Square root of seismic noise PSD $\sqrt{S_{x_0}}$ expressed in $\frac{\mathrm{m}}{\sqrt{\mathrm{Hz}}}$, measured in various environmental conditions at the Superattenuator top stage. All of them are measured during the last Virgo run in August 2011, except for the "calibration" spectrum that has been measured during a user handled calibration of the suspension control in 2014. More information in Tab. 9.1.

level. Actually, at the top of the Superattenuators this noise is filtered by the three-leg inverted pendulum. In Fig. 9.3 there are some spectra of the seismic noise, that have been measured, in several environmental conditions, by Virgo horizontal accelerometers placed on the top stage. It is easy to see that the spectrum at frequencies $< 10\,\mathrm{Hz}$ strongly depends on the weather and can dramatically increase with strong wind or if, for example, a remote earthquake occurs. Nevertheless, the strongest signal on the accelerometers is measured when a technician is estimating coils-to-sensors transfer functions, to calibrate the parameters for the top stage controller: he sends white noise to the coils, with the Superattenuator free to move due to the digital controller turned off. The RMS of the acceleration in the four cases of Fig. 9.3 are presented in Tab. 9.1.

With one of these spectra, it is possible to get the variance of the force, integrating

| | Seismic noise $\ddot{x}_0$ (mm/s$^2$) | Displacement $x - x_0$ (nm) | Force $f$ (µN) |
|---|---|---|---|
| Normal conditions | 0.10 | 10 | 17 |
| Wind at 50 km/h (8/8/2011) | 0.16 | 17 | 30 |
| Earthquake in Japan (8/19/2011) | 0.11 | 11 | 19 |
| Calibration | 0.59 | 1100 | 140 |

**Table 9.1.:** Root mean square of some quantities in an accelerometer working with critical damping, measured in various environmental conditions at the Superattenuator top stage. I present only two significant figures, the essential to appreciate some differences. However these values are affected by a moderate variability.

the PSD in $\omega$

$$\sigma_f^2 = \frac{1}{2\pi}\int_0^\infty S_f(\omega)\, d\omega$$

Values of this integral in the debated environmental conditions are shown in Tab. 9.1, and their relative spectra $S_f$ are in Fig. 9.4.

This force is done on the mass through a coil actuator, driven with internal resistance $R_I = 3.2\,\mathrm{k}\Omega$ and read on a external resistance $R_D$ (see Fig. 9.5). The efficiency is [34]

$$\epsilon = 30\,\mathrm{N/A} = \frac{30\,\Omega}{R_D}\mathrm{N/V} \tag{9.5}$$

if $R_D \gg R_I$.

An AD1955 DAC soldered on the new board provides the voltage to drive the actuator coil: according to Fig. 9.1, its noise can be approximated as

$$4\times 10^{-6}\sqrt{\frac{1\,\mathrm{Hz}}{f}}\frac{\mathrm{V}}{\sqrt{\mathrm{Hz}}} \tag{9.6}$$

in its full dynamic range $-5\,\mathrm{V} \div 5\,\mathrm{V}$. As it is going to be proved further down, this is the main noise source in the acting system, and we would like to keep this noise smaller than the sensing noise 9.2. This can be done scaling the arbitrary resistor $R_D$ placed at output of DAC. Of course, the smaller value of $R_D$, the maximum will be the force applicable. On the other hand, reducing $R_D$ we increase the effect of the DAC noise on the actuator and then on the system.

Let's say that we want to keep acting noise at the level of the sensing noise at 1 Hz, where DAC noise is $\sim 4\times 10^{-6}\frac{\mathrm{V}}{\sqrt{\mathrm{Hz}}}$. Indeed, looking at Fig. 9.4, most of the force is done in the frequency band between 0.1 Hz and 50 Hz. So, a value of

$$S_{acting}(1\,\mathrm{Hz}) = \left|1.5\times 10^{-9}\frac{\mathrm{m/s^2}}{\sqrt{\mathrm{Hz}}}\right|^2 \tag{9.7}$$

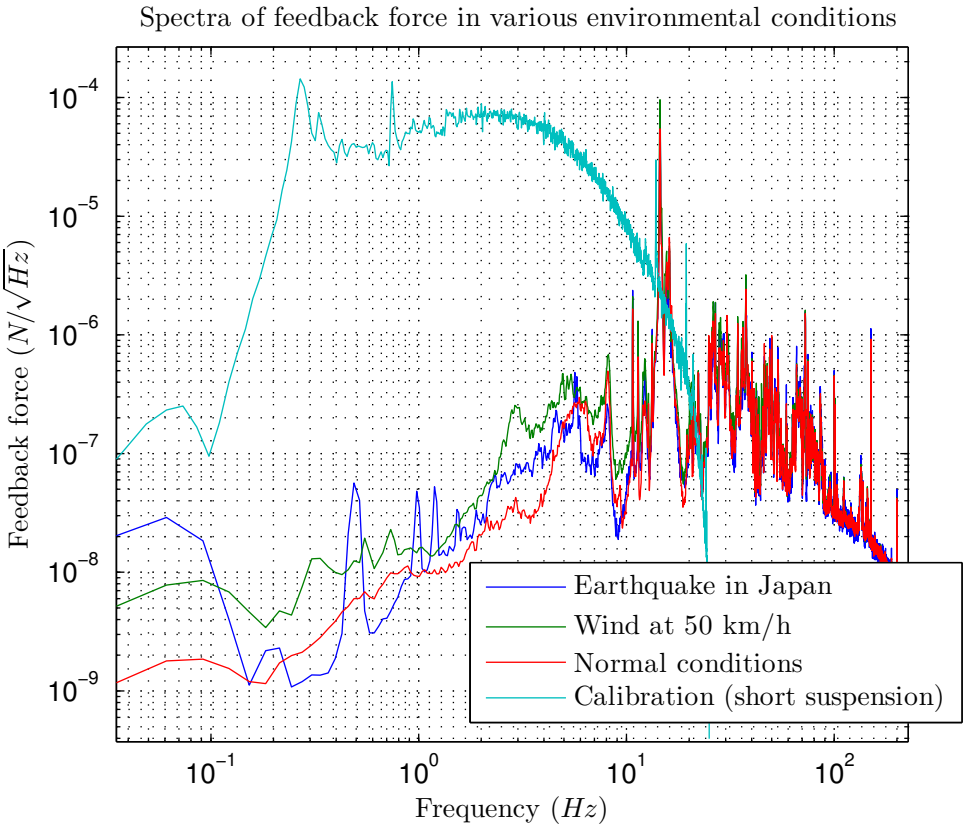


**Figure 9.4.:** Square root of feedback force PSD $\sqrt{S_f}$ expressed in $\frac{\mathrm{N}}{\sqrt{\mathrm{Hz}}}$, simulated in various environmental conditions at the Superattenuator top stage, with critical damping.

would satisfy that condition in the bandwidth above 1 Hz, with an even better improvement for $\omega \gg \omega_0$.

Of course DAC noise produces an equivalent noise in acceleration, being the voltage proportional to the force, and the force proportional to the acceleration. This noise in acceleration 9.7, relative to mass $m = 439\,\mathrm{g}$, is equivalent to a noise in force of $6.5 \times 10^{-10} \frac{\mathrm{N}}{\sqrt{\mathrm{Hz}}}$ and, using the efficiency 9.5, to a noise in voltage of $R_D \cdot 22 \frac{\mathrm{pA}}{\sqrt{\mathrm{Hz}}}$. Comparing this with 9.6, we find that

$$R_D = 200\,\mathrm{k}\Omega$$

is the minimum value of $R_D$ that keep the effect of the DAC noise $S_{acting}$ well below $S_{sensing}$. With this choice, the coil is able to apply a force as large as

$$F_{max} = \frac{5\,\mathrm{V} \cdot 30\,\mathrm{N/A}}{200\,\mathrm{k}\Omega} = 750\,\mu\mathrm{N}$$

This value is sufficient to perform the critical damping because, according to Tab. 9.1, it is 5 times grater than the expected RMS during calibration.

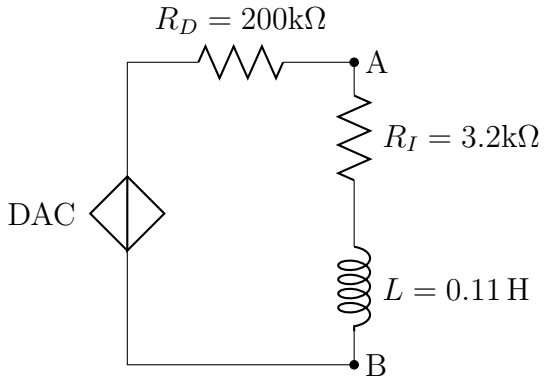


**Figure 9.5.:** Voltage divider used to reduce the effects of DAC noise to the coil actuator, whose internal resistance is $R_I = 3.2\,\text{k}\Omega$ [37] and the inductance $L = 0.11\,\text{H}$. To properly scale the DAC voltage we need a resistance $R_D = 200\,\text{k}\Omega$.

Finally I show as the thermal noise of the components in the actuator does not provide a significant contribution to the noise budget. The schematic diagram is shown in Fig. 9.5: being the coil impedance negligible at the working frequency (0.11 H at $\sim 1\,\text{Hz}$ is equivalent less than $1\,\Omega$), the current noise flowing in the circuit (and thus generating a force in the coil actuator) is the sum of DAC and resistor noises:

$$i_n^2 = \frac{v_{n,R_D}^2 + v_{n,R_I}^2 + v_{n,DAC}^2}{(R_D + R_I)^2}$$

where, at $T = 300\,\text{K}$,

$$\begin{aligned}\sqrt{v_{n,R_D}^2} &= \sqrt{4kTR_D} = 57\frac{\text{nV}}{\sqrt{\text{Hz}}} \\ \sqrt{v_{n,R_I}^2} &= \sqrt{4kTR_I} = 7.3\frac{\text{nV}}{\sqrt{\text{Hz}}}\end{aligned}$$

This clearly shows that such a voltage divider does not introduce significant additional noise to the system, and that the main contribute comes from the DAC.

## 9.4. Total Noise Budget

The noise budget curve of the accelerometer, with the new controller, is presented in Fig. 9.6. Now the statement *"the signal-to-noise ratio cannot be improved using a feedback control"* made at the beginning of the thesis should become clear to the reader: in the open-loop configuration, the red line would disappear from the noise

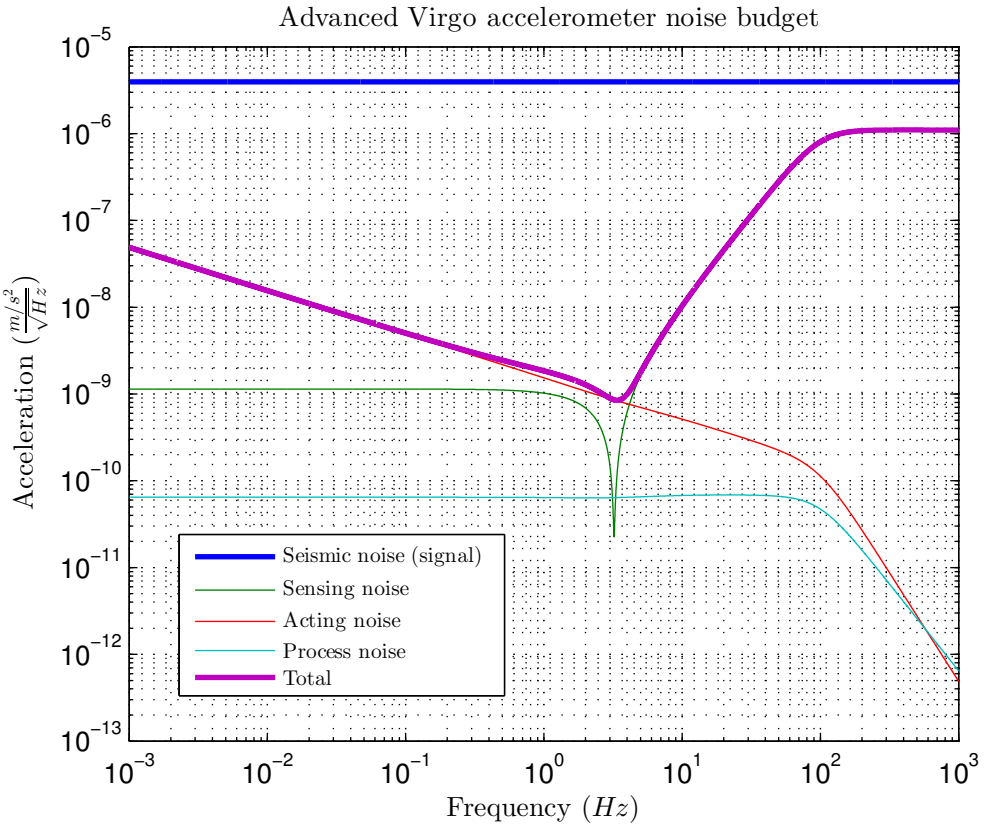


**Figure 9.6.:** Advanced Virgo accelerometer noise budget

budget, and the only significant contribute would be represented by the thermal noise of LVDT (the green line). The introduction of a control system is a compromise between the sensitivity and the usability of the sensor.

A significant improvement could come from the use of a better DAC. Our group is currently investigating the possibility to replace the AD1955 with less noisy devices: it is likely that we are able to reduce of almost two order of magnitude the the acting noise at 1 Hz in the final version of the board. This would imply that the main contribute of the noise budget at low frequencies will be the sensing noise indeed, and also would make the 7 µm-range, presented in sec. 9.2.1, wider.

### 9.4.1. Comparison with Virgo/Virgo+ Analog Control

In Virgo and Virgo+, accelerometers had an analog controller with transfer function 6.12. Inserting it in the closed loop transfer function 9.3, and using 9.4 to get $S_f(\omega)$, the variance of the force in the analog circuit

$$\sigma_f^2 = \frac{1}{2\pi}\int_0^\infty S_f(\omega)\, d\omega$$

| | Critical damping (RMS) | | Analog PID (RMS) | |
|---|---|---|---|---|
| | $x - x_0$ (nm) | $f$ (µN) | $x - x_0$ (nm) | $f$ (µN) |
| Normal conditions | 10 | 17 | 2.6 | 40 |
| Wind at 50 km/h | 17 | 30 | 4.7 | 67 |
| Earthquake in Japan | 11 | 19 | 3.0 | 45 |
| Calibration | 1100 | 140 | 64 | 250 |

**Table 9.2.:** Comparison of RMS of feedback forces and average displacement

corresponded to the RMS values in sec. 9.4.1, where they are compared to the critical damping controller.

In Fig. 9.7 the Virgo/Virgo+ power spectral density of the force $S_f(\omega)$ is compared with the new one, when accelerometer is subject to white noise acceleration. With PID controller, force was proportional to the acceleration in the bandwidth (the voltage on the coil driver was taken as output, indeed). In the critical damping configuration, the feedback force in the same condition is lower everywhere: it is focused only around the resonance. This explain the values in sec. 9.4.1.

Finally, the noise budget of Virgo/Virgo+ accelerometer is presented in Fig. 9.8, compared with the noise of the new digital control. [34] The dominant noise at low frequencies was relative to the old ADC, with $1/f$ corner around 1 Hz. With the digital control, the $1/f$ noise of ADC is not a problem anymore, because they acquire directly the high frequency signal and don't introduce a significant contribute. On the other hand, the digital control implies the use of a DAC to apply the feedback force: as seen in the previous sections, the $1/f$ noise of AD1955 is the main contribute to the noise budget. However, as explained in the previous section, this could be no longer true with a better DAC.

Then, as with the critical damping control, the thermal noise of secondary coils became dominant beyond 10 Hz: of course it is an intrinsic property of the system, independent of the controller used.

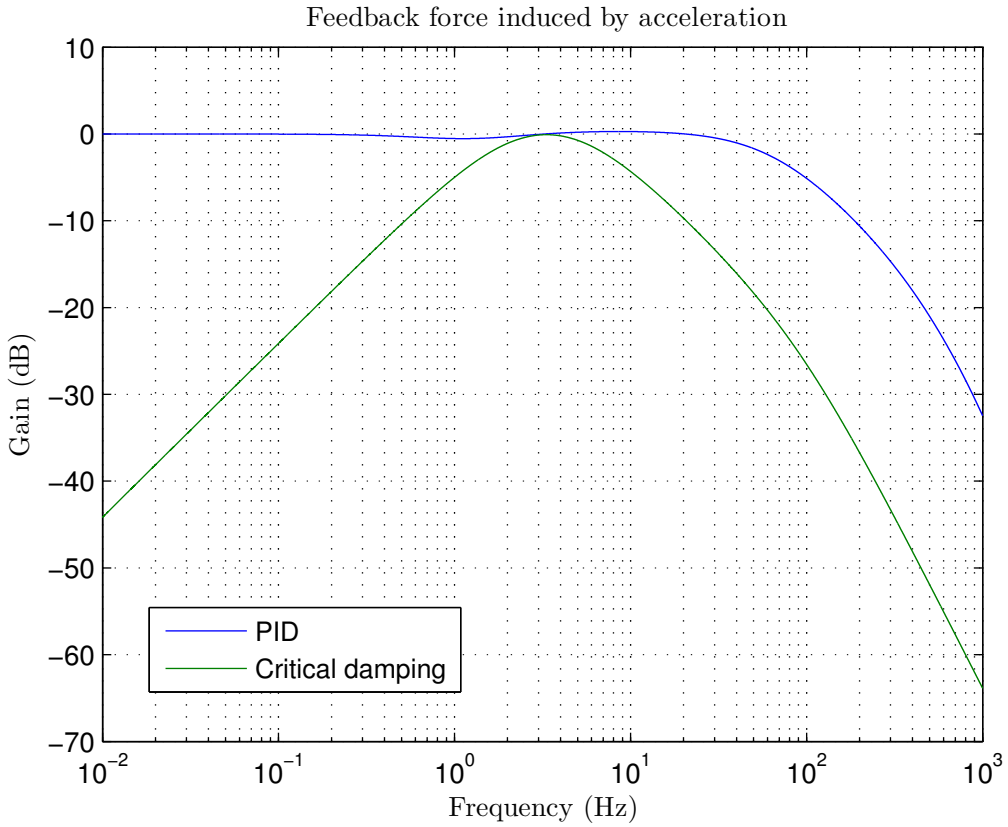


**Figure 9.7.:** Feedback force induced by white noise in acceleration.

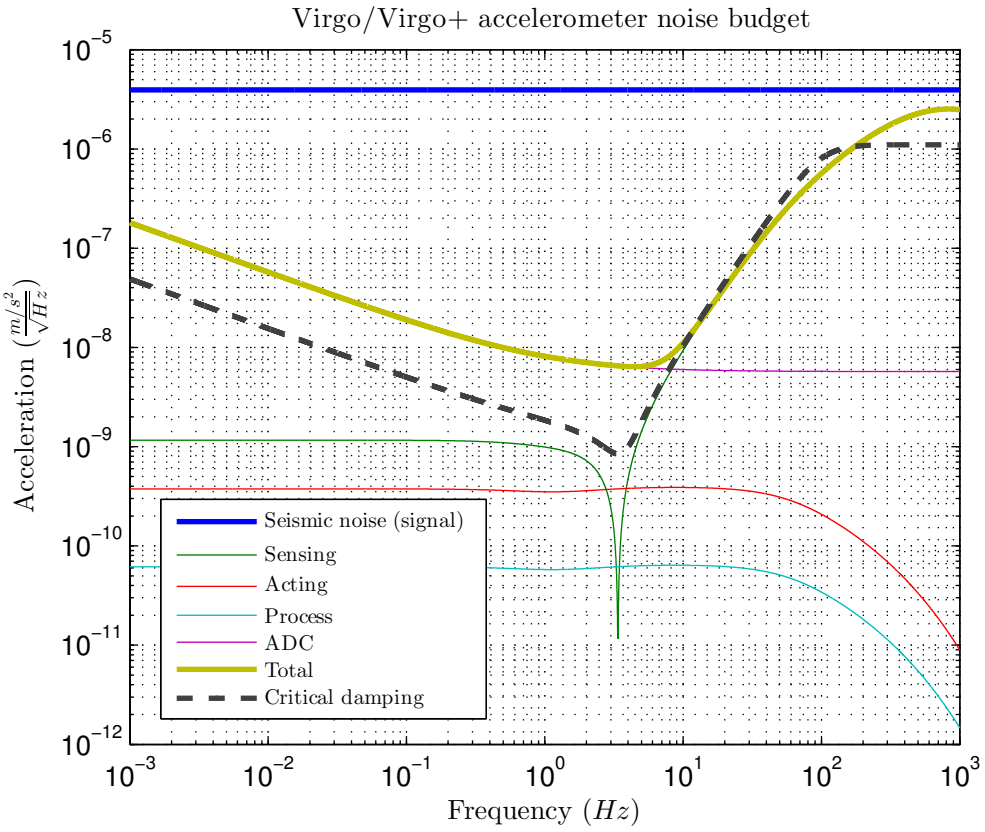


**Figure 9.8.:** Virgo/Virgo+ accelerometer noise budget, compared to the noise budget with critical damping. [34]

# 10 Conclusions

It is less than two years from the beginning of the data acquisition, and the project Advanced Virgo is going to make operative the interferometer with a never before achieved sensitivity. To be ready to detect gravitational signals from many potential sources around our galaxy, every single part of Virgo is undergoing several upgrades.

In this thesis I have presented a description as exhaustive as possible of horizontal accelerometers, currently used over the Superattenuators to measure the seismic noise. While the mechanics of the sensor will remain the same, the electronics that controls accelerometers is completely rebuilt. In particular, a dedicated board, hosting their analog controller in Virgo, disappears: the DSP of the new electronics of the Superattenuator inertial control is enough powerful to take care also of the control of accelerometers.

I have designed a digital control system for the horizontal accelerometers. It makes possible to reduce by a factor 2 the external force applied to the pendulum for the feedback control, with respect to the old controller used in Virgo and Virgo+. This, together with the better performances of the new ADC and DAC, lets us to increase of almost one order of magnitude the sensitivity of the sensors in the frequency band from DC to 3 Hz. Furthermore, this improvement could be even larger if current digital-to-analog converters are replaced with better ones. Because of the great importance of such a thing, our group is currently investigating this possibility. In the future, the critical damping control have to be extended for vertical accelerometers.

Using the noise levels of the new components, I have also defined a limit to the dynamic range of the position of the pendulum inside the accelerometer: with the current DAC, it must be kept within $\sim 7\,\mu$m from the center, in order to limit the effects of the noise on primary coil of LVDT over the accelerometer sensitivity. Of course, this range would be wider using a better DAC.

Eventually, I have created an algorithm to synthesize sinusoidal waves with a DDS, and then to demodulate the signal from secondary coils of LVDT. Using a digital

closed loop system, this algorithm measures the phase shift between reference wave and signal, and then adjusts itself in order to get the best signal-to-noise ratio from LVDT. This algorithm, implemented in FPGA, can be used not only for accelerometers, but of course also for the others LVDTs used in Superattenuator inertial control.

Furthermore, a purely digital control applied to accelerometers brings about a lot of other advantages. For example, the DDS realized with the FPGA let us to do without the commercial signal generators, that have been used so far in Virgo, one for each Superattenuator, to drive LVDT inside the accelerometers. In addition to an obvious savings opportunity relative to their maintenance, we can also suppose to send signals at slightly different frequencies to the various LVDT, in order to avoid possible electromagnetic interferences that could arise between sensors.

In conclusion, the potentialities of the new electronics are enormous. Besides the inertial control of Superattenuators, the computational resources of DSP and FPGA are sufficient to host many new features, compared to what it was in Virgo and Virgo+.

# A

# Mathematical Tools

## A.1. Laplace Transform

Laplace transform is a linear operator of a function $f(t)$ with a real argument $t$ ($t \geq 0$) that transforms $f(t)$ to a function $F(s)$ with complex argument $s$, given by the integral

$$\mathcal{L}[f(t)](s) = F(s) = \int_{0^+}^{\infty} f(\tau)\, e^{-s\tau} d\tau \tag{A.1}$$

This transformation is bijective for the majority of practical uses.

### A.1.1. Inverse Laplace Transform

The inverse Laplace transform is

$$\mathcal{L}^{-1}[F(s)](t) = \frac{1}{2\pi i} \lim_{T\to\infty} \int_{\gamma-iT}^{\gamma+iT} F(s) e^{st} ds, \tag{A.2}$$

where the integration is done along the vertical line $Re(s) = \gamma$ in the complex plane such that $\gamma$ is greater than the real part of all singularities of $F(s)$.

The set of values for which $F(s)$ converges is known as the region of convergence.

### A.1.2. Used Properties

Table of the used properties:

| | Time domain | Frequency domain |
|---|---|---|
| Linearity | $af(t)+bg(t)$ | $aF(s)+bG(s)$ |
| Differentiation | $f'(t)$ | $sF(s)-f(0)$ |
| Second differentiation | $f''(t)$ | $s^2F(s)-sf(0)-f'(0)$ |
| General differentiation | $f^{(n)}(t)$ | $s^nF(s)-\sum_{k=1}^{n}s^{k-1}f^{(n-k)}(0)$ |
| Integration | $\int_0^t f(t)\,d\tau$ | $\frac{1}{s}F(s)$ |
| Convolution | $(f*g)(t)$ | $F(s)\cdot G(s)$ |
| Unit impulse | $\delta(t)$ | 1 |
| Unit box | $r(t)=\begin{cases}a^{-1} & 0\le t\le a\\ 0 & elsewhere\end{cases}$ | $e^{sT}\frac{1-e^{sT}}{sT}$ |

## A.2. Z-Transform

In continuous-time system theory the Laplace transform can be considered as a generalization of the Fourier transform. In a similar manner the Fourier transform for discrete-time signals and systems of a sequence $x(n)$

$$X\left(e^{i\omega}\right)=\sum_{n=-\infty}^{+\infty}x(n)\,e^{-i\omega n} \tag{A.3}$$

can be generalized in what is commonly referred to as the *Z-transform*. The Z-transform $X(z)$ of a sequence $x(n)$ is defined as

$$\mathcal{Z}\left[x(n)\right](z)=X(z)=\sum_{n=-\infty}^{+\infty}x(n)\,z^{-n} \tag{A.4}$$

where $z$ is a complex variable. Furthermore, by expressing $z$ in polar form as $z=re^{i\omega}$, equation A.4 becomes

$$X\left(re^{i\omega}\right)=\sum_{n=-\infty}^{+\infty}x(n)\,r^{-n}e^{-i\omega n}$$

Thus, according to equation A.3, the Z-transform of $x(n)$ can be interpreted as the Fourier transform of $x(n)\,r^{-n}$.

Sometimes the Z-transform defined in equation A.4 is called *two-sided Z-transform*, because there is also a similar functional

$$\mathcal{Z}_I\left[x(n)\right](z)=X_I(z)=\sum_{n=0}^{+\infty}x(n)\,z^{-n} \tag{A.5}$$

that is defined *one-sided Z-transform*. Clearly, if $x(n)=0$ for $n<0$ the one-sided and two-sided transforms are equivalent.

### A.2.1. Region of Convergence

For any given sequence, the set of values of $z$ for which the Z-transform converges is called the *region of convergence*. Because of the multiplication of the sequence by a real exponential $r^{-n}$, it is possible for the Z-transform to converge even if the Fourier transform does not. Usually, the region of convergence, in the $z$-plane, is an annular region centered in the origin that can be as large as infinity.

### A.2.2. Inverse Z-transform

There is also an inverse Z-transform, defined as

$$\mathcal{Z}^{-1}\left[X\left(z\right)\right]\left(n\right) = x\left(n\right) = \frac{1}{2\pi i}\oint_C X\left(z\right) z^{n-1} dz \tag{A.6}$$

where $C$ is a counterclockwise closed contour in the region of convergence of $X\left(z\right)$ and encircling the origin of the $z$-plane.

### A.2.3. Convolution of Sequences

The convolution theorem of Laplace transform seen in equations 3.4 exists also for the $z$-transform: if $w\left(n\right)$ is the convolution of the two sequences $x\left(n\right)$ and $y\left(n\right)$,

$$w\left(n\right) = \sum_{k=-\infty}^{+\infty} x\left(k\right) y\left(n-k\right)$$

then the z transform of $w\left(n\right)$ is the product of the Z-transform of $x\left(n\right)$ and $y\left(n\right)$

$$W\left(z\right) = X\left(z\right) \cdot Y\left(z\right)$$

### A.2.4. Used Properties

Table of the used properties:

| | Time domain | Z-domain |
|---|---|---|
| Linearity | $a_1 x_1\left(n\right) + a_2 x_2\left(n\right)$ | $a_1 X_1\left(z\right) + a_2 X_2\left(z\right)$ |
| Time shifting | $x\left(n-k\right)$ | $z^{-k} X\left(z\right)$ |
| Convolution | $x_1\left(n\right) * x_2\left(n\right)$ | $X_1\left(z\right) \cdot X_2\left(z\right)$ |
| Unit sample | $\delta\left(n\right)$ | 1 |

## A.3. Bilinear Transformation

Suppose we have the following first order differential equation

$$a_1 y'(t) + a_0 y(t) = b_0 x(t) \tag{A.7}$$

where, obviously, $y'(t)$ is the time derivative of $y(t)$. Using a Laplace transform and assuming as initial condition $y(0^+) = 0$ we get

$$a_1 sY(s) + a_0 Y(S) = b_0 X(s)$$

from which we obtain the transfer function

$$H_a(s) = \frac{Y(s)}{X(s)} = \frac{b_0}{a_1 s + a_0} \tag{A.8}$$

Obviously we have

$$y(t) = \int_{t_0}^{t} y'(\tau) d\tau + y(t_0)$$

and, putting $t = nT$ and $t_0 = (n-1)T$ in this last equation ($f = 1/T$ is the sampling frequency), we get:

$$y(nT) = \int_{(n-1)T}^{nT} y'(\tau) d\tau + y((n-1)T)$$

Approximating the integral by the trapezoidal rule we obtain:

$$y(nT) \simeq y((n-1)T) + \frac{T}{2}[y'(nT) + y'((n-1)T)] \tag{A.9}$$

On the other hand we have from eq. A.7

$$y'(nT) = -\frac{a_0}{a_1} y(nT) + \frac{b_0}{a_1} x(nT)$$

putting this last equation into eq. A.9 we get

$$y_n - y_{n-1} \simeq \frac{T}{2}\left[-\frac{a_0}{a_1}(y_n + y_{n-1}) + \frac{b_0}{a_1}(x_n + x_{n-1})\right]$$

where we've written $y_n$ instead of $y(nT)$. Now, using the Z-transform and remembering that if $x_n \to X(z)$ then $x_{n-1} \to z^{-1}X(z)$, we obtain:

$$H(z) = \frac{Y(z)}{X(z)} = \frac{b_0}{a_1 \frac{2}{T}\frac{1-z^{-1}}{1+z^{-1}} s + a_0} \tag{A.10}$$

Comparing the analog transfer function A.8 with the discrete one in A.10, we see that we can obtain the latter from the former simply by substituting the $s$ Laplace's variable with the following expression:

$$s \to \frac{2}{T}\frac{1-z^{-1}}{1+z^{-1}} \tag{A.11}$$

Obviously we can obtain an analog transfer function from a discrete one using the inverse transformation:

$$z \to \frac{1+T/2\ s}{1-T/2\ s} \tag{A.12}$$

The transformation A.11 is called **bilinear transformation**. We obtain it in the case of a first order linear differential equation. Nevertheless its validity is more general, because an $N^{th}$-order linear differential equation can be written as a set of $N$ first order linear differential equations.

# B

# Technical Tools

## B.1. Mechanical Impedances

In the electrical world, the impedance is the measure of the opposition that a circuit presents to a current when a voltage is applied, ans is represented as a complex quantity $Z_e$. Is defined as the complex ratio of the Laplace transforms of the voltage $V$ to the current $I$:

$$Z_e = \frac{V}{I} \tag{B.1}$$

Under the assumption that all initial conditions are zero, the characteristic differential equation of a series RLC circuit with applied an external voltage $V$ is

$$LsI + RI + C^{-1}\frac{1}{s}I = V \tag{B.2}$$

Similarly, the characteristic differential equation of a forced damped harmonic oscillator with null initial conditions is

$$ms^2X + \gamma sX + kX = F \tag{B.3}$$

It's easy to see that these two systems can be studied with the same mathematical tools if we associate the physical quantities as shown in table B.1.

It follows that we can define a *mechanical impedance* $Z_m$ as the ratio of the external force $F$ to the velocity of the system $v = sX$*:*

$$Z_m = \frac{F}{v} \tag{B.4}$$

This is a measure of how much a structure resists motion when subjected to a given force, and has the dimension of a damping coefficient. It's interesting to observe that the the product of $V$ and $I$, elements of equation X is dimensioned as a power, so as that of $F$ and $v$.

| Series RLC circuit | | | Damped oscillator | |
|---|---|---|---|---|
| I | current | $\Longleftrightarrow$ | $sX$ | velocity |
| $L$ | inductance | $\Longleftrightarrow$ | $m$ | mass |
| $R$ | resistance | $\Longleftrightarrow$ | $\gamma$ | damping coefficient |
| $C^{-1}$ | elastance | $\Longleftrightarrow$ | $k$ | spring constant |
| $V$ | voltage | $\Longleftrightarrow$ | $F$ | force |

**Table B.1.:** Associations of electrical quantities and mechanical quantities.

## B.2. Thermal Noise

The resistance is related to the thermal noise in a circuit. With no current applied, the voltage measured across the two ends of a circuit is not null, and its power spectral density is

$$\bar{v_n^2} = 4kTR \tag{B.5}$$

where $kT = 25.6\,\text{meV} = 4.11 \times 10^{-21}\,\text{J}$ at room temperature (298 K) of the circuit and $R$ is the real part of its impedance. This is usually referred as *Johnson–Nyquist noise*.

The same power spectral density can be extended to the mechanical world with the associations in table B.1. This means that a mechanical system, e.g. a damped harmonic oscillator, presents a noise in force whose power spectral density is

$$\bar{f_n^2} = 4kT\gamma \tag{B.6}$$

or, using $Q = \frac{m\omega_0}{\gamma}$,

$$\bar{f_n^2} = \frac{4kTm\omega_0}{Q} \tag{B.7}$$

# C Notes on Seismic Noise

## C.1. An Analytic Approach

Instead of using the measured values of seismic noise, we can use the spectrum 5.1, that allows a parametric solution:

$$S_{x_0}(f) \sim \left| A \cdot \left( \frac{1\,\mathrm{Hz}}{f} \right)^2 \frac{\mathrm{m}}{\sqrt{\mathrm{Hz}}} \right|^2$$

(where $A = 10^{-7}$). According to 9.4, this induce, in the critical damped system, a feedback force with power spectral density of

$$S_f(\omega) = |T(i\omega)|^2 S_{x_0}(\omega)$$

This becomes

$$\begin{aligned} S_f(\omega) &= \left| -\frac{\Gamma (i\omega)^3}{(i\omega)^2 + 2\omega_0 (i\omega) + \omega_0^2} \right|^2 \left( \frac{4\pi^2 A}{\omega^2} \right)^2 \\ &= \left( \frac{4\pi^2 \Gamma A \omega}{\omega^2 + \omega_0^2} \right)^2 \end{aligned}$$

With one of these spectra, it's possible to get the variance of the force, integrating the PSD in $\omega$

$$\begin{aligned} \sigma_f^2 &= \frac{1}{2\pi} \int_0^\infty S_f(\omega)\, d\omega \\ &= \frac{1}{2\pi} \int_0^\infty \left( \frac{4\pi^2 \Gamma A \omega}{\omega^2 + \omega_0^2} \right)^2 d\omega \\ &= \frac{(4\pi^2 \Gamma A)^2}{2\pi} \int_0^\infty \frac{\omega^2}{(\omega^2 + \omega_0^2)^2} d\omega \\ &= \frac{(4\pi^2 \Gamma A)^2}{2\pi} \frac{\pi}{4\omega_0} = \frac{2\pi^4 \Gamma^2 A^2}{\omega_0} \end{aligned}$$

Using the right values, this corresponds to a standard deviation

$$\sigma_f = 40\,\mu\text{N}$$

that is consistent with estimations presented in Tab. 9.1.

# Bibliography


[1] J. Abadie *et al.*, "Predictions for the Rates of Compact Binary Coalescences Observable by Ground-based Gravitational-wave Detectors," *Class.Quant.Grav.*, vol. 27, p. 173001, 2010.

[2] The Virgo Collaboration, "Advanced Virgo Technical Design Report," Tech. Rep. VIR–0128A–12, CNRS and INFN, Apr 2012.

[3] J. Beringer *et al.*, "Review of Particle Physics," *Phys.Rev.*, vol. D86, p. 010001, 2012.

[4] I. R. Kenyon, *General Relativity*. Oxford University Press, 1990.

[5] S. Weinberg, *Gravitation and cosmplogy: principles and applications of the general theory of relativity*. John Wiley & Sons, Inc., 1972.

[6] R. Feynman, R. Leighton, and M. Sands, *The Feynman Lectures on Physics - Mainly Electromagnetism and Matter*. Addison-Wesley Publishing Company, Inc., 1964.

[7] J. Weisberg, D. Nice, and J. Taylor, "Timing Measurements of the Relativistic Binary Pulsar PSR B1913+16," *Astrophys.J.*, vol. 722, pp. 1030–1034, 2010.

[8] P. Peters and J. Mathews, "Gravitational radiation from point masses in a Keplerian orbit," *Phys.Rev.*, vol. 131, pp. 435–439, 1963.

[9] P. Ade *et al.*, "BICEP2 I: Detection Of B-mode Polarization at Degree Angular Scales," 2014.

[10] K. S. Thorne, *Gravitational Radiation in "Three Hundred Years of Gravitation"*. Cambridge University Press, 1987.

[11] The LIGO Scientific Collaboration, "http://www.ligo.org/science/gw-sources.php," 2014.

[12] C. D. Ott, E. Abdikamalov, P. Mösta, R. Haas, S. Drasco, *et al.*, "General-Relativistic Simulations of Three-Dimensional Core-Collapse Supernovae," *Astrophys.J.*, vol. 768, p. 115, 2013.

[13] J. Abadie *et al.*, "Search for gravitational waves associated with gamma-ray bursts during LIGO science run 6 and Virgo science runs 2 and 3," *Astrophys.J.*, vol. 760, p. 12, 2012.

[14] J. Aasi, J. Abadie, B. Abbott, R. Abbott, T. Abbott, *et al.*, "Gravitational waves from known pulsars: results from the initial detector era," 2013.

[15] B. Allen, "The stochastic gravity-wave background: sources and detection," in *Relativistic Gravitation and Gravitational Radiation, Proceedings of the Les Houches School of Physics, held in Les Houches, Haute Savoie*, vol. 26, pp. 373–418, 1997.

[16] T. Regimbau, "The astrophysical gravitational wave stochastic background," *Res.Astron.Astrophys.*, vol. 11, pp. 369–390, 2011.

[17] B. Abbott *et al.*, "An Upper Limit on the Stochastic Gravitational-Wave Background of Cosmological Origin," *Nature*, vol. 460, p. 990, 2009.

[18] G. Diambrini-Palazzi, "Gravitational radiation produced by high-energy accelerators and high power lasers," *Part.Accel.*, vol. 33, pp. 195–205, 1990.

[19] P. Saulson, *Fundamentals of Interferometric Gravitational Wave Detectors*. World Scientific Publishing Company, Incorporated, 1994.

[20] The AURIGA collaboration, "AURIGA website," May 2009.

[21] V. Boschi, *Modeling and Simulation of Seismic Attenuation Systems for Gravitational Wave Interferometers*. PhD thesis, Università di Pisa, 2010.

[22] K. Ogata, *Modern Control Engineering*. Instrumentation and controls series, Prentice Hall, 2010.

[23] J. Maciejowski, *Multivariable feedback design*. Electronic systems engineering series, Addison-Wesley, 1989.

[24] A. V. Oppenheim and R. Schafer, *Digital signal processing*. Prentice-Hall international editions, Prentice-Hall, 1975.

[25] M. Punturo, "Advanced Virgo sensitivity curve study." VIR-0073D-12, Nov 2012.

[26] R. Del Fabbro, "Magnetic antispring." VIR-NOT-PIS-1380-71, Dec 1993.

[27] SAT group, "Strategy for adv superattenuators." VIR-0098A-08, October 2008.

[28] A. Gennai, "Technical Requirements For a HRG Sensor Prototype." VIR-0661B-11, Sep 2012.

[29] V. Boschi, "Gyroscope Characterization Study." VIR-0032B-14, Feb 2014.

[30] Texas Instruments, *TMS320C6678 - Multicore Fixed and Floating-Point Digital Signal Processor (Rev. E)*. Texas Instruments, SPRS691E—November 2010—Revised March 2014 ed., Mar 2014.

[31] G. Losurdo, G. Calamai, E. Cuoco, L. Fabbroni, G. Guidi, M. Mazzoni, R. Stanga, F. Vetrano, L. Holloway, D. Passuello, *et al.*, "Inertial control of the mirror suspensions of the VIRGO interferometer for gravitational wave detection," *Review of Scientific Instruments*, vol. 72, no. 9, pp. 3653–3661, 2001.

[32] T. Zelenova, "Horizontal Accelerometer." VIR-0775A-09, 2009.

[33] Bruel & Kjaer, *LAN-XI Data Acquisition Hardware for PULSE$^{TM}$ and Test for I-deas$^{TM}$*. Bruel & Kjaer, bp 2215 – 15 ed., 08 2009.

[34] M. Passuello, "Accelerometer Noise Budget." 2009.

[35] R. Poley, "Signal Conditioning an LVDT Using a TMS320F2812 DSP," Application Report SPRA946, Texas Instruments, August 2003.

[36] M. Kumm, "DDS Synthesizer," 2008.

[37] N. Grilli, "Measurements on Accelerometers Coils." VIR-0061A-12, 02 2012.

# Nomenclature

| | |
|---|---|
| ADC | Analog-to-Digital converter |
| AdV | Advanced Virgo |
| BBN | Big Bang Nucleosynthesis |
| CMB | Cosmic Microwave Background |
| DAC | Digital-to-Analog converter |
| DSP | Digital Signal Processor |
| F0 | Filter 0 |
| F7 | Filter 7 |
| FIFO | First In, First Out |
| FPGA | Field Programmable Gate Array |
| GR | General Relativity |
| HRG | Hemispherical Resonator Gyroscope |
| ID | Inertial Damping |
| IP | Inverted Pendulum |
| LQG | Linear-Quadratic-Gaussian |
| LTI | Linear Time-Invariant system |
| LUT | Look-Up Table |

| | |
|---|---|
| LVDT | Linear Variable Differential Transformer |
| MIMO | Multiple-Input and Multiple-Output |
| NCO | Numerically Controlled Oscillator |
| PA | Phase Accumulator |
| PAC | Phase-to-Amplitude Converter |
| PID | Proportional-Integral-Derivative controller |
| PLL | Phase-Locked Loop |
| PSD | Power Spectral Density |
| SA | Superattenuator |
| SF | Standard Filter |
| SGWB | Stochastic Gravitational-Wave Background |
| SISO | Single-Input and Single-Output |
| SNR | Signal-to-Noise Ratio |
| SR | Special Theory of Relativity |